

# Fracture modeling of layered composites in a specialized off-axis finite element framework

Department of  
Wind Energy  
Master Report

Leon Herrmann

DTU Wind Energy-M-0485

October 2021

**DTU Wind Energy**  
Department of Wind Energy

---



# Fracture modeling of layered composites in a specialized off-axis finite element framework

Wissenschaftliche Arbeit zur Erlangung des Grades  
M.Sc.  
an der Ingenieurfacultät Bau Geo Umwelt  
der Technischen Universität München.

**Betreut von** Prof. Dr. -Ing. habil. Fabian Duddeck  
Professur für Computational Mechanics  
Assoc. Prof. Lars Pilgaard Mikkelsen  
DTU Wind Energy  
Prof. Christian Frithiof Niordson  
Assoc. Prof. Brian Nyvang Legarth  
DTU Mechanical Engineering

**Eingereicht von** Leon Herrmann  
leon\_herrmann@yahoo.de

**Eingereicht am** München, den 12.10.2021

# Anhang I

## Erklärung

Ich versichere hiermit, dass ich die von mir eingereichte Abschlussarbeit selbstständig verfasst und keine anderen als die angegebenen Quellen und Hilfsmittel benutzt habe.

---

Kopenhagen, 12.10.2021, Unterschrift

# Abstract

*A previously developed off-axis finite element framework is applied to the different damage mechanisms of fiber-reinforced composites encountered during tension-tension fatigue. The considered damage mechanisms are tunneling cracks and delamination cracks. First, the axial stiffness degradation caused by the cracks is computed, where a good agreement with a variety of models from literature is achieved. Afterward, the energy release rates for the cracks are estimated. For the delamination cracks, the virtual crack closure technique is employed, while for the tunneling cracks a variation of the crack closure technique is used. The energy release rates can in combination with empirical power laws be used to estimate the fatigue behavior of the laminates, which is useful for both the lifetime prediction and monitoring of the damage progress during its lifetime. Finally, also the fiber-matrix microstructure and non-straight cracks are included in the simulations to study their effect and to validate the usage of homogenization approaches. The computations are significantly faster than previous numerical methods while retaining or even improving the accuracy. This makes it possible to include more detail in the model, such as fiber-matrix microstructures, which typically are neglected. The outcome of this thesis besides highlighting the capabilities of the off-axis framework, is a Python code, that in combination with Abaqus can compute, the axial stiffness degradation and the energy release rates, given an arbitrary layup with cracks oriented in a single arbitrary direction with the option of including a fiber-matrix microstructure and non-straight cracks.*

# Zusammenfassung

## Bruchmechanische Modellierung von laminierten Kompositen mit Hilfe einer speziellen off-axis Finite Element Methode

*Ein zuvor entwickeltes off-axis Finite Element Modell wird für verschiedene Schadensmechanismen verwendet, die unter Zug-Zug Materialermüdung bei Faserverbundwerkstoffen auftreten. Die untersuchten Schadensmechanismen sind Tunnelrisse und Delaminierungsrisse. Zuerst wird der axiale Steifigkeitsverlust, welcher durch die Risse verursacht wird, berechnet, wo eine gute Übereinstimmung mit einer Vielzahl von Resultaten aus der Literatur erreicht wird. Danach wird die Energiefreisetzungsrates der Risse bestimmt. Für die Delaminierungsrisse wird hierfür die „virtual crack closure“ Technik verwendet, und für die Tunnelrisse eine Variation der „crack closure“ Technik. Die Energiefreisetzungsrates kann in Kombination mit empirischen Potenzgesetzen genutzt werden, um das Materialermüdungsverhalten der Lamine hervorzu sagen. Dies ist nicht nur nützlich für die Vorhersage der Lebenszeit, aber auch für die Überwachung des Schadenszustandes während der Lebenszeit. Schließlich werden auch die Fiber-Matrix Mikrostruktur und nicht-gerade Risse in den Simulationen aufgenommen, um dessen Einfluss zu studieren und den Gebrauch von Homogenisierungsmethoden zu validieren. Die Berechnungen sind gleichzeitig schneller und genauer als andere numerische Methoden. Dies ermöglicht es mehr Details im Modell aufzunehmen, sowie zum Beispiel die Fiber-Matrix Mikrostrukturen, welche normalerweise vernachlässigt werden. Das Ergebnis dieser Arbeit, abgesehen von der Illustration der Möglichkeiten des off-axis Finite Element Modells, ist ein Python Kode, welcher in Kombination mit Abaqus den Steifigkeitsverlust und die Energiefreisetzungsrates eines arbiträren Laminats mit Rissen orientiert in eine einzelne arbiträre Richtung berechnen kann. Zusätzlich hat man die Option eine Fiber-Matrix Mikrostruktur und nicht-gerade Risse hinzuzufügen.*

# Resumé

## Brudmekanisk modellering af lagdelte kompositter udført ved hjælp af en speciel off-axis finite element metode

*Et tidligere udviklet off-axis finite element model anvendes for forskellige skademekanismer, som optræder i forbindelse med træk-træk udmattelse i fiber-kompositter. De undersøgte skademekanismer er tunnelrevner og delamineringsrevner. Først bliver den aksiale stivhedsdegradering på grund af revnerne beregnet, hvor en god overensstemmelse med flere resultater fra litteraturen bliver opnået. Bagefter bestemmes energifrigørelsesraten af revnerne. Til delamineringsrevnerne bruges den såkaldte "virtual crack closure" teknik, og til tunnelrevnerne bruges en variation af "crack closure" teknikken. Energifrigørelsesraterne kan i kombination med empiriske potenslove bruges til at forudsige udmattelsen i materialet. Det kan både bruges til at forudsige levetiden men også til at overvåge tilstanden af skaden. Til sidst inkluderes også fiber-matrix mikrostrukturen og ikke-lige revner i simulationen for at studere dens indflydelse og bekræfte brugen af homogeniseringsmetoder. Beregningerne er både hurtigere og har en højere præcision end andre numeriske metoder. Det gør det også muligt at inkludere flere detaljer i modellen, som for eksempel fiber-matrix mikrostrukturer, som normalt ses bort fra. Resultatet af arbejdet er både en fremvisning af potentialet af off-axis finite element modellen, men også en Python kode, som i kombination med Abaqus kan beregne stivhedsdegraderingen og energifrigørelsesraten af et arbitrært laminat med revner orienteret i en enkel arbitrær retning. Yderligere har man muligheden for at tilføje en fiber-matrix mikrostruktur og ikke-lige revner.*



# Preface

It is planned, that this work will also be published with the goal of the following four publications:

- (a) L. P. Mikkelsen, B. N. Legarth, L. Herrmann, M. M. Christensen, and C. F. Niordson. “A special finite element applied to tunnel cracking in laminates”. In: *in review*
- (b) L. Herrmann, L. P. Mikkelsen, B. N. Legarth, and C. F. Niordson. “The influence of the fiber-matrix microstructure on off-axis tunnel cracking in laminates”. In: *in preparation*
- (c) L. Herrmann, L. P. Mikkelsen, B. N. Legarth, F. Duddeck, and C. F. Niordson. “An efficient stiffness degradation model for layered composites with arbitrarily oriented tunneling and delamination cracks”. In: *in preparation*
- (d) L. Herrmann, L. P. Mikkelsen, B. N. Legarth, and C. F. Niordson. “Investigation of the delamination propagation in layered composites”. In: *planned*

The work from the bachelor thesis has already been submitted as (a). The remaining work is still to be submitted, but is under preparation as three separate manuscripts: (b), (c), and (d), where the first two manuscripts have been prepared and the second is attached in section [A.3](#). (b) is referred to as [[Her+21b](#)]<sup>1</sup> and (c) as [[Her+21a](#)].

This would all not have been possible without the excellent guidance and patience, that I have received by my supervision from Lars Pilgaard Mikkelsen, Brian Nyvang Legarth, and Christian Frithiof Niordson throughout the past three years. I am very grateful and exceptionally lucky to have had this opportunity and can not thank them enough for it. I also truly hope to be able to continue our great collaboration on further exciting projects. Additionally, I also have to thank my additional supervisor for this master thesis, Fabian Duddeck, who was kind enough to provide important insights from another perspective and helped to improve the quality of the thesis.

This thesis was a cooperation between DTU<sup>2</sup> Wind Energy, DTU Mechanical Engineering, and the Chair of Computational Mechanics at TUM<sup>3</sup>. It was carried out as part of an Erasmus+ mobility program and performed at DTU in Denmark.

---

<sup>1</sup> The first draft of this manuscript was not written in the context of this thesis. It has however been rewritten and extended with additional contents from this thesis.

<sup>2</sup> Danmarks Tekniske Universitet

<sup>3</sup> Technische Universität München

# Contents

Abstract	I
Zusammenfassung	II
Resumé	III
Preface	V
1 Introduction	1
2 Background	3
2.1 Fiber-Reinforced Composites	3
2.2 Fatigue Damage in Fiber-Reinforced Composites	4
2.3 Fracture Mechanics	6
2.4 Tunneling Crack Propagation	9
2.5 Stiffness Degradation	10
2.6 Delamination	12
3 Aims and Objectives	14
4 Stiffness Degradation	17
4.1 Tunneling Cracks	17
4.1.1 Model Description	17
4.1.1.1 Displacement Based Load Application	19
4.1.1.2 Force Based Load Application	21
4.1.1.3 Analytical Lower Bound	21
4.1.2 Verification	23
4.1.2.1 Convergence Study	23
4.1.2.2 Periodic Boundary Conditions	24
4.1.3 Validation	25
4.1.3.1 Classical Laminate Theory	26
4.1.3.2 Tunneling Cracks Orientated at 90°	26
4.1.3.3 Arbitrarily Orientated Tunneling Cracks	26
4.1.3.4 Periodicity of the Model	29
4.1.4 Results	29
4.2 Delamination Cracks	31
4.2.1 Model Description	32
4.2.2 Verification	33
4.2.2.1 Convergence Study	33
4.2.3 Validation	34
4.2.4 Results	34
5 Delamination Propagation	39
5.1 Model Description	39
5.1.1 Virtual Crack Closure Technique	39
5.1.2 Tunneling Crack Propagation	42
5.1.3 Crack Propagation and Fatigue	46

5.2	Verification.....	48
5.2.1	Convergence Study .....	49
5.3	Validation.....	50
5.4	Results.....	53
6	Influence of the Fiber-Matrix Microstructure.....	60
6.1	Model Description.....	60
6.2	Verification.....	63
6.3	Results.....	63
6.3.1	Stiffness Estimation and Degradation .....	63
6.3.2	Delamination Propagation.....	64
6.3.3	Tunneling Crack Propagation .....	65
7	Discussion.....	72
7.1	Limitations.....	72
7.2	Assumptions.....	73
7.3	Outlook.....	75
8	Conclusion.....	77
A	Appendix.....	78
A.1	Difference between Load-Controlled and Displacement-Controlled Energy Release Rate Computation .....	78
A.1.1	Load-Control.....	78
A.1.2	Displacement-Control .....	79
A.2	Program Documentation .....	80
A.3	Appended Manuscripts .....	86
A.3.1	Manuscript [Her+21a] .....	87
	List of Symbols.....	100
	List of Figures.....	103
	List of Tables.....	106
	Bibliography.....	107

# 1. Introduction

Composite materials have emerged as one of the highly sought-after materials in the second half of the 20th century. The combination of different materials gives rise to materials with property combinations, that could not have been achieved before [CR15]. A type of composites known for their exceptional strength and stiffness to weight ratio are the so-called fiber-reinforced composites, composed of fibers, such as Glass or Carbon embedded in a matrix material, such as an Epoxy-resin. These are encountered in many different industries, such as e.g. aerospace, automotive and even sports [ZB09].

One industry, in particular, the wind industry, relies heavily on the usage of fiber-reinforced composites for their wind turbine blades. The main driving factor is to keep the cost of energy production during its lifetime as low as possible to compete with carbon-based energy sources. To achieve this, the size of the wind turbine blades is increased, as the power output of a turbine is proportional to the square of the blade length. At the same time, the weight of the blade plays an important role, which is why fiber-reinforced composites are used here [Jes17]. Another way of decreasing the cost of energy is by increasing the lifetime of the turbines, which is currently at about 20-30 years with large uncertainties. Due to these uncertainties large safety factors are used, which is detrimental to the cost of energy. Hence it is of interest to improve the methods considering the lifetime prediction, i.e. the fatigue behavior of fiber-reinforced composites [Jes17]. The fatigue damage comprises of both a compression and tension part, where buckling occurs during compression and fracture during tension. The Fracture mechanisms can be described in three steps, the initiation and propagation of off-axis tunneling cracks, the delamination, and finally the breakage of fibers in the load-carrying layers [CW82], [Jes+16].

Previously, a specialized off-axis finite element framework was developed by [Mik+21] to study the tunneling cracks, that occur due to fatigue. The advantage of this approach is its computational speed, as it is several orders of magnitudes faster than previous numerical methods while retaining or even improving its accuracy through improved mesh refinements. For this reason, it is interesting to consider the possibilities of this framework for the remaining fracture mechanisms during fatigue in fiber-reinforced composites. This thesis, therefore, explores the options of how to use this framework for the analysis and prediction of fatigue behavior in fiber-reinforced composites.

Three possible applications have been identified, which also define the outline of the thesis. After a brief introduction of the relevant background information, the first application, the stiffness degradation caused by the tunneling and delamination cracks is presented. It is of interest, as it enables monitoring of the damage progress in a structure, while also providing an estimate of how a structure will perform during its lifetime. The application of the framework was successful achieving a good agreement with analytical, numerical, and experimental data across the literature.

Afterward, the propagation of both tunneling and delamination cracks is discussed with a focus on the delamination propagation, where again a good agreement is found with results presented in literature. An attempt is also made to combine the crack propagation and stiffness estimation tools to predict both the lifetime and its material properties throughout its lifetime. The estimates are relatively rough, but show potential, if extended with more sophisticated approaches.

Finally, methods to incorporate a fiber-matrix microstructure are presented. Here, the focus lies on the methods, which can be applied to various problems to investigate the influence of the fiber-matrix microstructure and to determine the accuracy of homogenization approaches. Even non-straight cracks are considered.

All three chapters are accompanied by a unified code<sup>1</sup>, which can be used for all the presented applications. The code comes in the form of a Python script, that can be run through the commercial finite element code Abaqus together with the Fortran subroutines that define the specialized off-axis framework. Depending on the desired task, different configuration files are provided. The code is written in such a manner, that it can easily be applied to arbitrary layups and be easily extended with more sophisticated approaches, as long as they obey the assumptions made in the specialized off-axis framework. The documentation of the code is provided in section [A.2](#).

---

<sup>1</sup> available at <https://github.com/Leon-Herrmann/Fracture-Modeling-with-OA2D>

## 2. Background

This chapter aims at providing an overview of the current and relevant literature and background information for this thesis. First, a short overview of the most important concepts and tools for fiber-reinforced composites is provided including the notation and conventions to be used in this thesis. Then the fatigue damage in fiber-reinforced composites is discussed, where the focus lies on the tension-tension fatigue. Here it is seen, that fracture is a dominant part of tension-tension fatigue. Therefore a summary of the basics of fracture mechanics is provided afterward. The section about the fatigue damage however also introduces the main damage mechanisms in fatigue, which include tunneling and delamination cracks. Both of these including their influence on the stiffness make up the remainder of this chapter.

### 2.1. Fiber-Reinforced Composites

Composites are materials, that consist of multiple materials. Thus it is possible to design composites to get specific material properties. This has led to the design of highly desirable composites with high strength-to-weight properties. There exists a wide variety of composites. More information on different kinds of composites can be found in textbooks like [CR15]. This thesis will however only discuss fiber-reinforced composites, i.e. composites composed of fibers and a matrix, typically a polymer such as a resin. The fibers contribute with the stiffness and strength, whereas the matrix holds the fibers together and strengthens the fibers in the transverse direction. Again a variety of fiber-reinforced composites exist. However, in this thesis, only uni-directional fiber-reinforced composites are considered. Here, fibers are embedded in a resin aligned in one direction. This is then called a single ply and illustrated in the right part of fig. 1, where the dashed line indicates the direction of the fibers oriented at an angle  $\theta_3$ . These plies can then be stacked on top of each other to form a more complex material, called a laminate, see left part of fig. 1. The laminate is defined with a stacking notation  $[\theta_1/\theta_2/\theta_3/\theta_4/...]$ . Note also, that here the subindex of the angles  $\theta$  refers to different orientations and not the number of layers, as is commonly used in the layup notation. More general information on the notation of stacking sequences can be found in textbooks like [ZB09]. Cracked layers will play an important role in this thesis. Therefore a special notation to indicate them will be used throughout this work. A cracked layer, e.g. the blue crack in fig. 1, is denoted in the stacking sequence with a subscript  $c$ , i.e.  $[\theta_1/\theta_{2c}/\theta_3/\theta_4/...]$ . The laminate can be described in a global coordinate system  $(x_1, x_2, x_3)$ , whereas each ply will have its own local coordinate system  $(x_L, x_T, x_T)$ , that is marked in red in fig. 1. The longitudinal axis  $x_L$  is aligned with the fiber direction. In the case of  $\theta = 0^\circ$ , the global  $x_1$ -axis and local  $x_L$ -axis coincide. The choice of the global coordinate system in this thesis is unconventional in the context of laminates, but is used due to its convenience in the special element formulation from [Mik+21] and introduced in section 2.4.

Typically for structural analysis, the microstructure, i.e. the fiber and matrix material, are not considered. Here a homogenization approach, such as e.g. the rule of mixtures, the Halpin-Tsai rule,

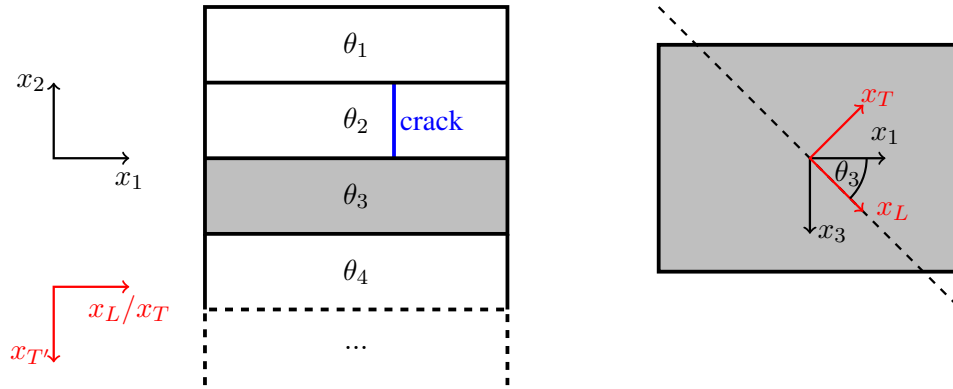


**Figure 1** A generic laminate consisting of multiple plies with different fiber orientations marked by  $\theta_i$ . Left: A side view in the  $(x_1, x_2)$ -plane. Right: A top view in the  $(x_1, x_3)$ -plane.

experimental measurements, or numerical methods, are used. Thus each ply is approximated with an orthotropic material. Additionally, the classical laminate theory can be employed, such that the individual plies are neglected. Here a relation between the global normal forces and bending moments  $(N_1, N_3, N_{13}, M_1, M_3, M_{13})$  and the strains and curvatures  $(\epsilon_{11}, \epsilon_{33}, \epsilon_{13}, \kappa_1, \kappa_3, \kappa_{13})$  is established via the Kirchhoff plate theory, described in textbooks like [Sun10]. This can be used to compute the deformations of a laminate structure. However, the stress states of the individual plies can still be retrieved using the strains and curvatures and the orthotropic constitutive law of each ply. These individual stress and strain states are useful for various failure criteria, such as e.g. maximum strain, maximum stress, Tsai-Hill, or Tsai-Wu theories. These criteria are very practical for the analysis of laminate structures. However, the actual failure mechanisms, especially when considering fatigue are more complex and are not necessarily captured by these criteria. As these mechanisms are not understood well enough and fiber-reinforced composites have highly sought-after material properties, damage in fiber-reinforced composites is a very active field of research.

## 2.2. Fatigue Damage in Fiber-Reinforced Composites

Damage mechanics, described in textbooks like [Lem96], [LD10], considers the progressive and irreversible physical process, that breaks a material. It is used to study both the degradation of the mechanical properties and the failure of materials. Typically damage initiates at small defects and stress concentrations through which debonding and thereby microcracking occur. These microcracks then coalesce and finally lead to the initiation of a macroscopic crack, which may propagate through the specimen. Thus the specimen often becomes unusable and failure has thereby occurred. Although the mechanisms usually follow the same pattern, differences occur due to the material, the loading, and the temperature. The common categories are brittle damage, ductile damage, creep damage, low cycle fatigue damage, and high cycle fatigue damage.

In the context of fiber-reinforced composites in the wind industry, the main concern is the high cycle fatigue damage, as turbine blades are expected to endure  $10^8 - 10^9$  cycles during their lifetime [JM17]. Here damage typically initiates, due to debonding between the fibers and matrix

in the plies orientated in an off-axis direction, as described in [Mar14]. The microcracks caused by the debonding then coalesce through matrix cracking until a crack is formed, that spans the entire ply in the vertical direction. These cracks are called tunneling cracks as they then tunnel i.e. propagate along the fiber direction in their corresponding ply. This initiation process is also observed in [Rei91], where both quasi-static and tension-tension fatigue experiments were conducted. During the quasi-static loading, the tunneling cracks are observed in the off-axis plies causing a large stiffness degradation, which is then linked to a progressive failure of the plies. The accumulation of the failed plies then leads to fiber failures in the load-carrying plies accompanied by a large drop in stiffness and load-carrying capabilities, which then leads to the last ply failure i.e. the failure of the entire composite. The fatigue tests show similar behavior, where first a formation and saturation of the tunneling cracks is observed, followed by a delamination between the plies, which then finally leads to the fiber failure. The effect of these three stages on the stiffness is shown in fig. 2.

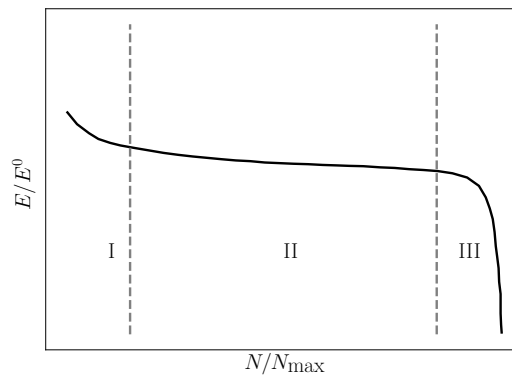


**Figure 2** Effect of the three damage stages on the stiffness. The current stiffness  $E$  normalized with the original stiffness  $E^0$  is related to the number of cycles  $N$  normalized with the total number of cycles  $N_{max}$ . The figure was inspired and adapted from [Rei91], [Jes+16].

The same three stages have been observed by multiple experimental investigations, such as [JM17], [Wan+18] using X-ray computed tomography. The three damage mechanisms associated with these three stages are illustrated in fig. 3 for a  $[0/90]$ -layup under axial loading i.e. in the direction of the  $0^\circ$  fibers. In the first stage (I) tunneling cracks, marked in red initiate and propagate. This then leads to a stress concentration at the interface between the layers and thereby causes the delamination, marked in blue, for the second stage (II). The laminate is thereby significantly weakened and the fibers in the load-carrying ply start to fail, marked in dark gray. This is referred to as the third stage (III).

A variety of additional experimental studies have been conducted, that support this failure behavior in fiber-reinforced composites.

The stiffness degradation due to the tunneling cracks and them being the cause for the delamination is also described by [ZBG14]. It is also stated, that the understanding of these damage mechanisms is essential to improve the lifetime of fiber-reinforced composites.

Also, [JSK18], [Jør17], show the importance of tunneling cracks in wind turbine blades. Here the effect of the residual stresses and other parameters on the formation of the cracks and the

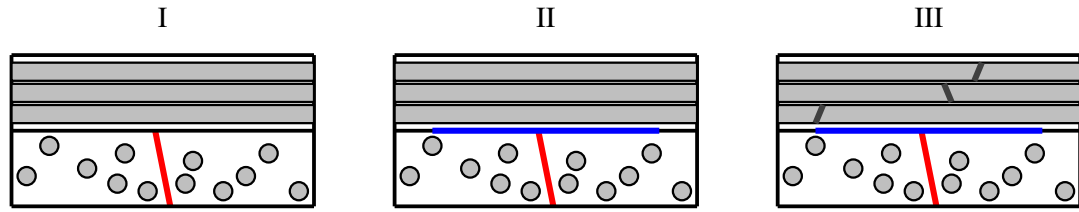


**Figure 3** The three damage mechanisms in fiber reinforced composites under tension. Left: Tunnelling cracks (red) are initiated and propagated in the off-axis layers. Center: The stress concentrations due to the tunnelling cracks initiate delamination cracks (blue) between the off-axis layers and load-carrying layers. Right: Fiber fracture (dark gray) of the load-carrying fibers leads to a major loss in strength and thereby leads to the final failure.

initiation of the delamination was investigated both experimentally and numerically. Again the importance of these failure mechanisms for the lifetime is highlighted.

The influence of delamination on the failure is also analyzed by [Wis12]. Here it is shown, that the delamination tendency is critical with respect to the strength of the composite.

However, also the interaction of the different damage mechanisms is of importance, as seen in [SF04], where numerical plane strain models are used.

To conclude, it is shown in literature that the tension-tension fatigue damage mechanics in fiber-reinforced composites are important to predict their lifetime and occur in three distinguishable stages, where all concern crack propagation. Thus a common strategy to analyze fatigue damage in fiber-reinforced composites is with fracture mechanics, with which the propagation of each of these cracks can be studied. An overview of common approaches in fracture mechanics can be found in textbooks like [And17] and [GS18].

It also has to be noted, that composites usually also experience compression during cyclic loading causing buckling, which might accelerate the fatigue failure, due to the interaction between buckling and cracking, as discussed by [RJ82]. This thesis will however limit itself to tension-tension fatigue. In particular, the focus will lie on the first two stages shown in fig. 3. A good overview of the full picture of damage in fiber-reinforced composites is however provided by [TV16] in general and for the delamination mechanisms by [Sri08].

### 2.3. Fracture Mechanics

As highlighted in the previous section 2.2, the tension-tension fatigue damage in fiber-reinforced composites is dominated by fracture. Thus the main concepts in fracture mechanics, that are important for this thesis, will be explained briefly. More detailed information can be found in textbooks, such as [And17], [Zeh12] and [GS18].

Only linear elastic fracture mechanics will be considered here. In linear elastic fracture, the crack tip is a stress singularity. It is therefore not possible to determine its propagation via stress-based methods commonly used in strength of materials calculations. One approach to circumvent this issue, is the Griffith energy balance [Gri21], which states, that the total potential energy of a system has to decrease or remain constant after the propagation of a crack. Thus it is possible to

define the criteria of crack growth, as the point, where the total potential energy stays constant. In other words, the decrease in potential energy due to the propagation of a crack has to match the surface energy of the material. This concept was then used by [Irw56] to define a convenient quantity to describe the phenomenon, the energy release rate  $\mathcal{G}$ .

$$\mathcal{G} = -\frac{d\Pi}{dA} \quad (2.1)$$

The energy release rate is defined, as the negative potential energy  $\Pi$  derived with respect to the increase in crack area  $A$ . In the context of numerical methods, this is commonly approximated by the negative change in potential energy  $\Delta\Pi$  for a given crack area increment  $\Delta A$  or a crack length increment  $\Delta a$ . The energy release rate is “a measure of the energy available for an increment of crack extension”, [And17] and is also referred to as the crack extension force or the crack driving force. To determine if a crack grows, the energy release rate can be compared to a critical energy release rate  $\mathcal{G}_c$ , also known as the fracture toughness. Alternative measures are the stress intensity factor  $K$  and the  $J$ -Contour Integral  $J$ . All of these measures are equivalent in linear elastic fracture mechanics and only the energy release rate  $\mathcal{G}$  will be considered in this thesis.

Fracture may occur in three different modes. Mode I is the normal crack opening mode, mode II is the in-plane shear crack opening mode and mode III is the out-of-plane shear crack opening mode. All three modes are illustrated in fig. 4. The modes are described with their corresponding subindices, e.g. the energy release rate with respect to mode I is denoted as  $\mathcal{G}_I$ . In isotropic materials, these modes typically relate directly to the loading, i.e. a normal load perpendicular to the crack will lead to a mode I crack propagation. However, in orthotropic materials, such as laminates, this is no longer the case. Here a combination of modes can occur under uni-axial loads, in particular at bi-material interfaces.

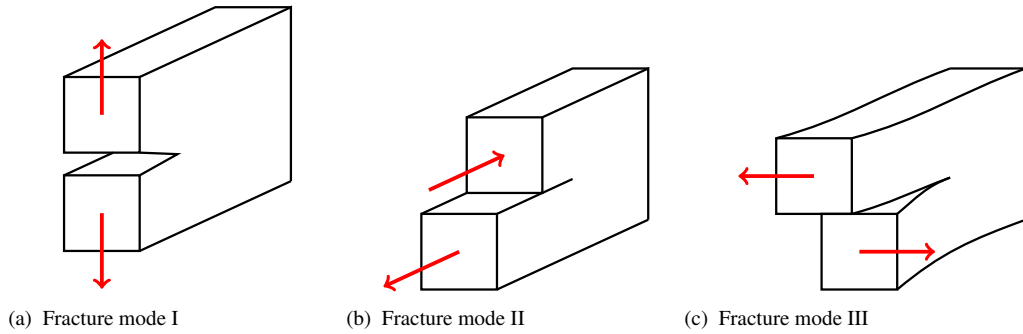


**Figure 4** The three fracture modes. The figure was inspired and adapted from [And17].

To quantify this mixture of modes, the mode mixity can be defined via the phase angle  $\Psi$  between two stress intensity factors, as shown in [Mik+20].

$$\Psi_{I+II} = \arctan\left(\frac{K_{II}}{K_I}\right) \quad (2.2)$$

$$(2.3)$$

Alternatively, the phase angles can be reformulated by replacing the stress intensity factors with

the expressions from [Bao+92] for the relations between stress intensity factors and energy release rates,

$$\Psi_{I+II} = \arctan \left( \lambda^{-1/4} \sqrt{\frac{\mathcal{G}_{II}}{\mathcal{G}_I}} \right) \quad (2.4)$$

$$(2.5)$$

where  $\lambda = E_2/E_1$ .

When considering fatigue, the main question is how much a crack propagates per cycle, i.e. the goal is the determination of the crack growth rate per cycle  $da/dN$ . This is commonly estimated via empirical laws, as it is observed, that the growth rate  $da/dN$  and the range of the stress intensity factors  $\Delta K = K_{\max} - K_{\min}$  have a linear tendency on a log-log plot for a large range of  $\Delta K$ , as can be seen in fig. 5.

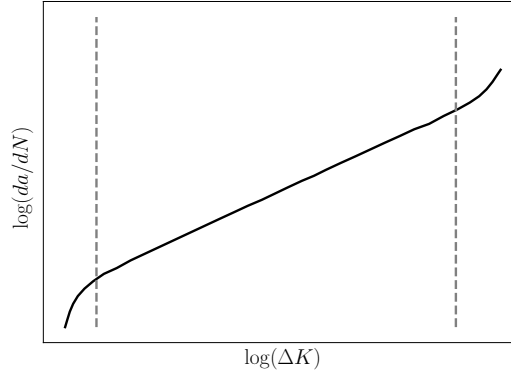


**Figure 5** The linear correlation of the crack growth rate  $da/dN$  and the range of the stress intensity factor  $\Delta K$  in a log-log plot between the gray dashed lines. The figure was inspired and adapted from [And17].

Thus it is possible to define empirically based power laws, as was done by [PE63] and referred to as Paris' law,

$$\frac{da}{dN} = C \Delta K^m \quad (2.6)$$

where  $C$  and  $m$  are the fitted parameters found with experiments. The lifetime can then be extracted via an integration with respect to  $da$ .

These power laws have also been adapted and used for tunnel cracks by [QC14] and delamination cracks by [CMQ19] in fiber-reinforced composites. Instead of using the range of stress intensity factors  $\Delta K$ , the energy release rate is used,

$$\frac{da}{dN} = D \mathcal{G}^n \quad (2.7)$$

where  $D$  and  $n$  are the fitted parameters found with experiments. With this empirical power law, it is possible to relate the energy release rate  $\mathcal{G}$  to the crack propagation per cycle  $da/dN$  and thus estimate both the lifetime and material properties during its lifetime given the energy

release rate. For this, the energy release rate  $\mathcal{G}$  has to be computed. Thus efficient methods for its estimation are highly desirable for both the creation of the Paris-like curves via experiments and the application of these curves.

## 2.4. Tunneling Crack Propagation

As shown in fig. 2 the most significant impact on the mechanical properties during the lifetime of the fiber-reinforced composite i.e. before fiber failure, occurs during stage I i.e. the formation and propagation of tunneling cracks. Thus tunneling cracks are of great interest and are therefore heavily researched. As stated earlier, [Mar14] has investigated the initiation of these tunneling cracks on a microscale and has discussed the relation of the fiber matrix interface with the fracture toughness. Here the focus will however lie on the propagation of these tunneling cracks. It is therefore typically assumed, that a crack spanning the full height of the ply has already formed.

One of the earliest approaches is seen in [HS93], where  $90^\circ$  off-axis cracks are considered in isotropic materials. Here it is shown, that the energy release rate  $\mathcal{G}$  reaches a steady-state, i.e. it is invariant with respect to the depth of the crack. Additionally, it is shown, that this steady-state energy release rate  $\mathcal{G}_{ss}$  is independent of the shape of the crack tip. It is possible to compute the energy release rate with the stress state in front of the crack and with the crack opening displacement in the wake of the crack. This is then exploited to derive a relatively simple formula for the calculation of the energy release rate using only the undamaged stress state  $\sigma_{11}^0$  and the crack opening displacement  $\Delta u_2$ .

$$\mathcal{G}_{ss} = \frac{1}{2h} \int_0^h \sigma_{11}^0(x_2) \Delta u_2(x_2) dx_2 \quad (2.8)$$

The undamaged stress state is found analytically, whereas the crack opening displacement is found numerically. For this plane strain is assumed. This was applied in a similar manner for channeling surface cracks in [Beu92].

Similar analyses were employed to find the crack opening displacement for periodic tunneling cracks in [BZC13]. The method was also extended to take the crack interaction of cracks in the same layer into account in [HS91]. It was also combined with the delamination in [SF04]. Here the combination of the off-axis tunneling crack propagation and off-axis delamination propagation was investigated.

Recently, [Mik+20] showed, that the steady-state in the direction of the off-axis crack and independence of the crack tip shape also holds for arbitrarily oriented off-axis cracks in orthotropic plies. This lead to the generalization of eq. (2.8), where mixed-mode fracture i.e. mode I  $\mathcal{G}_{I_{ss}}$  and mode II  $\mathcal{G}_{II_{ss}}$  fracture now occur.

$$\mathcal{G}_{ss} = \mathcal{G}_{I_{ss}} + \mathcal{G}_{II_{ss}} = \frac{1}{2h} \int_0^h \sigma_{11}^0(x_2) \Delta u_n(x_2) dx_2 + \frac{1}{2h} \int_0^h \sigma_{13}^0(x_2) \Delta u_t(x_2) dx_2 \quad (2.9)$$

Here  $\sigma_{11}^0$  and  $\sigma_{13}^0$  are the stress states from the undamaged laminate found with classical laminate theory, described in textbooks such as [ZB09]. The normal crack opening displacement  $\Delta u_n$  and tangential crack opening displacement  $\Delta u_t$  are found with 3D finite element models. The crack propagation reaching a steady-state, i.e. the strain and stress being invariant with respect to the off-axis crack direction, was then used by [Mik+21] to develop a specialized 2D off-axis finite element framework. The results obtained by this framework were in good agreement with the 3D model with simulation times being four orders of magnitude lower, due to the dimensionality reduction.

The decrease in simulation time made it possible for [Her+21b] to add a fiber matrix microstructure to the cracked plies. This was done to investigate the influence of the microstructure on the energy release rate and thereby quantify the quality of the usage of homogenized models. Both regular fiber alignments and more realistic alignments taken from CT-scans, from [MMA21], were used for this investigation. The fiber-matrix microstructures with their cracks are illustrated in fig. 56. The work is unfinished, but for the regular alignments, the deviations from the homogenized models were under 6%.

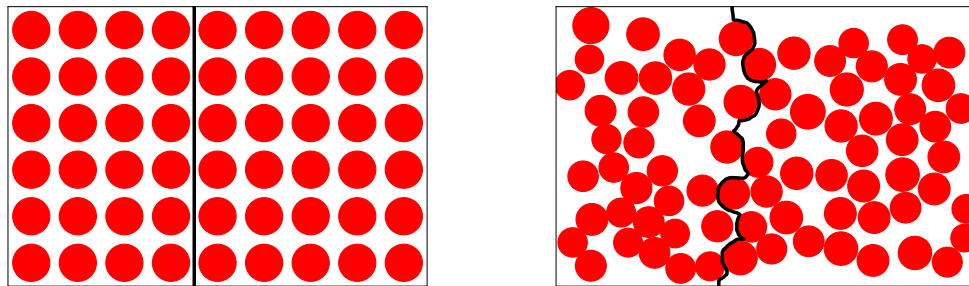


**Figure 6** The fiber-matrix microstructures employed in the off-axis layers in the vicinity of the crack in [Her+21b]. The red circles indicate the fibers, the white spacing the matrix and the black line the crack. Left: A regular microstructure. Right: An irregular microstructure with a non-straight crack extracted from a CT-scan in [MMA21].

## 2.5. Stiffness Degradation

It is essential when designing for fatigue to understand the stiffness degradation caused by the damage mechanisms described in fig. 3. A good understanding can be used in two ways. Firstly, it can be used during the design phase to ensure safety during its lifetime. Secondly, it can be also used to monitor the health, i.e. estimate the tunneling crack density, delamination ratio, and amount of fiber failure, by observing the mechanical properties during operation.

A variety of approaches, both analytical and numerical, exist. Especially the degradation, due to tunneling cracks has been investigated heavily. A great overview of the current approaches is provided by [CQ15]. One of the first methods is the stress transfer model by [McC96], which formulates a fourth-order differential equation for the stress perturbation, due to uniformly dis-

tributed cracks. The equation has to be solved numerically. The method is limited to  $90^\circ$  off-axis cracks in a single layer. Similarly [JV99] provide a closed-form analytical model to express the stress perturbation and thereby the mechanical properties with respect to the crack density. The model is called the shear lag model. It is however also limited to  $90^\circ$  off-axis cracks in a single layer. The analytical GLOB-LOC model by [Pup+16] achieves similar results by also using a shear lag approach. Although the original formulation was for  $90^\circ$  off-axis cracks, it has been extended to arbitrary angles in [LV20] using the crack sliding displacement. The extended method can be applied to arbitrarily oriented cracks in arbitrarily many layers. An analytical model with similar capabilities is the optimal shear lag analysis by [CQ15] also being able to predict the stiffness from arbitrarily oriented cracks in arbitrarily many layers. The approach has been improved even further in [CMQ21]. The last analytical model, [ZH99] derives differential equations, which however have to be solved numerically. This approach has a similar flexibility as the previous two with respect to the distribution of cracks.

The numerical approaches usually exploit the periodicity by using representative volume elements, referred to as RVEs. Here [LST09] uses a 3D RVE to model two layers of cracks. The approach can handle arbitrary crack orientations, but at maximum cracks in two layers. Similarly, [BCC13] proposes a 3D RVE, where the cracks have to be aligned in a single orientation. An alternative is the periodic 3D RVE model proposed by [MCQ18] considering cracks in only a single layer. However, this model is additionally capable of taking the delamination into account. For cracks oriented at  $90^\circ$ , plane strain models can be used, as seen in [LV05].

Lastly also variational approaches exist, as e.g. [VH10]. These are however usually quite limited with respect to the layup configurations and the number of cracks.

It has to be noted, that all of the previous methods only predict the stiffness given a crack density. The crack density can however be estimated by studying the effect of neighboring cracks on the crack propagation properties discussed in section 2.4. This was analyzed in [Mik+20] and [Mik+21]. A more sophisticated model predicting the expected crack density evolution is provided by [CMQ17], where the local hydrostatic stress and maximum principal stress determine the initiation of new tunnel cracks and thereby their density. Alternatively, experiments can also be taken into consideration, which can show the saturated crack density.

There are also quite a few experiments, that have investigated the stiffness degradation, such as [Var+99] for a  $[0/\pm\theta_{4c}/\bar{0}]_s$  layup, [Ton+97] for a  $[0/90_c/\mp 45_c]_s$  layup and [KMG06], [Kat+08] for a  $[0/45_c]_s$  layup. These are useful to validate analytical and numerical methods.

The degradation, due to the delamination, as illustrated in stage II of fig. 2 has been studied less intensely. For this task, the periodic model by [MCQ18] has been used to estimate its influence for arbitrarily oriented cracks in a single layer. The same model was used by [CMQ19] for cracks oriented at  $90^\circ$ . Similar results were obtained via a plane strain model in [SF04]. Thus the influence of the delamination on the stiffness properties has mainly been studied with numerical

methods.

## 2.6. Delamination

Delamination, i.e. the propagation of delamination cracks has however been investigated heavily. A good overview over the process of delamination is provided by [Sri08], whereas [CMQ19] provide an insight for the delamination in fiber-reinforced composites. It is also described here, how the delamination is induced by the stress concentrations of the tunneling cracks. Here, the periodic model by [MCQ18] is used to predict the energy release rates for cracks oriented at  $90^\circ$ . Their method should however also work for arbitrary orientations. The energy release rates are found with the virtual crack closure technique, explained thoroughly in [Kru04], and are then related to the delamination growth rate via a power law using experimental data. Furthermore, a description of the common delamination configurations is provided. This is illustrated in fig. 7, where two main delamination configurations are seen, the H-shaped and the Z-shaped delamination. Additionally, there are some variations, referred to as the incomplete and mixed configurations. These configurations were observed experimentally and the variations can be explained by the deviations in the underlying microstructure. The most common configuration, 45% of the cases, is the H-shaped delamination whereas 17% were Z-shaped and 26% had a mixed shape. Thus the focus of their investigations lies on the H-shaped delamination. The H-shaped delamination is also the least complex configuration, as it is symmetric, which can be exploited in a model.

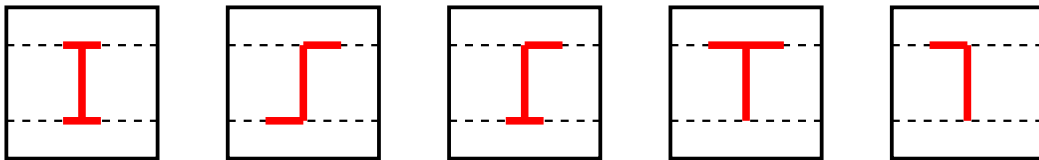


**Figure 7** Delamination configurations. From left to right: H-shaped delamination, Z-shaped delamination, Mixed delamination, Incomplete H-shaped delamination, Incomplete Z-shaped delamination. Figure adopted from [MCQ18].

As stated before in the case of  $90^\circ$  off-axis cracks, a 2D plane strain model can be used instead of the 3D models as has been shown by [SF04]. However various methods exist to study the delamination at other orientations. A review of the most common methods is provided by [Bak+14], where the methods are classified into three groups, which are cohesive zone envelope models, cohesive zone loading-unloading hysteresis models, and linear elastic fracture mechanics models.

The cohesive zone models describe the crack propagation as overcoming the traction, which holds the crack faces together. These models can directly compute the crack growth rate. However, they also require additional model parameters, to define these tractions, commonly achieved with a potential. Additionally a nonlinear finite element method is required [Bel+14]. Implementations of cohesive zone elements can be found in [Fei05] and [PP12].

The linear elastic fracture mechanics approaches are usually less complex, as they only require a linear analysis and do not require additional model parameters. However, the disadvantage

is, that the crack growth rate is not directly extracted. Instead, the energy release rate is usually computed, which then can be related to the crack growth rate via Paris' law, described in [And17], or variations of it. Paris' law then requires a different set of model parameters.

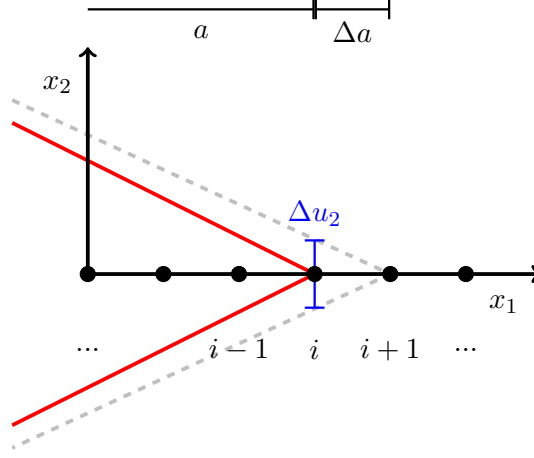


**Figure 8** Schematic illustrating the crack closure integral and virtual crack closure technique for crack propagation along the  $x_1$ -axis. The crack closure integral requires the stress  $\sigma_{22}$  between nodes  $i$  and  $i + 1$  found with the red crack. Additionally the crack opening displacement between nodes  $i$  and  $i + 1$  has to be computed with the gray crack. For the virtual crack closure technique a single simulation with the red crack is required. Here the stress  $\sigma_{22}$  is extracted between nodes  $i + 1$  and  $i + 2$ , while the displacement  $\Delta u_2$  is found between  $i$  and  $i + 1$ . Note, that the depicted schematic assumes linear shape functions. Higher order elements require a slight modification.

The basic principle in most linear elastic fracture approaches used for delamination is the estimation of the change in potential energy, due to the delamination growth. One approach is the crack closure integral [Zeh12], which is a two-step technique. In the case of a crack alignment and propagation with the  $x_1$ -axis, as shown in fig. 8, the stress state  $\sigma_{22}^0$  is computed for the non-propagated crack and the crack opening displacement  $\Delta u_2$  for the propagated state. Both are computed for the element connecting node  $i$  and node  $i + 1$  so that the change in potential energy and the energy release rate can be computed.

$$\mathcal{G}_I = -\frac{\Delta\Pi}{\Delta a} = -\frac{1}{2\Delta a} \int_a^{a+\Delta a} \sigma_{22}^0(x_1) \Delta u_2(x_1) dx_1 \quad (2.10)$$

The virtual crack closure technique, described in [RK77] and [Kru04], circumvents the need for two simulations. Here it is assumed, that the state at the crack tip does not vary significantly when going from a crack length of  $a + \Delta a$  to  $a + 2\Delta a$ . Thus instead of using the stress state  $\sigma_{22}^0$  of the non-propagated crack, the stress state behind the crack tip  $\sigma_{22}(x_1 + \Delta a)$  is used to compute the change in potential energy.

$$\mathcal{G}_I = -\frac{\Delta\Pi}{\Delta a} = -\frac{1}{2\Delta a} \int_a^{a+\Delta a} \sigma_{22}(x_1 + \Delta a) \Delta u_2(x_1) dx_1 \quad (2.11)$$

An alternative is the virtual crack extension method, described in [And17], that exploits the derivative information of the stiffness matrix to determine the change in potential energy in one simulation step. However here the difficulty lies in obtaining the derivative information, which is usually not easily obtainable in commercial finite element codes.

### 3. Aims and Objectives

The main question dictating the direction of this thesis is, if the specialized off-axis finite element framework, developed in [Mik+21], can be used to predict different fatigue damage mechanisms in fiber-reinforced composites accurately and efficiently. As the entire damage process in fiber-reinforced composites is very complex and can not be understood in a single thesis, only selected damage mechanisms are investigated. These are chosen based on the greatest potential for improvement of prior methods by employing the specialized off-axis finite element framework.

The framework exploits a steady-state in an arbitrarily oriented off-axis direction. These steady states have been observed for fracture in [Mik+20], where the off-axis direction is defined along the cracks. It is for this reason, that this thesis will limit itself to the damage mechanisms related to fracture, i.e. under tension. These have been summarized in fig. 3, where three stages are described. The two first stages concerning the tunneling cracks and the delamination are critical for the mechanical properties during the lifetime of a fiber-reinforced composite. Additionally, an understanding of them also provides insight towards the third stage and thus the laminates lifetime. A review of the literature in chapter 2 shows, that methods for these mechanisms are highly sought-after. Up to now, several analytical, semi-analytical and numerical methods exist for the different mechanisms. These however typically lack either accuracy due to their underlying assumptions or efficiency due to costly 3D simulations. Here the specialized 2D off-axis finite element framework might be able to provide an improvement for both the accuracy and the efficiency. Due to the efficiency and flexibility of the approach, it additionally enables the possibility of including a fiber-matrix microstructure, or other defects aligned in the off-axis direction, in simulations, which until now have only been possible in a limited sense. Taking this into account, three aims have been formulated concerning the first two damage stages:

- i Can the stiffness be expressed as a function of the tunneling crack density and the delamination ratio with an efficient 2D finite element simulation?
- ii Can the propagation of delamination cracks be computed with an efficient 2D finite element simulation? Under which circumstances does the delamination occur?
- iii What is the influence of the fiber-matrix microstructure on the stiffness and fracture properties? Is the homogenization approximation accurate?

These aims build upon each other and will be investigated sequentially, where the finite element model can be reused and extended for each subsequent aim. To clarify, how these aims are to be achieved, clear objectives for each aim have been defined:

- i Stiffness degradation
  - Implement a periodic 2D finite element model exploiting the symmetry and antisymmetry [Li08]. For this create a Python script, that takes the full information of the laminate,

the tunneling crack density, and the delamination ratio as input.

- Verify both the periodic boundary conditions and the convergence properties.
  - Validate the shear component  $\sigma_{13}$  in the specialized off-axis finite element framework.
  - Extract the axial stiffness  $E_1$  from the model.
  - Validate the model against experiments and other models. Conduct the validation in steps of increasing complexity (90° off-axis cracks, arbitrarily oriented off-axis cracks, unbalanced laminates).
- ii Delamination crack propagation
- Find an approach to extract the internal nodal forces while using a user element subroutine.
  - Implementation of the virtual crack closure technique [Kru04]. Test the implementation on a double cantilever beam, first for pure mode I and then for mixed-mode fracture, i.e. mode I and mode II fracture. Validate the model with analytical solutions from [And17] and [Sør+06].
  - Add the virtual crack closure technique to the periodic 2D finite element model to estimate the energy release rates  $\mathcal{G}$  for the symmetric delamination.
  - Conduct convergence studies.
  - Validate the model with a comparison to experiments and other models.
  - Conduct parametric studies with respect to the model properties to study under which circumstances delamination occurs.
- iii Influence of the microstructure
- Add a regular fiber-matrix microstructure in the off-axis layer using the previous models.
  - Compare the model to homogenized models and quantify the influence of the microstructure.
  - Add an irregular fiber-matrix microstructure and non-straight cracks and discuss the potential differences.

Additionally, it has to be remarked, that all finite element models will be using fully integrated quadrilateral or triangular elements with quadratic shape functions. This is chosen, as at present the off-axis framework only consists of these elements and an extension would require a considerable effort without providing a foreseeable benefit. In principle, quadrilaterals will always be employed, except for the microstructure cases, as this would complicate the mesh generation.

The materials, that are to be used for the investigations are provided in table 1. These are taken from [Mik+20] and [Mik+21], where they are referred to as GlassFRP1 and CarbonFRP2 and FRP stands for fiber-reinforced polymer. They were chosen, as this makes deductions with respect to the tunneling crack propagation possible without additional simulations. For the same reason,

most investigations will use the layup  $[0/\theta/0/-\theta_c]_s$ .

**Table 1** Material properties.

Material	$E_L$ [GPa]	$E_T = E_{T'}$ [GPa]	$G_{LT} = G_{LT'}$ [GPa]	$G_{TT'}$ [GPa]	$\nu_{LT} = \nu_{LT'}$ [-]	$\nu_{TT'}$ [-]
GlassFRP	30.62	8.620	3.250	2.900	0.2900	0.3300
CarbonFRP	266.0	5.490	3.540	2.370	0.2700	0.4000

## 4. Stiffness Degradation

As seen in fig. 2, the stiffness of fiber-reinforced composites is affected significantly by the tunneling cracks and the delamination. It is therefore important to consider the stiffness degradation during the lifetime of a composite structure. This chapter provides a 2D finite element model using a specialized off-axis framework from [Mik+21], that quantifies the stiffness given a tunneling crack density and a delamination ratio. The model is implemented in steps. First, the tunneling cracks are considered, and afterward, the delamination is added. Furthermore, the investigation is limited to symmetric laminates, denoted with the subindex  $s$  in the stacking sequence. This limitation is chosen, as the off-axis framework has not yet been employed for unsymmetric layups, where coupling effects between extension, shear, and bending occur. The only exception being for the unstructured microstructure in [Her+21b], where a slight asymmetry occurs due to the microstructure. No difficulties were observed for this case. The framework should be fully capable of handling more pronounced unsymmetric layups after conducting a thorough verification and validation.

### 4.1. Tunneling Cracks

This section introduces the 2D finite element model using the off-axis framework, which is to be used for the stiffness degradation caused by the tunneling cracks. The same model is then extended in the upcoming sections on delamination, crack propagation, and the microstructure. After the model description, the correctness of the model is verified and validated. Finally, several parametric studies are conducted to both show the capabilities of the model, but also to provide insights into the influence of tunneling cracks.

#### 4.1.1. Model Description

For the model it will be assumed, that the cracks are distributed periodically. A view from the top of the laminate, i.e. in the  $(x_1, x_3)$ -plane is illustrated in fig. 9. Here the periodic cracks are indicated in red. The normal distance between the cracks  $L$  is used to quantify the crack density  $\rho_c = 1/L$ . Additionally the projection of the normal distance on the  $x_1$ -axis  $\hat{L} = L/\sin(\theta)$  is shown, as it is this distance, that will be modelled in the 2D off-axis model. The 2D off-axis model is in fact also a projection of the 3D problem in  $(x_1, x_2, x_3)$  projected onto the  $(x_1, x_2)$ -plane, indicated by the dashed line in gray.

The projection is shown in fig. 10 in the  $(x_1, x_2)$ -plane, where the periodicity is clearly illustrated. For the illustration the lower half of the layup  $[0/\theta/0/-\theta_c]_s$  with equal layer heights  $h$  is depicted. However, the layer height  $h$  may in principle vary for each ply. Due to the symmetry in the layup, it is sufficient to model only half of the laminate, where the horizontal red dashed line indicates the horizontal symmetry. For the model it is assumed, that the periodicity is repeated infinitely, i.e. the laminate extends infinitely in the  $x_1$ -direction. This is a reasonable assumption, as the

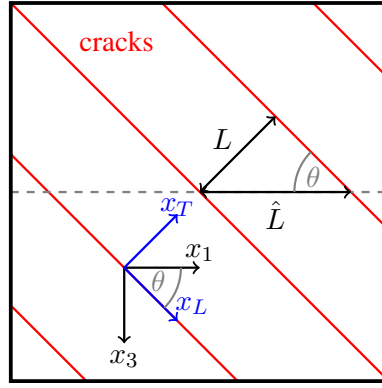


**Figure 9** Top view in the  $(x_1, x_3)$ -plane showing the periodic cracks in red, the distances between the cracks  $L, \hat{L}$  and the global and local coordinate systems.

order of magnitude of the length of a laminate is much greater than that of the thickness. Thus boundary effects can be neglected. The half laminate is loaded under a uni-axial tension load  $N_1$ . Note, that the full laminate would thereby be loaded with  $2N_1$ , which is taken into account by defining the half-height of the laminate as  $H$ . Similarly, the half-height of the crack is also defined as  $h_c$ .

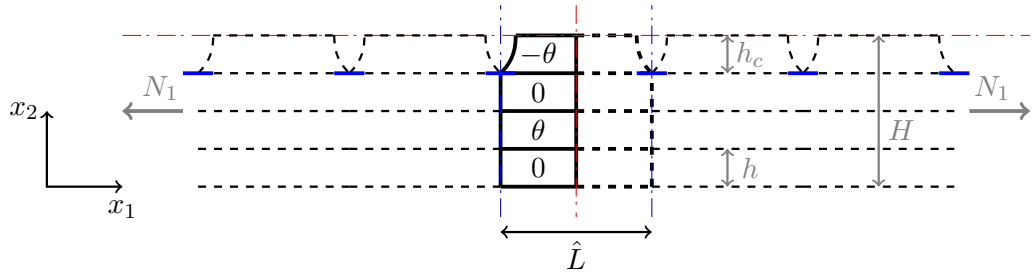


**Figure 10** Lower half of the deformed laminate  $[0/\theta/0/-\theta_c]_s$  under a uni-axial tension load  $N_1$  illustrating the periodicity and symmetry lines. The horizontal red dashed line is a symmetry, whereas the vertical red and blue dashed lines are anti-symmetries. The layer height is indicated with  $h$ . Here all layers have the same height, which does not always have to be the case. The half height of the laminate is then denoted as  $H$  and the half height of the crack as  $h_c$ . The delamination is indicated by the horizontal blue solid lines.

Due to this infinite periodicity of the model, it is sufficient to model only a single period of length  $\hat{L}$ . However, even inside of this period an anti-symmetry is present, indicated by the vertical red dashed line in fig. 10. This can be exploited in the periodic model, which is shown in fig. 11, using the quarter model marked by the black solid lines from fig. 10. The horizontal symmetry is applied at the top of the model, whereas the vertical symmetry is applied on the right side of the model together with a prescribed displacement  $\Delta$  found from the desired force  $N_1$  with classical laminate theory. Alternatively the desired force  $N_1$  can be applied at a single node, while constraining the displacement in the  $x_1$ -direction at the right edge with a multi-point constraint. In principle, the left side of the model requires traditional periodic boundary conditions, enforced with constraint equations. However, as the periodic model also exhibits an antisymmetry, marked with the vertical blue dashed lines in fig. 10, at this edge, the periodic boundary conditions can be simplified to anti-symmetry boundary conditions on the left edge as well. This is also consistent with the explanations of periodic boundary conditions provided by [Li08].

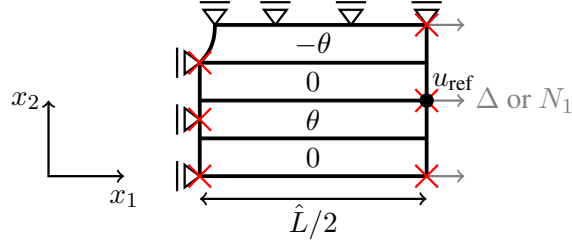


**Figure 11** The deformed periodic model with boundary conditions exploiting the symmetries illustrated in fig. 10. The roller supports restrict the degrees of freedom in the  $x_1$  or  $x_2$  dimension, whereas the red crosses restrict the displacement in the  $x_3$ -direction. The gray arrows indicate a prescribed displacement  $\Delta$  or force  $N_1$ .

As stated before, there are two approaches to apply the load. These will be explained shortly in the following two sections.

#### 4.1.1.1 Displacement Based Load Application

The prescribed displacement  $\Delta$  can be found with classical laminate theory, described in textbooks such as [ZB09]. The theory leads to a constitutive relation, consisting of an extensional stiffness matrix  $\mathbf{A}$ , an extension-bending coupling matrix  $\mathbf{B}$  and a bending stiffness matrix  $\mathbf{D}$ , which relates the normal forces  $\mathbf{N}$  and moments  $\mathbf{M}$  to the strains  $\boldsymbol{\varepsilon}$  and the curvature  $\boldsymbol{\kappa}$ .

$$\begin{pmatrix} \mathbf{N} \\ \mathbf{M} \end{pmatrix} = \begin{pmatrix} \mathbf{A} & \mathbf{B} \\ \mathbf{B} & \mathbf{D} \end{pmatrix} \begin{pmatrix} \boldsymbol{\varepsilon} \\ \boldsymbol{\kappa} \end{pmatrix} \quad (4.1)$$

However, as the considered laminates are symmetric, the extension-bending coupling matrix  $\mathbf{B}$  is a zero-matrix. Additionally, only extension, i.e. no bending is considered. Thus it is sufficient to look at the extensional matrix  $\mathbf{A}$  only.

$$\begin{pmatrix} N_1 \\ N_3 \\ N_{13} \end{pmatrix} = \mathbf{A} \begin{pmatrix} \varepsilon_{11} \\ \varepsilon_{33} \\ \varepsilon_{13} \end{pmatrix} \quad (4.2)$$

The extensional matrix  $\mathbf{A}$  is computed with the local constitutive matrices  $\mathbf{Q}_i^l$  from each ply transformed into the global coordinate system with the transformation matrices  $\mathbf{T}_i$  and the layer heights  $h_i$ .

$$\mathbf{A} = \sum_i (\mathbf{T}_i \mathbf{Q}_i^l \mathbf{T}_i^T) h_i \quad (4.3)$$

The local constitutive matrices are defined as

$$\mathbf{Q}_i^l = \frac{1}{1 - \nu_{TL_i} \nu_{LT_i}} \begin{pmatrix} E_{L_i} & \nu_{TL_i} E_{L_i} & 0 \\ \nu_{LT_i} E_{T_i} & E_{T_i} & 0 \\ 0 & 0 & G_{LT_i} (1 - \nu_{LT_i} \nu_{TL_i}) \end{pmatrix}, \quad (4.4)$$

where  $\nu_{TL_i} = \nu_{LT_i} E_{T_i} / E_{L_i}$ . The transformation matrices are given as

$$\mathbf{T}_i = \begin{pmatrix} c_i^2 & s_i^2 & 2s_i c_i \\ s_i^2 & c_i^2 & -2s_i c_i \\ -s_i c_i & s_i c_i & c_i^2 - s_i^2 \end{pmatrix}, \quad (4.5)$$

where  $c_i = \cos(\theta_i)$  and  $s_i = \sin(\theta_i)$ . Thus the strain  $\varepsilon_{11}$  can be found by inverting the extensional stiffness matrix  $\mathbf{A}$  and the given normal load  $N_1$ . The prescribed displacement  $\Delta$  is then computed with the normal strain  $\varepsilon$  and the length of the periodic model  $\hat{L}/2$ :

$$\Delta = \varepsilon_{11} \frac{\hat{L}}{2} = (\mathbf{A}^{-1} \mathbf{N})_1 \frac{\hat{L}}{2}, \quad (4.6)$$

where  $\mathbf{N} = (N_1, 0, 0)^T$  for uni-axial tension. Additionally the strains  $\varepsilon_{11}, \varepsilon_{33}, \varepsilon_{13}$  are required for the off-axis framework, in the far-field strain prescription  $\bar{\varepsilon}$  described in [Mik+21], where the additional degrees of freedom are avoided. The far-field strain prescription approach is however only valid if the defects don't affect the far-field strains significantly. In [Mik+21] it was applied to the simulation of tunneling crack growth of a finite number of cracks in infinitely long laminates and was thus appropriate. In the context of this work, the periodic cracks do have a non-negligible influence on the far-field. Instead of prescribing the far-field strains  $\bar{\varepsilon}$ , its work conjugate, the total far-field force  $\bar{\mathbf{N}}$  has to be applied. In the out-of-plane direction- $x_3$  the total far-field force, is simply the total applied force in the  $x_3$ -direction. In the in-plane direction,  $x_1$  (and  $x_2$ ) the total far-field force should be 0, as the loads are applied through conventional inhomogeneous finite element boundary conditions. The difference in the treatment of the in-plane and out-of-plane dimensions is due to the out-of-plane field being a fluctuation field, which is described in detail in [Mik+21]. Thus in the case of uni-axial loading, the entire total far-field force  $\bar{\mathbf{N}}$  is  $\mathbf{0}$ . In the context of uni-axial loading, the previous computation is obsolete. Here a prescribed displacement  $\Delta$  can be applied in the  $x_1$ -direction, while the far field force  $\bar{\mathbf{N}} = \mathbf{0}$  is set to zero. The axial normal force  $N_1$  can thereupon be extracted from the finite element model, where the other normal force components will remain zero.

As the cracks do have an impact on the structure, it will be noticed, that if the prescribed displacement is applied to the model with a crack present, a lower normal force will be observed, as the prescribed displacement was computed with classical laminate theory, which does not consider the defects. This is however not an issue, as it is exactly what is needed to describe the stiffness degradation.

For this task, a load  $N_1^0$  is to be applied to the model by estimating the prescribed displacement  $\Delta$ . However, when the prescribed displacement  $\Delta$  is applied to the right edge shown in fig. 11, the sum of the nodal reaction forces in the  $x_1$ -direction at the right edge  $N_1$ , i.e. the actual axial load will be lower if a crack is present. Thus the loss of axial stiffness due to the defect can be estimated with

$$\Delta E_1 = \frac{E_1}{E_1^0} = \frac{N_1 / \varepsilon_{11}}{N_1^0 / \varepsilon_{11}} = \frac{N_1}{N_1^0}. \quad (4.7)$$

#### 4.1.1.2 Force Based Load Application

Alternatively, the load can be applied directly with forces. In principle, the classical laminate theory computation can hereby be skipped. However, the stiffness estimation of the undamaged laminate still should be extracted to relate the stiffness degradation. For the uni-axial loading, the force  $N_1$  is applied to one node on the right edge, the reference node  $u_{\text{ref}}$  of the model shown in fig. 11. The remaining nodes on this edge are then constrained together, such that the displacement in the  $x_1$ -direction is identical. This is necessary to enforce the symmetry condition. It is achieved with a multi-point constraint, where for all nodes  $u_i$  at the right edge the following has to hold for the displacement in the  $x_1$ -direction.

$$u_{i_1} - u_{\text{ref}_1} = 0 \quad (4.8)$$

In Abaqus, this can be implemented using equations.

Simultaneously the total far-field force has to be applied, as described in the previous section, where  $\bar{\mathbf{N}} = \mathbf{0}$  for a uni-axial load. The advantage of this approach is, that it is more consistent when considering bi-axial loading, where a non-zero out-of-plane force  $\bar{\mathbf{N}}$  can be applied. This is not possible for the previous approach if large defects are present, as the applied in-plane strain has to match the out-of-plane force. So instead of dealing with a mixture of strains and forces under bi-axial loading, a pure force-based approach is recommended. Thus for the sake of generalisability of the model, the force-based load application is chosen for the model, despite the implementational overhead, due to the constraints. When considering the two approaches, special care has to be taken during the computation of the energy release rate, which will be explained in detail in section 5.1.2.

#### 4.1.1.3 Analytical Lower Bound

As described, the stiffness of an undamaged laminate can be computed with the classical laminate theory. A similar approach can be taken for the lower bound of the stiffness degradation. The stiffness degradation is due to the partial loss of the load-carrying capacity of the cracked layers. For a lower bound estimate, it is assumed, that the tunneling crack density or the delamination ratio are large enough to cause a full loss of the carrying capacity. Under this assumption, the classical laminate theory can be used. Here the stiffness contribution of the cracked ply is simply removed. This is also referred to as the ply discount method described in textbooks such as [DI94]. However, two different estimates can be made.

The first estimate, as described above, assumes, that the cracked layer loses its entire stiffness and will therefore be referred to as the lower ply discount bound. However, in principle, the crack, aligned with the fiber direction does not affect the stiffness in the direction of the fibers, i.e. the longitudinal stiffness. In the upper ply discount estimate<sup>1</sup>, only the transverse and shear stiffness

---

<sup>1</sup> It is referred to as an estimate, instead of a bound, as it does not bound the solution.

of the cracked layers are neglected. This is also the lowest possible stiffness degradation to be expected from the finite element model previously described.

One downside of the upper ply discount estimate is, that spurious effects occur for cracked layers oriented closely to the load-carrying direction, i.e. small angles  $\theta_c$ . Here the cracked laminate reaches a greater stiffness, than the uncracked laminate, as the loss of the transverse stiffness leads to the laminate not showing any resistance to the Poisson effect, i.e. the contraction in the out-of-plane direction.

This phenomenon is illustrated with the following isotropic example. A single isotropic ply with a unit height is considered. It is assumed, that the cracks are aligned with the  $x_1$ -direction, so that it only affects the transverse, i.e.  $x_2$ -components and the shear components. The constitutive matrix from eq. (4.4) can be rewritten as

$$\mathbf{Q} = \frac{1}{1-\nu^2} \begin{pmatrix} E & \nu(1-D)E & 0 \\ \nu(1-D)E & (1-D)E & 0 \\ 0 & 0 & (1-D)G(1-\nu^2) \end{pmatrix}. \quad (4.9)$$

Additionally, a damage parameter  $D$  was introduced for the transverse and shear stiffness contribution. The damage parameter is  $D = 0$  when the layer is uncracked and equivalent to the classical laminate theory and when  $D = 1$  the layer is fully damaged, i.e. no bearing capacity remains in the transverse and shear components. Inverting the matrix  $\mathbf{Q}$  leads to the compliance matrix  $\mathbf{C}$

$$\mathbf{C} = \mathbf{Q}^{-1} = \frac{1}{(1-(1-D)\nu^2)} \begin{pmatrix} \frac{1-\nu^2}{E} & \frac{-\nu(1-\nu^2)}{E} & 0 \\ \frac{-\nu(1-\nu^2)}{E} & \frac{1-\nu^2}{E} & 0 \\ 0 & 0 & \frac{1-(1-D)\nu^2}{(1-D)G} \end{pmatrix}. \quad (4.10)$$

A uni-axial load  $\mathbf{N} = (N_1, 0, 0)^T$  is applied and the normal strain in the  $x_1$ -direction  $\varepsilon_{11}$  can be extracted

$$\varepsilon = \begin{pmatrix} \varepsilon_{11} \\ \varepsilon_{33} \\ \varepsilon_{13} \end{pmatrix} = \mathbf{CN}. \quad (4.11)$$

Finally, the effective uni-axial stiffness  $E_1$  can be computed, where the load  $\mathbf{N}$  is equivalent to the applied stress  $\sigma$ , due to the assumption of the unit height.

$$E_1 = \frac{N_1}{\varepsilon_{11}} = \frac{(1-(1-D)\nu^2)E}{1-\nu^2} \quad (4.12)$$

For  $D = 1$ , the effective stiffness is simply equal to the stiffness of the material  $E$ , which is to be expected. However, when the damage increases, i.e. the damage parameter  $D$  decreases, the effective stiffness also increases, reaching a maximum at  $D = 1$

$$\lim_{D \rightarrow 1} E_1 = \frac{E}{1-\nu^2}. \quad (4.13)$$

This result is counter-intuitive and should be taken with a grain of salt, as it is most likely not what is encountered in the real structure. Furthermore, it is only in these extreme cases, when the cracks are aligned with the loading, that these spurious estimates occur. In the context of the laminate structures discussed in this thesis, this corresponds to very small angles in the off-axis layers  $|\theta| < 10^\circ$ , which is not commonly used in the industry anyway. Additionally, the cracks will most likely not occur in this form, as the energy release rates at these orientations for the tunneling crack propagation are either 0 or close to 0, as seen in [Mik+21] and [Mik+20].

#### 4.1.2. Verification

It is essential, that the model is verified before its application. There are two important aspects, that are to be verified in this section. First, it is ensured, that the computed results reach convergence for a refined mesh. Secondly, it has to be ensured, that the periodic model described in fig. 11 is equivalent to the full model described in fig. 10. For this purpose, the periodic boundary conditions have to be investigated.

##### 4.1.2.1 Convergence Study

The first verification step is a study of the mesh, where the convergence properties are studied. For this the mesh is refined, which is quantified by the smallest element length  $n_{EI}$  compared to the effective axial stiffness. The results are illustrated in fig. 12 for two crack densities  $\rho_c H = 1$  and  $\rho_c H = 6$  at three crack orientations  $\theta = 30^\circ$ ,  $\theta = 60^\circ$  and  $\theta = 90^\circ$ . The coarsest refinement consists of only 16 elements, whereas the finest refinement consists of 43'872 elements. A convergence is observed with a slight deviation for the coarser meshes. The relative error is

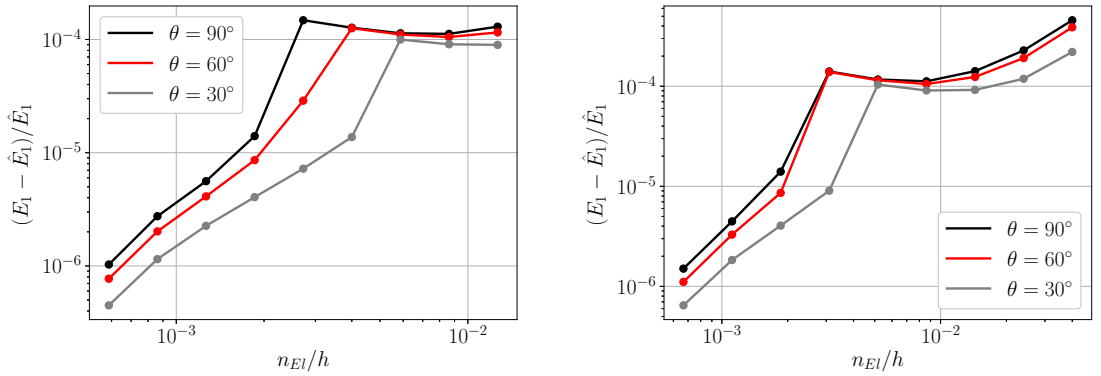


**Figure 12** Convergence study with axial stiffness  $E_1$  using the layup  $[0/\theta/0/-\theta_c]_s$  and the GlassFRP material from table 1. Left: Crack density  $\rho_c H = 1$  Right: Crack density  $\rho_c H = 6$

computed with the value obtained from the finest mesh  $\hat{E}_1$  and is always below 0.1%, even for the mesh consisting of only 15 elements. This indicates, that the stiffness, i.e. nodal reaction forces are insensitive to the level of refinement. The observed insensitivity of the reaction forces to the level of refinement is also expected, as is explained in textbooks like [Coo01].

#### 4.1.2.2 Periodic Boundary Conditions

As the periodic boundary conditions typically pose some complications and easily introduce errors to a finite element model they have to be verified. For this purpose a full model is created, i.e. the periodicity is no longer exploited and 100 cracks are modeled explicitly. The boundaries are constrained in the  $x_3$ -direction. Then the displacements at a crack located far from the boundary, i.e. of the 50<sup>th</sup> crack are compared to the displacements from the periodic model. This is done both at the crack and halfway between two cracks. The comparison is shown in fig. 13, where a good agreement is observed.

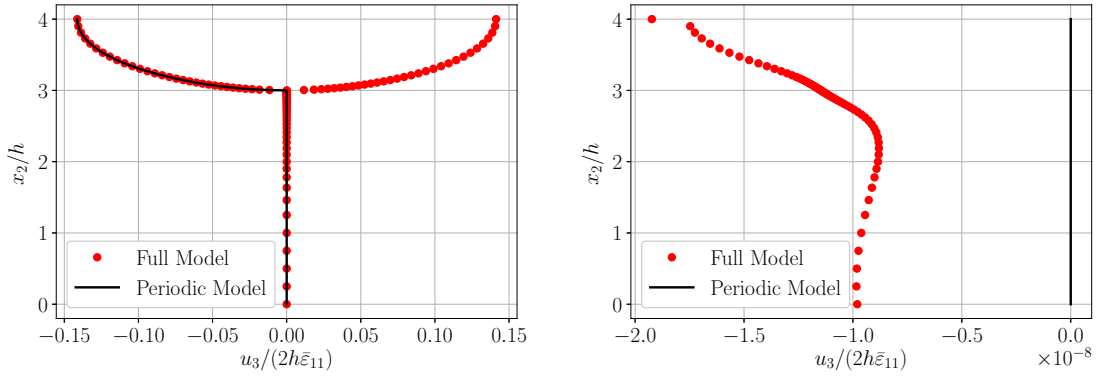


**Figure 13** Comparison of the normalized out of plane displacement  $u_3$  for the symmetric, but unbalanced layup  $[0/-45c]_s$  obtained by the periodic and full model. Left: Displacements at a crack. Right: Displacements halfway between two cracks.

The constraint in the  $x_3$ -direction at the boundary of the full model is questionable, as no physical meaning can directly be derived for it. However, its influence is probably negligible. This was investigated by varying the number of cracks modeled and a comparison to an unconstrained version, i.e. only a single node is locked to avoid rigid body movement. The results are shown in fig. 14 for  $\theta = 45^\circ$  and  $\theta = 15^\circ$ . The maximum observable difference is about 0.3%. Thus it can be concluded, that the influence is negligible and the periodic boundary conditions represent the full model to a satisfactory level.

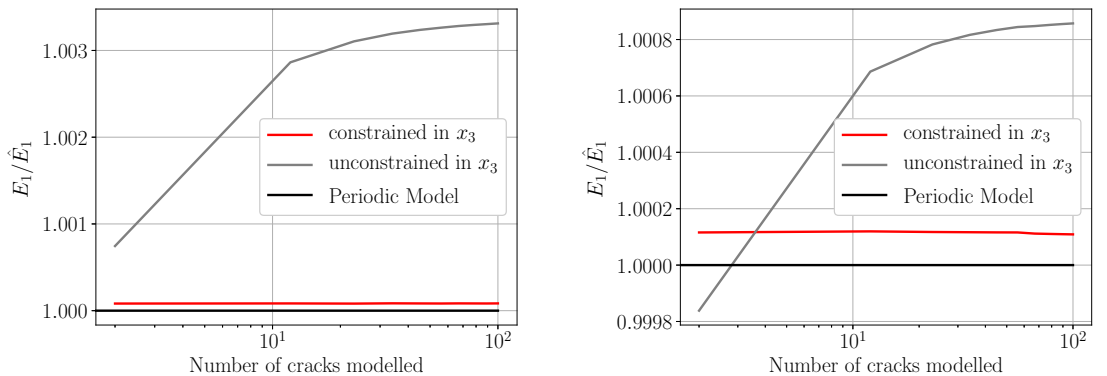


**Figure 14** Comparison of the axial stiffness  $E_1$  for the symmetric, but unbalanced layup  $[0/-\theta_c]_s$  obtained by the full model with edges constrained and not constrained in the  $x_3$ -direction. Additionally the result of the periodic model is illustrated. Left:  $\theta = 45^\circ$  Right:  $\theta = 15^\circ$

### 4.1.3. Validation

Next, the model has to be validated. This will be achieved stepwise with increasing complexity. Initially, an unbalanced laminate without cracks will be compared to the classical laminate theory. The reason being, that the off-axis framework from [Mik+21] has not been validated yet for shear deformations, that occur due to the extension-shear coupling terms being non-zero in unbalanced laminates.

Next five cases from literature have been selected, [Var+99], [McC96], [KMG06], [MCQ18] and [BCC13], which are listed in table 2 with their corresponding laminate setup. This is a mixture of experimental, analytical and numerical models.

**Table 2** Validation cases for the stiffness degradation.

Validation Case	[JV99]	[McC96]	[KMG06], [Kat+08]	[MCQ18]	[BCC13]
layup	$[\pm\theta/90_{4c}]_s$	$[\pm 45/0/90_c]_s$	$[0/45_c]_s$	$[0/45_c/ - 45]_s$	$[0/\theta_{4c}/ - \theta_4/\bar{0}]_s$
$E_L$ [GPa]	44.73	136.6	43.00	48.83	44.70
$E_T = E_{T'}$ [GPa]	12.76	9.790	13.00	14.07	12.70
$G_{LT} = G_{LT'}$ [GPa]	5.800	6.474	4.690	5.200	5.800
$G_{TT'}$ [GPa]	4.490	3.364	4.643	5.025	4.500
$\nu_{LT} = \nu_{LT'}$ [-]	0.2970	0.2860	0.3000	0.3080	0.2970
$\nu_{TT'}$ [-]	0.4200	0.4550	0.4000	0.4000	0.4111
ply thickness [mm]	0.1440	0.1250	0.6100 in 45°-ply 0.6400 in 0°-ply	0.6000	0.1440

Additionally, it has to be remarked, that six material properties are listed in table 2, which is not necessary as the materials are all transversely isotropic. Thus the following relation holds.

$$G_{TT'} = \frac{E_T}{2(1 + \nu_{TT'})} \quad (4.14)$$

Nevertheless, all six material properties are listed for the sake of convenience. Finally, the validity of the periodic assumption is investigated.

Furthermore, the ply thickness information is in principle obsolete for this thesis. This is achieved through a geometrical non-dimensionalization. The crack density  $\rho_c$ , commonly expressed in cracks per mm will always be defined in combination with the total laminate height  $H$ , i.e. as  $\rho_c H$  in a non-dimensional form. The only case, where additional information has to be provided, is if the layer thicknesses are varying, such as e.g. for the case [KMG06], [Kat+08]. However, typically, this can be expressed in relative terms in the layup definition. The benefit of the geometrical normalization is, that the results are independent of the layer height and are thus more generally applicable.

#### 4.1.3.1 Classical Laminate Theory

An unbalanced and undamaged laminate with the layup  $[-30_2/0/70_2]_s$  under a uni-axial tension load is investigated. The material used is the GlassFRP from table 1. A comparison between the global stresses  $\sigma_{11}$ ,  $\sigma_{33}$  and  $\sigma_{13}$  obtained with classical laminate theory and the periodic 2D finite element model is shown in fig. 15. The stresses are normalized with the applied load divided by the height  $N_1/H$ . A good agreement is observed with relative errors of less than 0.003%. This is an indication, that the additional shear term arising due to the unbalanced laminate does not cause an issue for the off-axis framework and this part of the framework will thus be considered validated.

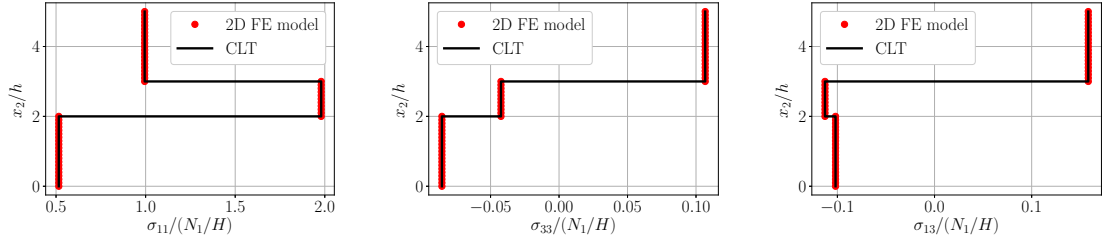


**Figure 15** Uni-axial validation case with classical laminate theory using a laminate with layup  $[-30_2/0/70_2]_s$ . The stresses are normalized with the applied load divided by the total height  $N_1/H$ . Left:  $\sigma_{11}$  Center:  $\sigma_{33}$  Right:  $\sigma_{13}$

#### 4.1.3.2 Tunneling Cracks Orientated at $90^\circ$

The next step is a validation with tunneling cracks orientated at  $90^\circ$ . Here the off-axis framework is equivalent to a generalized plane strain model, as discussed in [Mik+21]. A plane strain model can be seen in [LV05]. For this purpose, the first two columns from table 2 will be used. The first, [Var+99] is a dataset obtained from experiments and the second [McC96] is from an analytical model, the so-called stress transfer model. The comparison is illustrated in fig. 16 and a satisfactory agreement is observed. The experimental data agrees very well with the periodic model, whereas the analytical model deviates slightly for greater crack densities  $\rho_c$ . However the deviation observed at  $\rho_c H = 1$  are still very small, about 0.04%. Additionally, it is seen, that the stiffness degradation converges towards the upper ply discount estimate with an increasing crack density  $\rho_c$ .

#### 4.1.3.3 Arbitrarily Orientated Tunneling Cracks

Until now the off-axis framework has not been employed for its true purpose. The real benefit is for off-axis cracks with arbitrary orientations, i.e.  $\theta \neq 90^\circ$ . Therefore it is essential to ensure its accuracy for these cases. For this task, three validation cases have been selected and are listed in the last three columns of table 2.

First a dataset from experiments conducted by [KMG06], [Kat+08] is used as validation. Additionally [MCQ18] have used the same model to validate their 3D periodic finite element model.

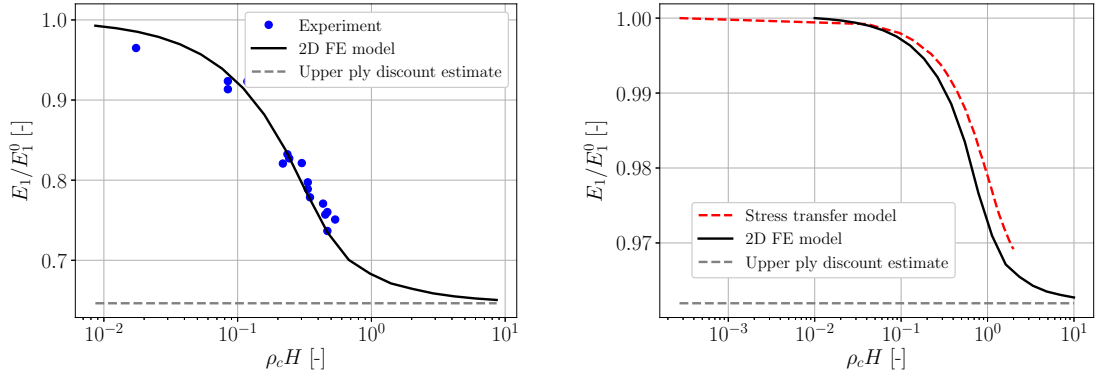


**Figure 16** Comparison of periodic off-axis model to experimental and analytical values. Left: Comparison to experiment from [JV99] using the layup  $[\pm 0/90_{4c}]_s$ . Right: Comparison to analytical stress transfer model from [McC96] using the layup  $[\pm 45/0/90_c]_s$ .

Thus a comparison with both data-sets can be made and is shown in fig. 17. The laminate with the layup  $[0/45_c]_s$  is additionally unbalanced, which leads to a coupling between shear and extension. Nevertheless, the model still seems to perform well. The experimental data lies in-between the 2D and 3D finite element models. It is however surprising, that the 2D and 3D models deviate up to about 1.5%. It is however difficult to explain the differences and to conclude, which model describes the problem better. Again, it is observed, that the 2D model converges towards the upper ply discount estimate.

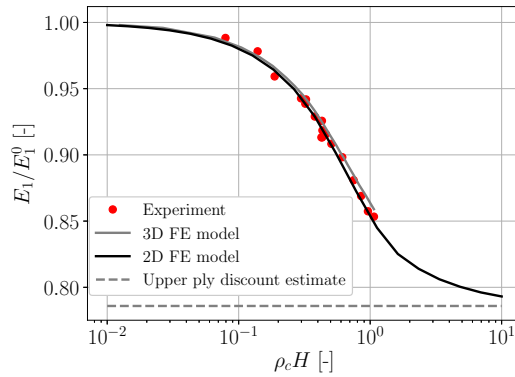


**Figure 17** Comparison of model to experimental values from [KMG06], [Kat+08] using the layup  $[0/45_c]_s$ . Additional comparison to results from a periodic 3D Finite element model by [MCQ18].

Next another comparison with the 3D periodic model by [MCQ18] is conducted with a balanced layup  $[0/45_c / -45]_s$ . The result is depicted in fig. 18 and the models seem to agree better. This could be an indication, that the previous deviation might occur due to the unbalanced laminate, which emphasizes the possible differences in the boundary effects. It is however difficult to deduce this from only two cases and overall the agreement is still satisfactory. A reason against this hypothesis is, that this balanced laminate also becomes unbalanced for a larger crack density  $\rho_c$ , i.e. when it approaches the upper ply discount estimate. Thus in principle all layups can be considered unbalanced beyond a certain crack density threshold.

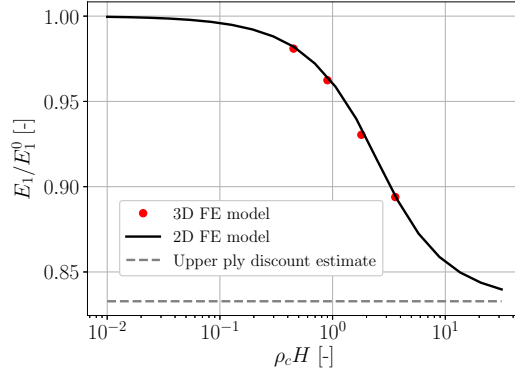


**Figure 18** Comparison of model to values obtained with a periodic 3D Finite element model by [MCQ18] using the layup  $[0/45_c/-45]_s$ .

Finally another 3D periodic model from [BCC13], who proposed the following benchmark, is used as comparison. Here the layup  $[0/\theta_{4c}/-\theta_{4c}/\bar{0}]_s$  is used, which originates from [Var+99], where a  $[0/\theta_{4c}/-\theta_{4c}/\bar{0}]_s$  was used. The difference is, that [BCC13] only uses a single cracked ply. The result is listed in fig. 19 for both  $\theta = 55^\circ$  and  $\theta = 70^\circ$ . For both cases the models agree very well throughout the data-set. It is also surprising, that the stiffness curves of both cases are almost identical and do not seem to be dependent on the orientation  $\theta$ . Therefore the influence of the orientation  $\theta$  will later be investigated in a parametric study. Both models also converge towards the upper ply discount estimate.

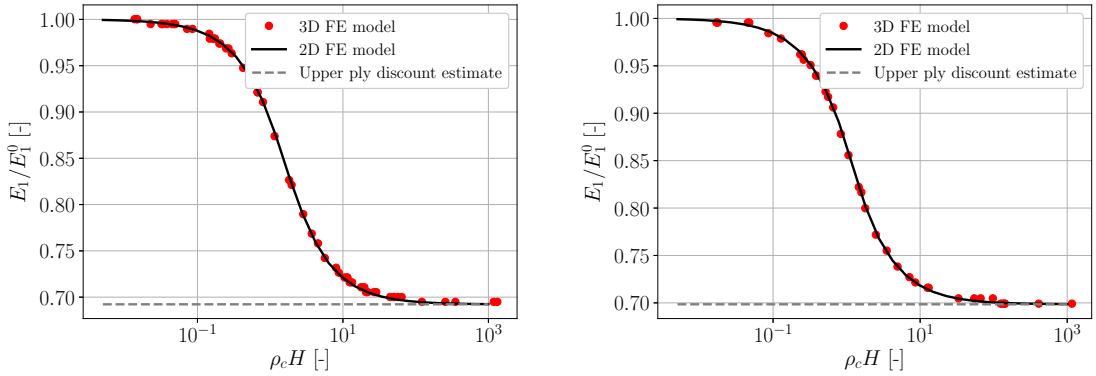


**Figure 19** Comparison of model to values obtained with a periodic finite element mode by [BCC13] using the layup  $[0/\theta_{4c}/-\theta_{4c}/\bar{0}]_s$ . Left:  $\theta = 55^\circ$ . Right:  $\theta = 70^\circ$ .

Another interesting aspect in the comparison with [BCC13] is the computational effort. The 3D periodic model takes about 2000 s on average per simulation, whereas the developed 2D model only takes about 20 s on average for models with about 1600 2D elements on the DTU wind energy cluster<sup>2</sup>. It has to however also be noted, that the comparison is not unflawed, as the computations with the 3D model are from 2013 and it is unknown, which hardware was used. However, it is likely, that their finite element code did exploit parallelization, which is not the case for the 2D model running only on a single node of the CPU.

<sup>2</sup> AMD EPYC 7351 (2.9 GHz) processor with 16 cores

#### 4.1.3.4 Periodicity of the Model

The assumption of a periodic distribution of the cracks is an idealization based on empirical observations. However, the periodic alignment of the cracks will not be exact in a real specimen. Thus the influence of an imperfect periodic distribution is investigated. For this purpose, a Gaussian distribution is used to sample the crack spacing  $L$  given a mean crack spacing  $\mu_L$  and a standard deviation of the crack spacing  $\sigma_L$ . For every standard deviation, 20 samples with 20 cracks each are taken and used to compute the stiffness degradation  $\Delta E_1$ . From the 20 stiffness degradation values the corresponding mean  $\mu_{\Delta E_1}$  and standard deviation can be approximated  $\sigma_{\Delta E_1}$ . The results for the average crack densities  $\rho_c H = 1$ ,  $\rho_c H = 2$  and  $\rho_c H = 3$  for  $\theta = 90^\circ$  are shown in fig. 20.

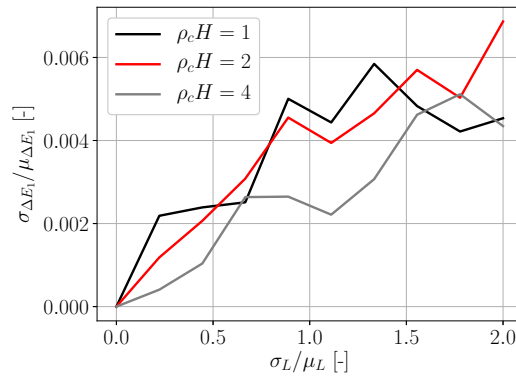


**Figure 20** Stochastic investigation of the effect of irregularly spaced tunneling cracks on the stiffness degradation using the layup  $[-90_c/0/90/0]_s$ .

The normalized standard deviation of the stiffness degradation reaches about  $\sigma_{\Delta E_1} / \mu_{\Delta E_1} = 0.006$  for the normalized standard deviation of the crack spacing  $\sigma_L / \mu_L = 2$ . This is deemed sufficient, as the irregularity expressed by such a standard deviation already exceeds the observed regularity in e.g. [CMQ19] or [QC14]. For illustration purposes, an example of a crack distribution with  $\sigma_L / \mu_L = 2$  is provided in fig. 21. This degree of irregularity does not influence the stiffness degradation strongly. Thus the usage of the periodic model is validated in the case of the stiffness degradation. Ideally, a similar study should be conducted for the crack propagation in the following sections, which is however not done, as it is difficult to determine the choice of crack for the propagation. It is however expected and therefore assumed here, that the assumption of the periodicity is also valid for the crack propagation computations.

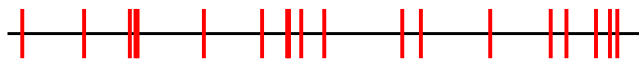


**Figure 21** Example tunneling crack distribution with  $\sigma_L / \mu_L = 2$ .

#### 4.1.4. Results

After the successful verification and validation, the model can now be applied to different cases. Here the laminate with the layup  $[0/\theta/0/ -\theta_c]_s$  and the two materials GlassFRP and CarbonFRP

from table 1 will be investigated. First, the dependency of the stiffness degradation on the angle  $\theta$  is looked at. The results are presented in fig. 22, where the stiffness degradation is shown for different tunneling crack densities  $\rho_c$ . It is seen, that the orientation influences the stiffness degradation, where it is typically greatest for angles greater than  $45^\circ$ . This is to be expected, as for smaller angles, the cracks are aligned more closely to the loading direction and thus don't affect the axial stiffness degradation as much, as explained in section 4.1.1.3. Furthermore, it is seen, that the simulation results converge towards the upper ply discount estimate for angles greater than  $10^\circ$ . It is surprising, that the finite element model does not capture the spurious effect of the stiffness increase for angles below  $10^\circ$ , which was explained in section 4.1.1.3. This is however not a concern, as on the one side the model will most likely not be applied for such small angles and on the other side, these effects do not necessarily make physical sense. Thus, even though the discrepancy is not explained, it is favorable, that the finite element model does not lead to a stiffness increase for small angles.

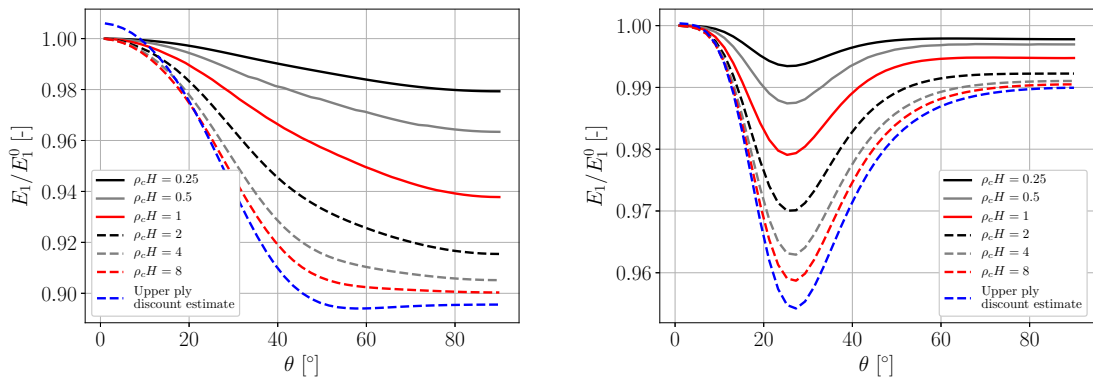


**Figure 22** Influence of the orientation  $\theta$  on the axial stiffness degradation for the layout  $[0/\theta/0/-\theta_c]_s$ . Left: GlassFRP. Right: CarbonFRP.

As no significant difference between the cases  $\theta = 55^\circ$  and  $\theta = 70^\circ$  was observed for the layout  $[0/\theta_{4c}/-\theta_4/\bar{0}]_s$  in fig. 19, the parametric study with the orientation  $\theta$  is repeated for this layout. The result is depicted in fig. 23. Here it is observed, that there is a clear dependency with respect to the orientation  $\theta$ . However, the difference at  $\theta = 55^\circ$  and  $\theta = 70^\circ$  is very small.

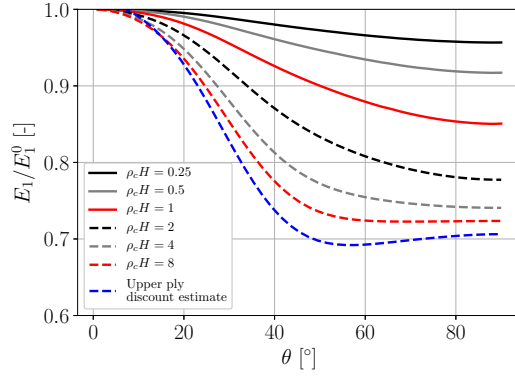


**Figure 23** Influence of the orientation  $\theta$  on the axial stiffness degradation for the layup  $[0/\theta_{4c} / -\theta_4/\bar{0}]_s$  from [BCC13].

Finally, the influence of the tunneling crack density  $\rho_c$  for the layup  $[0/\theta/0 / -\theta_c]_s$  is analyzed and shown in fig. 24 for the angles  $\theta = 30^\circ$ ,  $\theta = 60^\circ$  and  $\theta = 90^\circ$ . A similar tendency as in the validation cases is observed with an initial stiffness fall, which then slowly converges towards an upper ply discount. Here it is however observed, that the convergence is not ideal with a maximum relative error of 0.2% between the converged value and the upper ply discount estimate occurring for  $\theta$  with the GlassFRP material. It is however still greater than the lower ply discount bound.

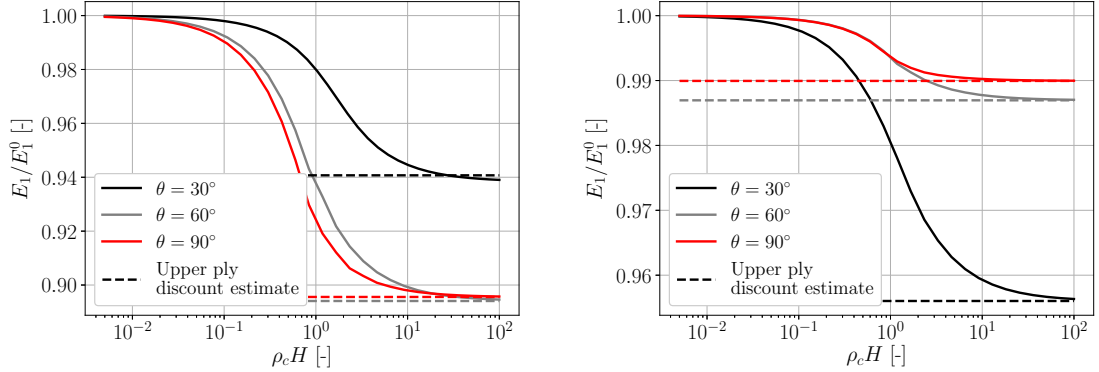


**Figure 24** Influence of the tunneling crack density  $\rho_c$  on the stiffness degradation for the layup  $[0/\theta/0 / -\theta_c]_s$ . Left: GlassFRP. Right: CarbonFRP.

## 4.2. Delamination Cracks

The model from section 4.1 is now extended to include delamination cracks. Thus this section will be concerned with both the stiffness degradation due to the tunneling cracks and the delamination cracks. First, the extension of the model is described. Then the model is verified and validated. Finally, parametric studies are conducted to show the effect of both tunneling cracks and delamination cracks on the axial stiffness.

#### 4.2.1. Model Description

As seen in section 2.2 the delamination cracks are caused by the stress concentrations at the tip of the tunneling cracks. It, therefore, does not make sense to create a delamination model without the tunneling cracks. Thus the model from section 4.1 can be extended slightly to include the delamination. This is illustrated in fig. 25, which can be compared to the original model without delamination in fig. 11. Here the difference, i.e. the delamination with length  $d_r(\hat{L}/2)$ , is marked in blue, where  $d_r$  is the delamination ratio. The delamination ratio indicates the relative amount of delamination, that has occurred and is thus 0 for no delamination and 1 for full separation. In the context of finite elements, this seam can be modeled easily by disconnecting the mesh at the interface.

It also has to be noted, that the model still exploits the symmetries in both the  $x_1$ - and  $x_2$ - direction. Thus only an H-shaped delamination can be studied when exploiting both symmetries. The model could however be easily extended to model all delamination configurations discussed in fig. 7. For this, the full height of a full period has to be modeled, instead of only a half-height of a half period. This is however not done in this thesis, as the H-shaped delamination is the most common and the stiffness drop due to the delamination is considerably less than for the tunneling crack, as seen in fig. 2. It is also questionable if a different delamination configuration with the same delamination ratio would result in large deviations. This could be answered with future investigations.

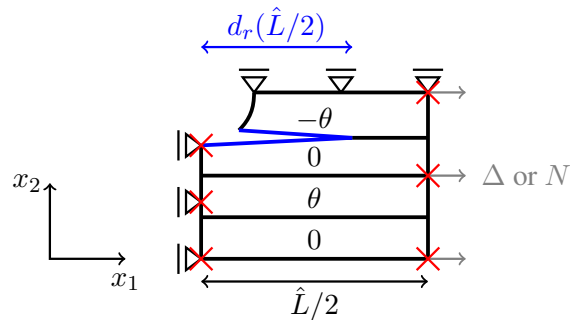


**Figure 25** The deformed periodic model with boundary conditions. The roller supports restrict the degrees of freedom in the  $x_1$  or  $x_2$  dimension, whereas the red crosses restrict the displacement in the  $x_3$ -direction. The gray arrows indicate a prescribed displacement or force. The delamination is marked in blue and is implemented disconnecting the mesh at the interface.

Another aspect, that is not clear in the deformed laminate shown in fig. 25 is the opening in the  $x_2$ -direction of the delamination crack. In fact, the crack will usually only open, for lower delamination ratios. This is also the case for isotropic plies as is illustrated in fig. 26, where overlap occurs for a delamination ratio of  $d_r = 0.75$ . To take this effect into account, contact, and friction should be modeled at the interface.

However, [DS91] has discussed this problem for isotropic layers and [SF04] for orthotropic layers. They conclude, that the overlap is small and its influence is negligible. When taking the contacts influence with contact mechanics [WL07] into account [DS91] noticed that it was within 2.5% and 6% for the stress intensity factors, i.e. the crack propagation. It mainly influences the mode I

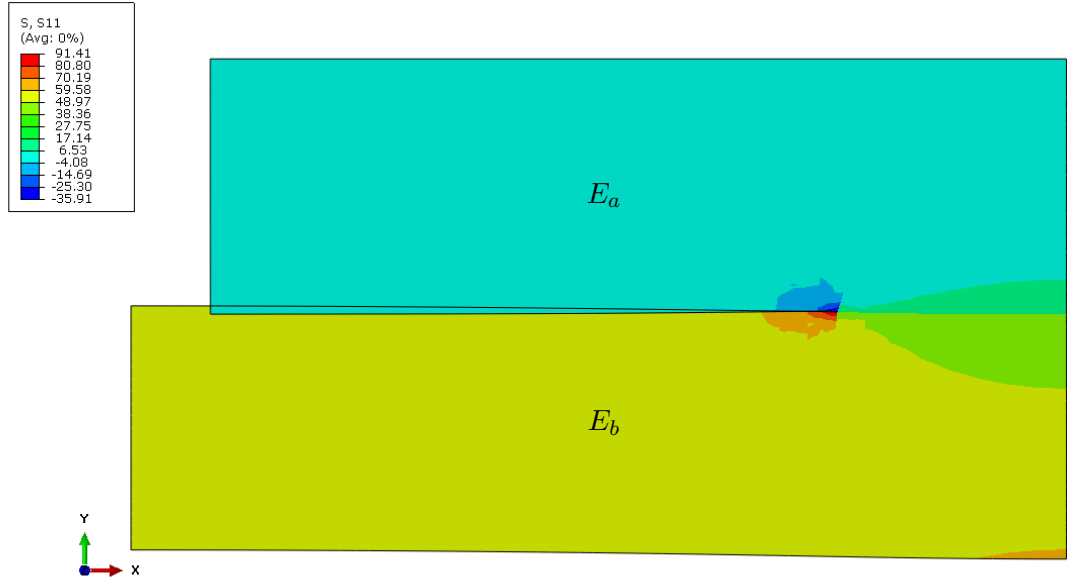


**Figure 26** Example of two isotropic layers with delamination leading to overlap at the interface. The crack density is  $\rho_c = 0.5 \text{ mm}^{-1}$ , the layer thickness  $h = 0.3 \text{ mm}$ , the delamination ratio  $d_r = 0.75$  and the stiffness ratio  $E_b/E_a = 5$ .

crack growth, which is less significant than the mode II crack growth and not affected as much by the contact. A similar investigation was conducted by [CMQ19] for fiber-reinforced composites with tunneling cracks. Thus contact will be neglected in this thesis.

The computation of the axial stiffness degradation will use the same procedure as described in section 4.1, where the reaction forces are used together with eq. (4.7).

#### 4.2.2. Verification

Once again, the model has to be verified. As the model is a direct extension from the model described in section 4.1, the verification is less thorough. The periodic boundary conditions are identical to the previous model and the verification is thereby not repeated for these. However a convergence study is again conducted to ensure convergence of the computations for refined meshes.

##### 4.2.2.1 Convergence Study

A convergence study is conducted to ensure the reliability of the results. The mesh is refined using the smallest element length  $n_{EI}$ , whereupon the axial stiffness  $E_1$  is extracted. It is then normalized with the axial stiffness  $\hat{E}_1$  obtained with the most refined mesh. The results are illustrated in fig. 27 using the layup  $[0/45_c/-45]_s$  at a crack density of  $\rho_c H = 1.8$ . Three delamination ratios  $d_r = 0.1$ ,  $d_r = 0.3$  and  $d_r = 0.5$  are checked. The number of elements ranges from 6 to 78'435 and the convergence tendencies are satisfactory. Again, the axial stiffness does not seem very sensitive to the level of mesh refinement.

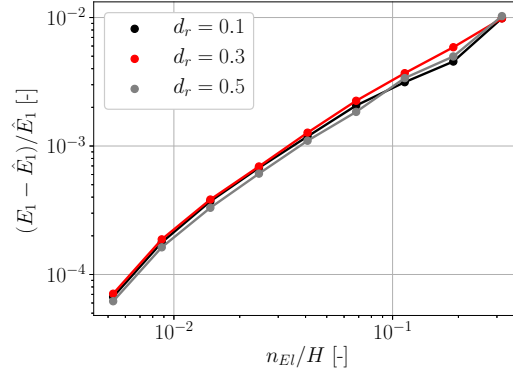


**Figure 27** Convergence study with axial stiffness  $E_1$  using the layup  $[0/45_c/ - 45]_s$  with a crack density of  $\rho_c H = 1.8$  and the material from [McC96] shown in table 2.

#### 4.2.3. Validation

The model is now to be validated. However the amount of data and models concerning the stiffness degradation, due to delamination, is very sparse. The only model found was by [MCQ18] where they use their 3D periodic finite element model. They however provide their stress data in the cracked ply, which can be used for a more detailed validation. This comparison is conducted for two laminates with layups  $[0/90_c]_s$  and  $[0/45_c/ - 45]_s$  and illustrated in fig. 28. The material is listed in table 2. The data points marked in red are from the 3D model, whereas the black lines are obtained with the 2D model. Additionally, the stress state of the undamaged laminate is shown with a gray dashed line and obtained with classical laminate theory. Also, the vertical dotted gray lines indicate the tip of the delamination crack. Overall a good agreement is observed. The slight differences could possibly be explained with the extraction and averaging of the stresses, which introduces both interpolation and numerical errors. It is however difficult to assert the difference, as the procedure is not described in detail by [MCQ18]. In this work, a path is created along the nodes and the nodal stress values, i.e. the interpolated stress values are extracted and then integrated with the trapezoidal rule. A better approach would be an extraction at the Gauß points and a second-order integration scheme, which is not done, due to practical reasons and an already satisfactory agreement. As the stresses seem to fit relatively well, the stiffness degradation can also be compared. Here the same laminate with layup  $[0/45_c/ - 45]_s$  is used and the results are illustrated in fig. 29. The values coincide very well, even though the stiffness degradation is relatively small. The relative errors are very small, being bounded by 0.2%.

Although the validation for the delamination is not as strong as for the tunneling cracks, it is deemed sufficient to investigate the stiffness degradation caused by the combination of tunneling cracks and delamination cracks. This is because the overall tendencies agree with the model by [MCQ18] and the underlying tunneling crack model was validated to a satisfactory degree.

#### 4.2.4. Results

The validated model is now to be applied to the laminate with the layup  $[0/\theta/0/ - \theta_c]_s$  and the two materials GlassFRP and CarbonFRP from table 1. First the influence of both the tunneling

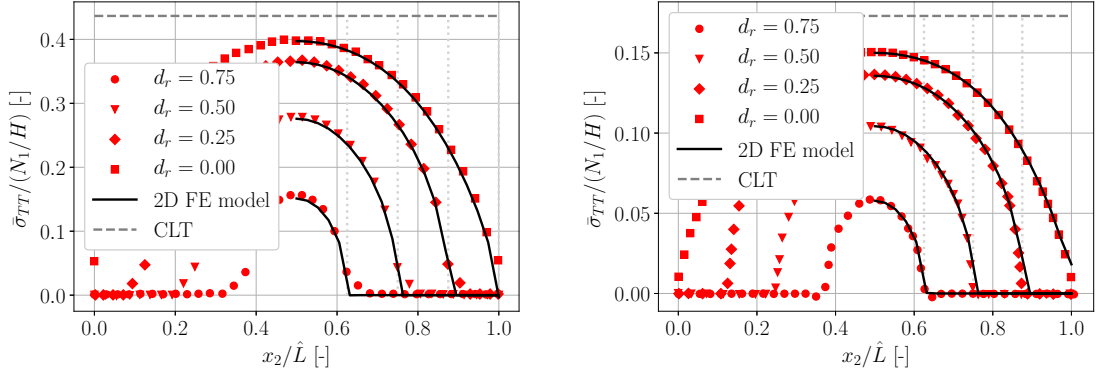


**Figure 28** Comparison of the local transverse stresses  $\bar{\sigma}_{TT}$ , averaged through the thickness of the cracked ply with results obtained in [MCQ18]. The load applied to the laminate is  $N_1 = 100$  MPa. In both cases the tunneling crack density is  $\rho_c = 0.5 \text{ mm}^{-1}$ . Left: The layup is  $[0/90_c]_s$  with a ply thickness of  $h = 0.3$  mm. Right: The layup is  $[0/45_c/-45]_s$  with a ply thickness of  $h = 0.6$  mm.

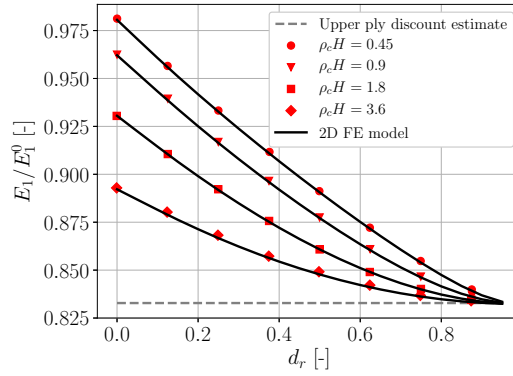


**Figure 29** Comparison with values obtained with a periodic 3D Finite element by [MCQ18] using the layup  $[0/45_c/-45]_s$ . The stiffness degradation as function of the delamination ratio.

crack density  $\rho_c$  and the delamination ratio  $d_r$  on the stiffness degradation are analyzed. These are illustrated as contour plots in fig. 30. The maximal stiffness degradation can again be compared to the upper ply discount estimate, which unfortunately is surpassed slightly. For GlassFRP the bound is passed by 0.5% for  $\theta = 30^\circ$  and by 0.2% for  $\theta = 60^\circ$ , and for CarbonFRP the bound is passed by 0.9% for  $\theta = 30^\circ$  and by 0.6% for  $\theta = 60^\circ$ . Again it is surprising, that this bound is passed and a satisfactory explanation has not been found.

However, the errors are still small enough, such that the model can be used. In particular, the contour plots in fig. 30 are useful for assessing the internal damage of a composite from a measurement. If a measurement of a stiffness degradation is given, one can identify a contour line, which provides the possible combinations of tunneling crack densities  $\rho_c$  and delamination ratios  $d_r$ . Combined with a measurement of the crack density, the delamination ratio can uniquely be identified.

An alternative to a measurement of the crack density is a measurement of the out-of-plane stiffness degradation that can be obtained by performing an axial test of the  $90^\circ$ -rotated laminate,

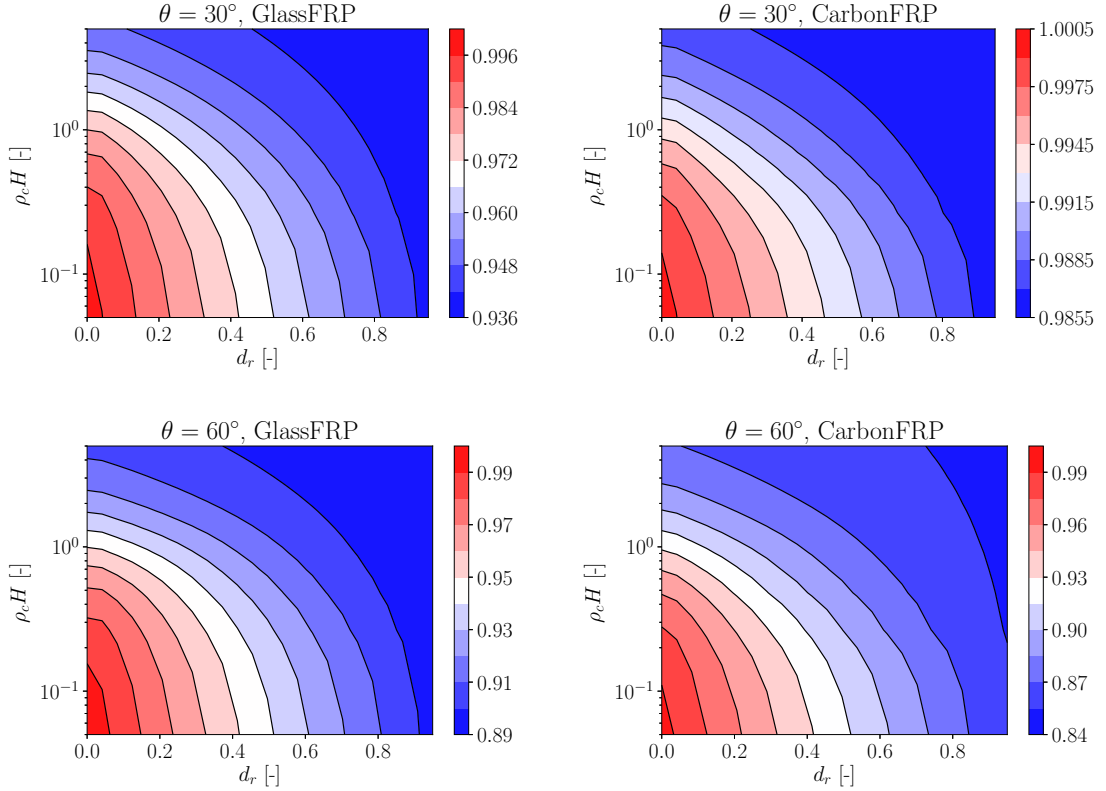


**Figure 30** Influence of the tunneling crack density  $\rho_c$  and the delamination ratio  $d_r$  on the stiffness degradation for the layup  $[0/\theta/0/-\theta_c]_s$ . Left: GlassFRP,  $\theta = 30^\circ$  upper ply discount estimate: 0.941,  $\theta = 60^\circ$  upper ply discount estimate: 0.894. Right: CarbonFRP,  $\theta = 30^\circ$  upper ply discount estimate: 0.928,  $\theta = 60^\circ$  upper ply discount estimate: 0.896.

which can then also be used in combination with a contour plot of the corresponding stiffness degradation. This will yield a second contour line. The intersection of these two contour lines might then yield a unique solution to the tunneling crack density and the delamination ratio. To illustrate this procedure a contour plot of the layup  $[0/\theta/0/-\theta_c]_s$  rotated by  $90^\circ$ , i.e. with the layup  $[90/\theta + 90/90/-\theta + 90_c]_s$  is provided in fig. 31.

The contour lines of the layup  $[0/30/0/-30_c]_s$  from fig. 30 and the contour lines of the layup  $[90/120/90/-120_c]_s$  from fig. 31 can then be combined to yield a contour line plot, which could be used to identify the internal damage from experiments for the layup  $[0/30/0/-30_c]_s$ . This is illustrated in fig. 32. These plots are computationally cheap to generate with the given framework and potentially useful to estimate the internal damage of laminates in a non-destructive manner. To illustrate the proposed method, consider the axial stiffness degradation measurement in the  $x_1$ -direction of 0.972 and the measurement in the  $x_3$ -direction of 0.875. Using fig. 32, a tunneling crack density of  $\rho_c H = 0.16$  and a delamination ratio of  $d_r = 0.375$  can uniquely be identified. This is potentially useful in cases, where the internal damage parameters, i.e. the tunneling cracking density and the delamination ratio, are to be identified from bi-axial fatigue measurements. Note however, that this only works, if no other damage mechanisms occur.

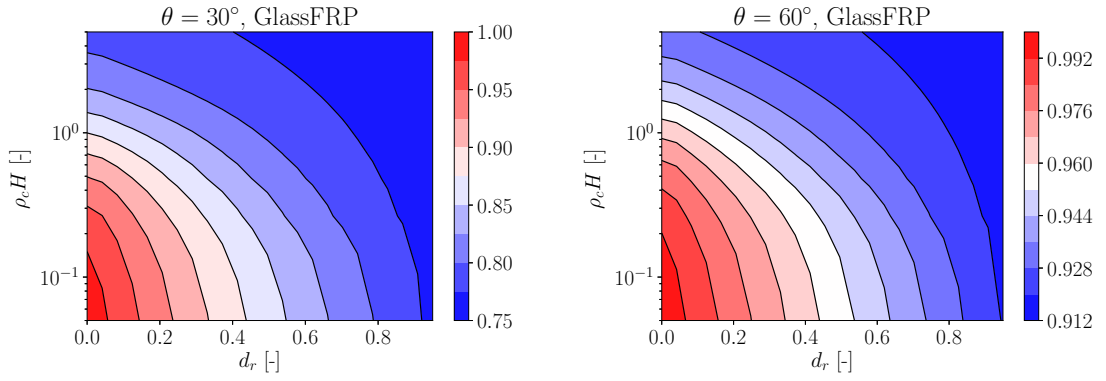


**Figure 31** Influence of the tunneling crack density  $\rho_c$  and the delamination ratio  $d_r$  on the axial stiffness degradation for the rotated layup  $[90/\theta + 90/90/-\theta + 90c]_s$ . Left: Rotated layup  $[90/60/90/-60c]_s$  with GlassFRP. Right: Rotated layup  $[90/30/90/-30c]_s$  with GlassFRP

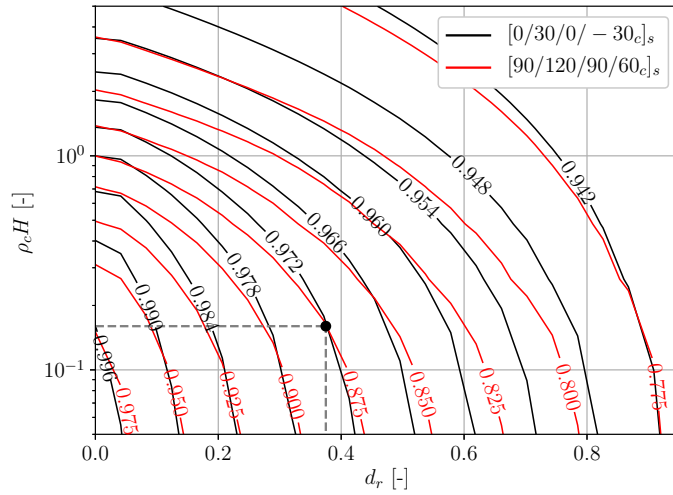


**Figure 32** The axial stiffness degradation of the layup  $[0/30/0/-30c]_s$  marked in black and of the layup  $[90/120/90/60c]_s$ , equivalent to  $[90/60/90/-60c]_s$  marked in red is shown.

Furthermore it has to be noted, that a unique solution is not always guaranteed. In the case of a layup that is invariant with respect to the  $x_1$ - and  $x_3$ -direction, this is not possible.

Additionally a parametric study with respect to the orientation  $\theta$  is conducted with the material CarbonFRP and shown in fig. 33. Similar as in fig. 22, the stiffness degradation is smallest for small angles  $\theta$ . Again, the upper ply discount estimate provides a lower bound for the results with the exception of the small angles  $|\theta| < 10^\circ$ . Furthermore, it is seen, that as the delamination ratio and the tunneling crack rate increase, the stiffness curves converge to the same line.

Finally, also the influence of the ply thickness in the off-axis layers  $h_\theta$  is investigated and illustrated in fig. 34. As expected the stiffness degradation converges towards 0 for a large ply thickness  $h_\theta$  and 1 for a small ply thickness  $h_\theta$ . Additionally, the upper and lower ply discount

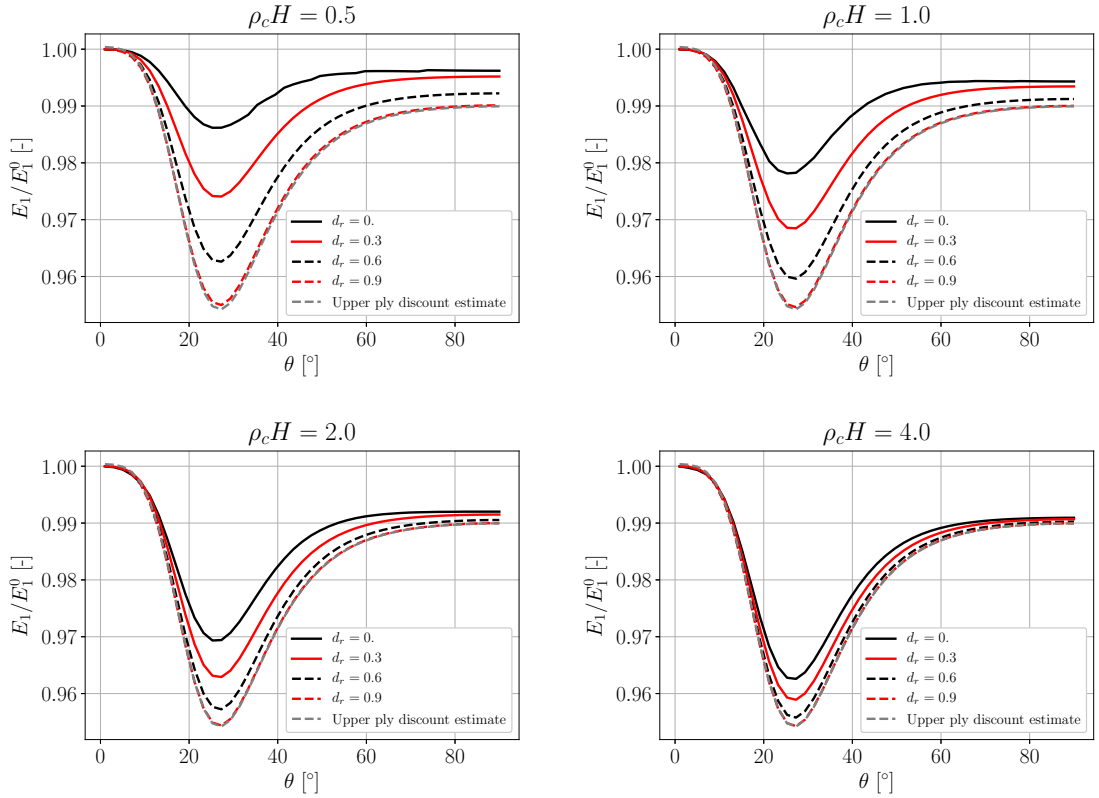


**Figure 33** Influence of the orientation  $\theta$ , the tunneling crack density  $\rho_c$  and the delamination ratio  $d_r$  on the stiffness degradation for the layup  $[0/\theta/0/-\theta_c]_s$  with the material CarbonFRP.

bounds are shown. Again, the upper ply discount estimate is breached slightly. However, the lower ply discount bound should under no circumstances be violated, which is also not the case. Furthermore, it is observed, that the curves tend to converge towards each other for a greater delamination ratio  $d_r$ , which is also to be expected, as the damage saturates and no further stiffness degradation can occur. The converged line is approximately the upper ply discount estimate.

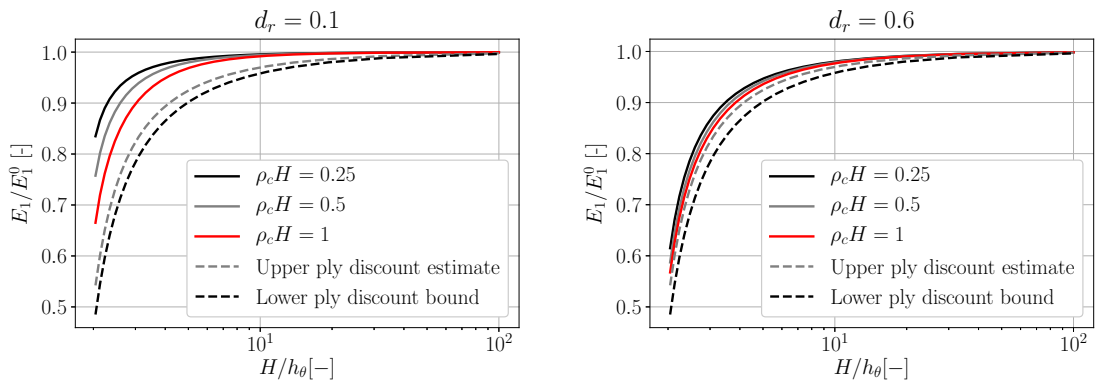


**Figure 34** Influence of the off-axis layer thickness  $h_\theta$  on the stiffness degradation for the layup  $[0/\theta/0/-\theta_c]_s$  with the material GlassFRP and  $\theta = 45^\circ$ . Left: Delamination ratio  $d_r = 0.1$ . Right: Delamination ratio  $d_r = 0.6$ .

## 5. Delamination Propagation

As described in section 2.6 delamination is an important part of the failure process in fiber-reinforced composites. Specifically, the second stage shown in fig. 3 is dominated by the delamination. Hence it is of interest to not only understand the effect of the delamination on the material properties but also to understand the circumstances under which the delamination occurs and propagates. Especially, a comparison between the delamination propagation and the tunneling crack propagation is of interest, i.e. to identify when which propagation occurs. Finally, the crack propagation properties are related to the fatigue behavior of the laminates.

### 5.1. Model Description

The model from chapter 4 will be reused and extended to accommodate the computation of the energy release rate for the delamination propagation. For the energy release rate computation, the virtual crack closure technique was chosen. The energy release rate can then be used to estimate the crack growth rate, which then can be used to predict the crack length at each cycle and thereby the fatigue life. For this task, Paris-like power laws are used.

#### 5.1.1. Virtual Crack Closure Technique

The least invasive approach, that simultaneously only requires a single simulation per crack increment is the virtual crack closure technique [Kru04] and was explained briefly in fig. 8. Here the energy release rate  $\mathcal{G}$  is computed with the change in potential energy, which is approximated at the crack tip. For this, the crack opening displacement  $\Delta u$  for the propagated state and the stress state  $\sigma^0$  for the non-propagated crack are to be used, as shown in eq. (2.10). This corresponds to the crack closure integral, whereas in the virtual crack closure technique the stress state  $\sigma^0$  is approximated by the stress state in front of the crack, as shown in eq. (2.11).

The integral from eq. (2.11) can be simplified even further for each element type. In this case, elements with quadratic shape functions are used. A crack along the  $x_1$ -axis is illustrated in fig. 35. The black dots indicate the nodes, whereas the black vertical dashed lines indicate the vertical element boundaries. The current crack with length  $a$  is shown in red and the incremented crack with length  $a + \Delta a$  is shown with the dashed gray line. The integral can now be replaced by the nodal quantities of the model, i.e. the crack opening displacements  $\Delta u_{2i}$ ,  $\Delta u_{2i+1}$  and the reaction forces  $F_{2i+2}$ ,  $F_{2i+3}$ . Hence the integral can be evaluated numerically with a summation over the nodal quantities.

$$\mathcal{G}_I = -\frac{1}{2\Delta a}(\Delta u_{2i} F_{2i+2} + \Delta u_{2i+1} F_{2i+3}) \quad (5.1)$$

The same principle applies for the fracture modes II and III.

$$\mathcal{G}_{II} = -\frac{1}{2\Delta a}(\Delta u_{1_i} F_{1_{i+2}} + \Delta u_{1_{i+1}} F_{1_{i+3}}) \quad (5.2)$$

$$\mathcal{G}_{III} = -\frac{1}{2\Delta a}(\Delta u_{3_i} F_{3_{i+2}} + \Delta u_{3_{i+1}} F_{3_{i+3}}) \quad (5.3)$$

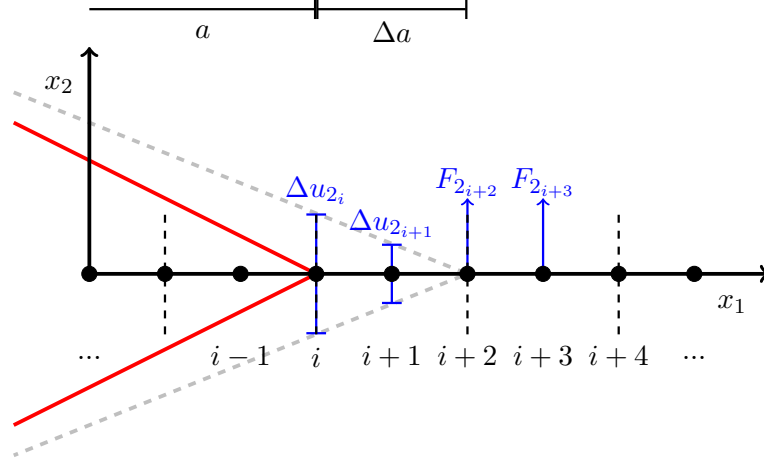


**Figure 35** Schematic illustrating the virtual crack closure technique for crack propagation along the  $x_1$ -axis modeled with quadratic elements. The elements are indicated by the vertical dashed lines, whereas the nodes are represented by black dots. The current crack with length  $a$  is shown in red and the propagated crack with length  $a + \Delta a$  is shown with the dashed gray line. The mode I energy release rate  $\mathcal{G}_I$  can be computed with the nodal crack opening displacements  $\Delta u_2$  and the nodal reaction forces  $F_2$ . The energy release rates for mode II and mode III can be calculated in a similar fashion.

The extraction of the nodal displacements  $u$  for the computation of the crack opening displacement is straightforward in a finite element model. However, the extraction of the internal nodal forces  $f$  for the reaction forces poses a minor challenge in a finite element model, except at the boundaries. The internal forces are lost during the assembly process of the global stiffness matrix. They can however be recovered in different ways, which will be explained specifically for the case of Abaqus, but also holds in a more general way for most finite element solvers.

Abaqus solves the finite element model iteratively and thus assembles the stiffness matrix in each iteration. During the assembly, the right-hand side RHS for each element is computed as

$$\text{RHS} = -\text{MATMUL}(\text{AMATRX}, \text{U})$$

where AMATRX is the element stiffness matrix and U the displacement vector of the current iteration. Thus the right-hand side corresponds to the internal nodal forces  $f$  for the internal nodes. Hence, the internal forces could be extracted with a subroutine, called during the assembly of the global stiffness matrix. This method is relatively unconventional and associated with a large amount of bookkeeping.

An alternative approach, that is used for this thesis, is to modify the model slightly. Here the interface of the crack is modified. The seam of the crack is modelled with a length of  $a + 2\Delta a$  instead of a length of  $a + \Delta a$ , i.e. the crack extends until node  $i + 4$  in fig. 35. The excessive

length of the crack is however reduced again by constraining the nodes at  $i + 2$  and  $i + 3$  with multi-point constraints. This is illustrated in fig. 36, where the displacement degrees of freedom  $\mathbf{u}$  of the upper element and  $\mathbf{v}$  of the lower element are to be constrained, which is indicated in red. In Abaqus, this is achieved with the following six equations.

$$u_j^i - v_j^i = 0, i = (1, 2), j = (1, 2, 3) \quad (5.4)$$

This is however not quite sufficient for the extraction of the reaction force  $F$ . For this task, one additional step has to be undertaken as explained in [Sys20]. Here a reference node with degrees of freedom  $\mathbf{w}$  is introduced at each of the undeformed positions of the nodes involved in the multi-point constraints. The reference nodes are not directly part of the remaining mesh and will be only linked via an updated version of eq. (4.4).

$$u_j^i - v_j^i - w_j^i = 0, i = (1, 2), j = (1, 2, 3) \quad (5.5)$$

Furthermore, the degrees of freedom of the reference nodes  $\mathbf{w}$  are fully constrained, i.e.  $\mathbf{w} = \mathbf{0}$ . This leads to the possibility of extracting the reaction forces of the reference node, which are identical to the reaction forces at the interface of the crack.

Even though this approach was chosen for the model instead of the extraction during assembly, both have been implemented in a preliminary version for the sake of comparison and verification. The verification was successful and only the multi-point constraint approach will be used.

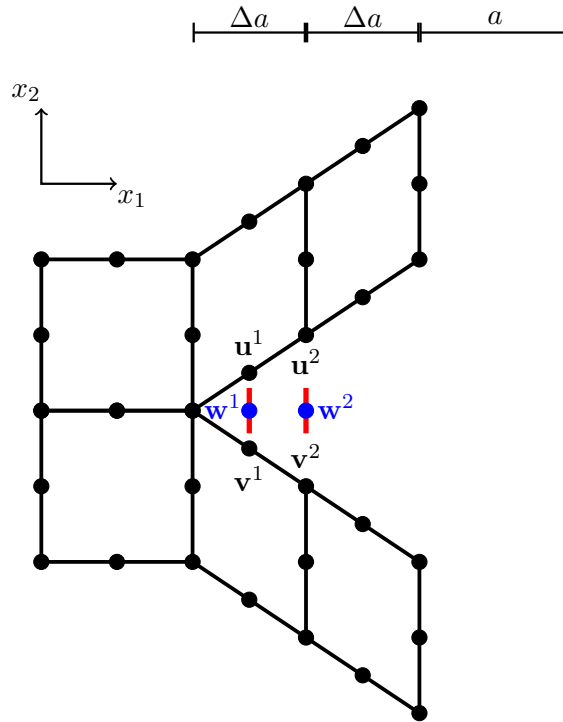


**Figure 36** Schematic of the reaction force extraction method via multi-point constraints. Here an excessive crack with length  $a + 2\Delta a$  is reduced to the desired length of  $a + \Delta a$  by constraining the nodes  $\mathbf{u}^i$ ,  $\mathbf{v}^i$  and  $\mathbf{w}^i$  together for  $i = (1, 2)$ . Simultaneously the displacements of the reference nodes  $\mathbf{w}^i$  are fully constrained. The reaction forces can then be extracted from the reference nodes.

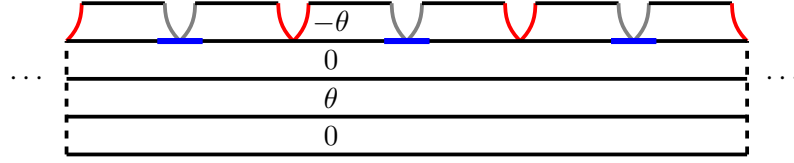


**Figure 37** Periodic tunnel cracking problem. The gray cracks are fully developed through the entire laminate, while the red cracks are still propagating. Additionally delamination can be inserted at the fully developed crack tips, which is marked in blue.

### 5.1.2. Tunneling Crack Propagation

As seen in fig. 3, the tunneling crack propagation occurs before the delamination. Thus it is expected, that the energy release rate of the delamination is lower than for the tunneling cracks until a tunneling crack saturation is reached, i.e. a threshold of the crack density  $\rho_c$ . Preliminary studies, that show this saturation effect have been conducted in [Mik+21]. These will now be extended with the periodic model to determine the threshold at which delamination can occur. The goal is to determine the energy release rate  $\mathcal{G}$  of tunneling cracks between fully tunneled cracks at a given crack density  $\rho_c$ . The problem is illustrated in fig. 37, where the gray cracks have already tunneled through the entire laminate and the red cracks are still propagating. Thus it is the energy release rate of the red cracks, that is to be determined.

Until now in this thesis, the far-field loading was force-based, whereas, in [Mik+21], the loading was displacement-based. For the stiffness degradation and the delamination propagation, the approaches are equivalent. However, when using the computational approach from [HS93], i.e. eq. (2.8), special care has to be taken. Typically in linear elastic fracture mechanics, an infinitesimal crack increase is considered, which leads to the force- and displacement-based approaches being equivalent with regard to the change in potential energy and thereby the energy release rate, as seen in [And17]. However, when considering eq. (2.8), the tunneling crack spans the height of at least one ply and propagates in the off-axis direction. This leads to a difference in the potential energy, as illustrated in fig. 38, where the load-control is shown in gray and the displacement control in red. This difference is explained in more detail in section A.1 with a simple toy-example. From this, it is observed, that the displacement-based approach lacks part of the potential energy. Therefore, the force-based approach is applied to all the following cases. For [Mik+21], this was not a problem, as the two approaches converge to each other for infinitely long specimens with a finite number of cracks, as explained in section A.1.

Furthermore, the toy-example in section A.1 indicates two possible computational approaches for the energy release rate, via the change in internal energy  $\Delta U$  or the change in the external work  $\Delta W$ . For this to be true, Clapeyron's theorem has to be assumed, which states that the potential energy is equal to half the external work under equilibrium  $\Pi = \frac{1}{2}W$ . This can be reformulated in terms of the changes in energy, as

$$\Delta U = -\frac{1}{2}\Delta W. \quad (5.6)$$

Note, that this assumption has not been proved and doesn't hold in general when considering

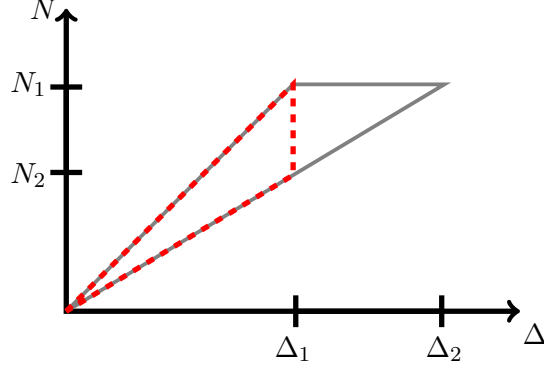


**Figure 38** Force-displacement curve showing the change in potential energy for load-control in gray and for displacement control in red.

fracture. However in the case of the studied laminate empirical studies have been conducted, that confirm the validity of the assumption. Thus two possibilities exist for the determination of the energy release rate. Until now tunneling cracks have been typically analyzed via the internal energy using eq. (2.8). Alternatively, the external energy may be used.

$$\mathcal{G} = -\frac{\Delta\Pi}{\Delta A} = -\frac{\Delta U + \Delta W}{\Delta A} = -\frac{\Delta W}{2\Delta A} \quad (5.7)$$

This can be reformulated using the displacement  $\Delta_1$  encountered at the right boundary in fig. 25, where the force  $N_1$  is applied. Thus the change in external work can be expressed by the state before  $\Delta_1^0$  and after  $\Delta_1^1$  crack propagation

$$\Delta W = (\Delta_1^0 - \Delta_1^1)N_1, \quad (5.8)$$

leading to the following expression for the energy release rate.

$$\mathcal{G} = -\frac{\Delta W}{2\Delta A} = \frac{(\Delta_1^2 - \Delta_1^1)N}{2h_c \sin(\theta)} \quad (5.9)$$

Alternatively, the expression can be formulated in terms of the compliance  $C_1 = \Delta_1/N_1$ .

$$\mathcal{G} = \frac{\Delta C_1 N_1^2}{2h_c \sin(\theta)} \quad (5.10)$$

This compliance-based approach has the advantage, that the stiffness degradation curves from chapter 4 can be used to determine the tunneling crack energy release rate without further computations. This however requires a slight transformation of the stiffness degradation curves

$$C_1 = \frac{1}{K_1} = \frac{1}{E_1 \frac{\hat{L}}{H}} = \frac{1}{E_1 \frac{\sin(\theta)}{\rho_c H}} = \frac{\rho_c H}{E_1 \sin(\theta)}, \quad (5.11)$$

which is illustrated in fig. 40 for the layup  $[0/\theta/0/-\theta_c]_s$  at  $\theta = 30^\circ$  from fig. 24.

Given the transformed curve from the left part of fig. 39, the energy release rate required to e.g. double the crack density can be determined by the difference in the compliance  $\Delta C$ . Thus differ-

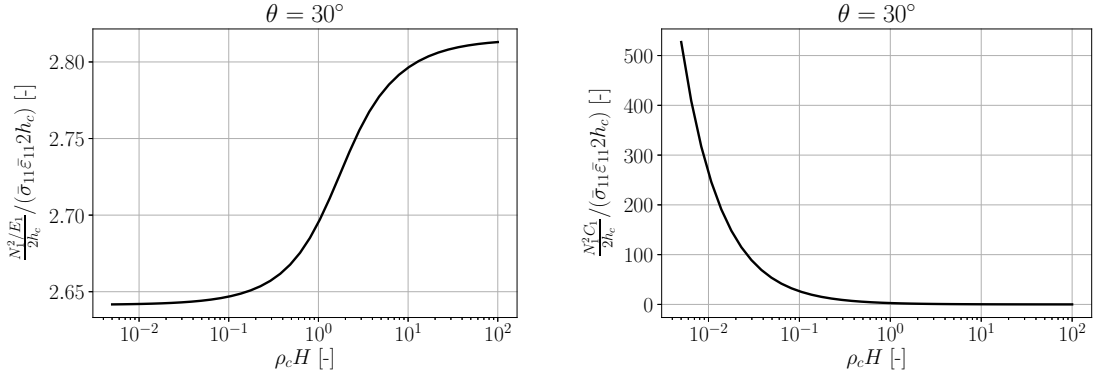


**Figure 39** Transformation of the stiffness  $E_1 = \sigma_{11}/\varepsilon_{11}$  to the compliance  $C_1 = \Delta_1/N_1$ . The curve is modified from fig. 24 and expressed in a sense, such that the energy release rate  $\mathcal{G}$  between two crack densities can directly be extracted via the difference.

entiating the curve with respect to the tunneling crack density leads to the curve in fig. 40 with the energy release rate. The computation is compared to results obtained via the internal energy approach from eq. (2.8) confirming that the approaches are equivalent. Thus the compliance method is a convenient alternative to the approach with eq. (2.8) if the stiffness degradation curve is given. The downsides of the approach are its limitation to cases under uni-axial load and the inability to extract the mode-mixity.

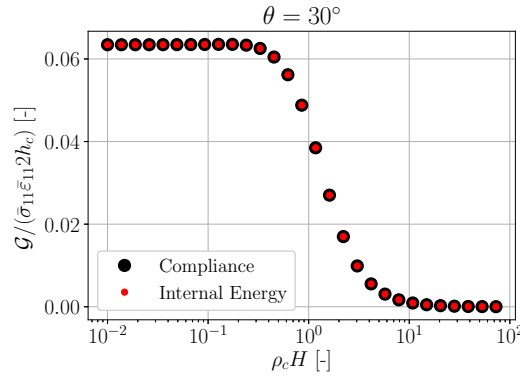


**Figure 40** Energy release rate for the doubling of the tunnel cracking density, given the current density  $\rho_c$  obtained with the compliance method via a modification of the stiffness degradation result from fig. 24.

Therefore the energy release rate  $\mathcal{G}$  will in this thesis mainly be computed via the internal energy, as explained in section 2.4. Here, it is assumed that the undamaged stress state  $\sigma^0$  and the crack opening displacement  $\Delta u$  in a single cross-section, reach a steady-state. Hence, the energy release rate is referred to as the steady-state energy release rate  $\mathcal{G}_{ss}$  and can be computed with eq. (2.8) for mode I and with eq. (2.9) for mixed-mode cracking. When this method was introduced by [HS93], it was for a single tunneling crack, which meant that the undamaged stress state  $\sigma^0$  could be computed analytically. With multiple cracks present, the undamaged stress state, i.e. the stress state with only the gray cracks from fig. 37 present, has to be estimated numerically. Thus two simulations have to be performed for the computation of the energy release rate.

For this task, two periodic models are created and illustrated in fig. 41. In both cases, a full period of the problem is modeled. The first is to determine the stress state  $\sigma^0$ , where the crack of interest is still closed. The second is for the crack opening displacement  $\Delta u$ , where the crack is open. These can then be inserted in eq. (2.9) for the energy release rate. The issue with this approach lies in the extraction of the stresses  $\sigma^0$ , which occurs via an extrapolation from the Gauß points to the nodes. This introduces interpolation errors and a superior approach when using the finite element method is to use the nodal quantities, i.e. the reaction forces  $F^0$ . The change in potential energy can be defined as

$$d\Pi = \frac{1}{2} \left( \sum_i F_{1i}^0 \Delta u_{1i} + \sum_i F_{2i}^0 \Delta u_{2i} + \sum_i F_{3i}^0 \Delta u_{3i} \right). \quad (5.12)$$

Due to the symmetry of the crack opening displacement,  $\Delta u_2$  is always zero and the corresponding term cancels out. Additionally, the crack opening displacements can be expressed in components orientated in the normal  $\Delta u_n$  and transverse  $\Delta u_t$  direction with respect to the crack

$$\Delta u_n = \Delta u_1 \sin(\theta) - \Delta u_3 \cos(\theta), \quad (5.13)$$

$$\Delta u_t = \Delta u_1 \cos(\theta) + \Delta u_3 \sin(\theta). \quad (5.14)$$

This is convenient, as it allows to split the potential energy into two terms, corresponding to the two fracture modes, i.e. mode I and mode II.

$$d\Pi = d\Pi_I + d\Pi_{II} = \frac{1}{2} \left( \sum_i F_{n_i}^0 \Delta u_{n_i} + \sum_i F_{t_i}^0 \Delta u_{t_i} \right). \quad (5.15)$$

The increase in fracture surface  $dA$  can be computed as

$$dA = \frac{h}{\sin(\theta)}, \quad (5.16)$$

where it is important to take the nature of the off-axis crack into account with the division by  $\sin(\theta)$ .

Inserting eq. (5.15) and eq. (5.16) into the definition of the energy release rate, eq. (2.1) yields

$$\mathcal{G}_{ss} = \mathcal{G}_I + \mathcal{G}_{II} = \frac{d\Pi_I + d\Pi_{II}}{dA} = -\frac{\sin(\theta)}{2h} \left( \sum_i \Delta u_{n_i} F_{n_i}^0 + \sum_i \Delta u_{t_i} F_{t_i}^0 \right). \quad (5.17)$$

Another interesting aspect observed in fig. 3 is that tunneling cracks and delamination cracks seem to occur sequentially, i.e. the tunneling effect isn't encountered again, as soon as delamination occurs. This could be explained by a decreasing energy release rate of the tunneling cracks, as soon as the delamination initiates. This can also be investigated by the model shown in fig. 41, where a delamination, indicated in blue, is introduced at the crack tip of the fully propagated tunneling cracks.



(a) Undamaged case to extract initial stress state  $\sigma^0$  or reaction forces  $F^0$ . (b) Damaged case with tunneling cracks to extract the crack opening displacement  $\Delta u$ .

**Figure 41** Two periodic tunnel cracking models with a full period each. The gray cracks are fully developed through the entire laminate, while the red cracks are still propagating. Additionally delamination can be inserted at the fully developed crack tips, which is marked in blue. The boundary conditions are identical to the ones presented in fig. 11. The reaction force  $F^0$  and the crack opening displacement  $\Delta u$  are inserted in eq. (5.17) to compute the energy release rate  $\mathcal{G}_{ss}$ . Again note, that the vertical anti-symmetry line can be exploited.

### 5.1.3. Crack Propagation and Fatigue

As discussed in section 2.3 the energy release rate  $\mathcal{G}$  can be related to the crack growth rate per cycle. This applies both for the tunneling crack growth rate, denoted as TCGR, and the delamination crack growth rate denoted as DCGR. Both can be expressed as power laws with respect to  $\mathcal{G}$ , that are determined empirically for a specific layup, as seen in [QC14] and [CMQ19]. Since this section will consider both the tunneling cracks and the delamination cracks, their energy release rates will be distinguished with the subindices  $tc$  and  $dc$ .

Given such a power law and several simplifications, the first two stages of the fatigue life, seen in fig. 2, can be described with the presented finite element model. For this, it is assumed, that the tunneling cracks develop in a perfectly periodic and sequential manner. Thus given a crack density  $\rho_c$  of fully developed tunnel cracks, the next tunneling cracks will initiate exactly halfway between the previous cracks and thus yield in a doubled crack density  $2\rho_c$  after their simultaneous propagation. This is illustrated in fig. 42, where the gray lines represent the existing tunneling cracks and the red lines the cracks, that are currently propagating.

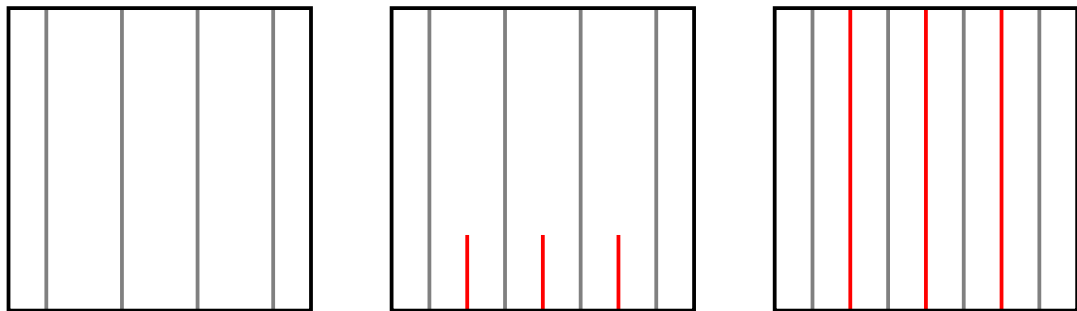


**Figure 42** Top view of the laminate showing the sequential cracking. The gray lines indicate fully developed cracks, whereas the red lines indicate cracks, that are still propagating. Thus from left to right, the manner in which the red cracks propagate is shown.

This assumption enables the usage of the periodic finite element model and allows to treat the tunneling cracks separately. For each tunneling crack density, an energy release rate can be computed, which then can be related to a crack growth rate. The crack growth rate can then be used to compute the number of cycles it takes for the cracks to tunnel through the entire laminate. This process can be repeated until delamination occurs.

The point of the beginning of delamination can be determined by comparing the energy release rate of the tunneling cracks  $\mathcal{G}_{tc}$  to the delamination  $\mathcal{G}_{dc}$ . Initially,  $\mathcal{G}_{tc}$  will be larger. However, at the saturation point of the tunneling cracks, delamination will initiate, which is when  $\mathcal{G}_{dc}$  will be larger.

These assumptions and computations of the axial stiffness at each stage, can be combined to a basic algorithm, see algorithm 1, to predict the stiffness degradation during the first two damage stages. Here, the crack density is doubled until the energy release rate of the delamination is larger than that of the tunneling cracks. Finally the delamination ratio  $d_r$  is incremented until it reaches 1. Simultaneously, the number of cycles  $n$  and the axial stiffness  $E_1$  are saved at each stage.

It has to be pointed out, that the power laws are typically expressed in a dimensional form, i.e. in mm per cycle. Thus the delamination ratio  $d_r$  has to be converted to a delamination length  $l_{d_r}$ , which is achieved with

$$l_{d_r} = \frac{d_r}{2\rho_c \sin(\theta)}, \quad (5.18)$$

where it is assumed, that the delamination length is measured from the tip of the tunnel crack to the tip of the delamination crack, i.e. half of the entire delamination crack, due to the symmetry.

---

**Algorithm 1** Fatigue estimation. Computation of the number of cycles until full delamination, while extracting the axial stiffness at each stage.

---

**Require:** initial tunnel crack density  $\rho_c^0 H$ , laminate width  $w$ , delamination incrementation  $\Delta d_r$   
 initialize arrays  $\mathbf{n}$ ,  $\mathbf{E}_1$   
 initialization  $d_r = 0$ ,  $\rho_c = \rho_c^0$

```

while True do
  compute  $\mathcal{G}_{tc}$ 
  compute  $\mathcal{G}_{dc}$ 
  if  $\mathcal{G}_{tc} \geq \mathcal{G}_{dc}$  then
     $\Delta a / \Delta n = \text{TCGR}(\mathcal{G}_{tc})$ 
     $n = n + \frac{w}{\Delta a / \Delta n}$ 
     $\rho_c = 2\rho_c$ 
  else
    break
  end if
  compute  $E_1$ 
   $\mathbf{n}.\text{append}(n)$ ,  $\mathbf{E}_1.\text{append}(E_1)$ 
end while

```

```

for  $i$  from 0 to  $\lfloor 1 / \Delta d_r \rfloor$  do
  compute  $\mathcal{G}_{dc}$ 
   $\Delta a / \Delta n = \text{DCGR}(\mathcal{G}_{dc})$ 
   $\Delta l_{d_r} = \frac{\Delta d_r}{2\rho_c \sin(\theta)}$ 
   $n = n + \frac{\Delta l_{d_r}}{\Delta a / \Delta n}$ 
   $d_r = d_r + \Delta d_r$ 
end for

```

---

Note, that this scheme is a simplification of the processes and yields only a rough estimate of the fatigue behavior. However, the intention of showing this simplified scheme is to illustrate the possibilities of the presented finite element model, as the model currently produces accurate results for the stiffness estimation and crack propagation. Due to its ease of use, the model is a good base model, that can be easily combined with more advanced approaches to improve fatigue predictions.

Specifically, the crack initiation and crack density evolution are typically treated with more sophisticated methods, as e.g. presented in [CMQ17]. Here, the local hydrostatic stress and the local maximum principal stress computed in fiber-matrix unit cells are used as crack initiation criteria to predict the crack density evolution. Fiber-matrix microstructures can be included in the current finite element model, as will be shown in chapter 6, without increasing the computational complexity significantly. Thus, the additional step, where the stresses in the unit cells are computed can be eliminated for an improved and cheaper crack density evolution.

Also, the assessment of the transition point from tunneling cracks to delamination cracks is not ideal, as the fracture toughness in the layer and at the interface might be different. Typically it will be lower at the interface, which means, that the delamination will occur earlier than the current model predicts. However, at the same time the fracture resistance under mode II, i.e. the dominant mode during delamination is much greater than for mode I, as explained in [SJ09]. Therefore, the point of transition is usually later than by this comparison. It can be accounted for by introducing an empirical factor in the comparison of the two energy release rates.

Additionally, it is possible, that a clear separation between tunnel cracking and delamination does not always occur. This could, however, also be taken into account in the model, by enabling the possibility of having tunnel cracking after the first delamination. Furthermore, the effect of the cracks on the stresses in the load-carrying layers is computable. Therefore, estimates for the final fiber breaking in stage III from fig. 2 could possibly also be made to give a full picture of the fatigue.

Other aspects, like plasticity, fiber-matrix microstructures and contact may also be added, to improve the results. There are however also several limitations of the model. For the stiffness estimation, it is always assumed, that the cracks have tunneled through the entire laminate. Thus it is not possible to produce intermediate results. Furthermore cracking can only occur in the same direction, i.e. in layers oriented in the same direction, as then the problem can no longer be described in two dimensions. However, if the cracks are separated by sufficiently thick layers, the principle of superposition may be used, as discussed in [CQ15].

## 5.2. Verification

Before the model can be applied to any cases, it has to be verified first. Besides small verification steps, as e.g. the computation of the internal forces via two different approaches to ensure

correctness, the verification will be achieved with a convergence study.

### 5.2.1. Convergence Study

The convergence study will be conducted with the layup  $[0/45_c/-45]_s$  from [MCQ18]. The reason for choosing this layup is, that it provided the greatest challenges during the convergence analyses performed in the context of this thesis. The results are illustrated in fig. 37 and fig. 43 for each of the delamination interfaces. The energy release rates for mode II and mode III converge and reach errors of less than 1% relatively fast. The mode I energy release rate however seems troublesome, as the errors are still relatively large for the greatest refinement level with over 200'000 elements.

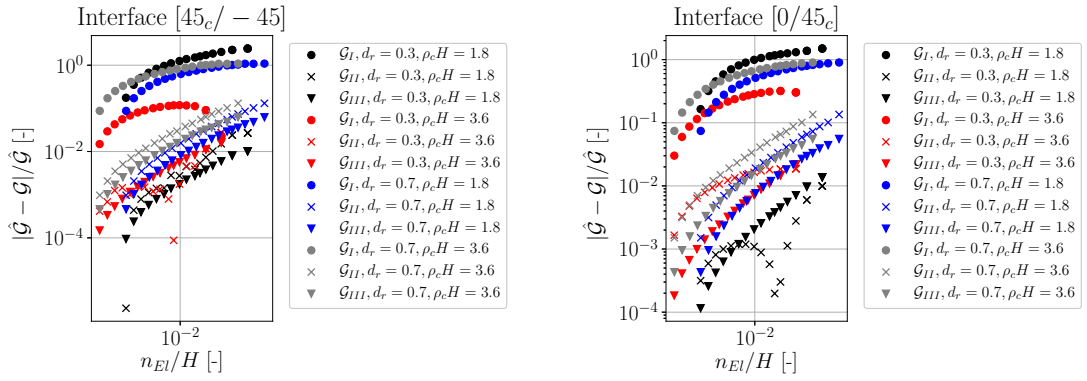


**Figure 43** Convergence analysis of the energy release rate with the layup  $[0/45_c/-45]_s$  from [MCQ18]. Left: Energy release rate for the interface  $[45_c/-45]$ . Right: Energy release rate for the interface  $[0/45_c]$

This is shown even more distinctly in fig. 44, where on the left side only the mode I energy release rate is shown and no convergence is observed at all. The explanation for this diverging behavior is the oscillating stress field at the tip of the crack in bi-material interfaces, as explained in [Kru04]. Here it is explained, that the mode-mixity is not defined for a crack increment  $\Delta a$  going towards 0. Simultaneously  $\Delta a$ , which also defines the degree of mesh refinement, has to be chosen sufficiently small, so that it is ensured, that the finite element solution has converged. This poses a challenge for the convergence, as seen in the left part of fig. 44. To confirm, that this in fact is the reason for the lack of convergence, the study was repeated for the layup  $[-45/-45_c/-45]_s$  while keeping all other parameters identical, i.e. the bi-material interface is removed. The right figure in fig. 44 shows the result and with a clear convergence behavior. From this convergence study, an appropriate degree of refinement can be estimated. Thus  $n_{EI}/H = 0.01$  is chosen for all upcoming studies, which corresponds to the recommended range of 0.1 – 0.01 by [Kru04].

Additionally, [Kru04] states, that this phenomenon only occurs for mode I fracture. Thus this is in agreement with the findings from fig. 43, where the mode II and mode III energy release rates converge appropriately. As the mode II and mode III energy release rate convergence properties are sufficient and the mode I energy release rate is not of interest and in many cases unphysical, the verification is deemed successful. An explanation for disregarding the mode I energy release rate will follow in section 5.3.

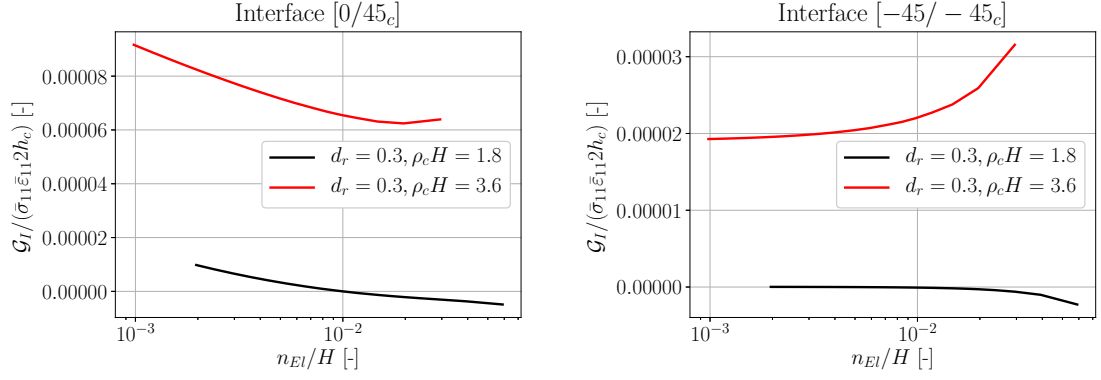


**Figure 44** Convergence analysis of the mode I energy release rate  $G_I$  in the layups  $[0/45_c/-45]_s$  on the left and  $[-45/-45_c/-45]_s$  on the right, illustrating the convergence issues in a bi-material interface.

### 5.3. Validation

The validation will again be carried out with results found from literature. It is however more challenging, as the amount of data is sparse for this problem, as it until now only has been obtained by expensive 3D models or generalized plane strain models limiting itself to cracks orientated at  $90^\circ$ . Experimental data is basically non-existent, as it is extremely challenging to extract energy release rates from delamination cracks.

Two validation cases have been chosen, where [MCQ18] was already used for the validation of the stiffness degradation and thus listed in table 2. The two cases are now listed in table 3, where both are based on the same periodic 3D model described in [MCQ18].

**Table 3** Validation cases for the delamination crack propagation.

Validation Case	[CMQ19]	[MCQ18]
layup	$[90_{4_c}/0_2]_s$	$[0/45_c/-45]_s$
$E_L$ [GPa]	48.83	48.83
$E_T = E_{T'}$ [GPa]	14.07	14.07
$G_{LT} = G_{LT'}$ [GPa]	5.200	5.200
$G_{TT'}$ [GPa]	5.025	5.025
$\nu_{LT} = \nu_{LT'}$ [-]	0.3080	0.3080
$\nu_{TT'}$ [-]	0.4000	0.4000
ply thickness [mm]	0.3100	0.6000

First the case from [CMQ19] with the layup  $[0_2/90_{4_c}]_s$  is used. Here the crack is oriented at  $90^\circ$  and the 2D model is equivalent to a generalized plane strain model. The comparison of the two models is shown in fig. 45, where a good agreement is reached for the greater crack densities. However for the tunnel crack density  $\rho_c H = 0.6$  a large deviation occurs, for which no reason has been found. It was ensured, that the results are converged and no underlying differences between

the models of different crack densities were observed.

Furthermore, it is noted, that only the mode II energy release rate  $\mathcal{G}_{II}$  is shown. This is because the mode I energy release rate  $\mathcal{G}_I$  is two orders of magnitude smaller and in fact unphysical. This is because the interface does not open, but overlaps, as was shown for isotropic layers in fig. 26. Thus a mode I energy release rate does not represent the crack propagation properties appropriately, as the crack will not grow in mode I. Therefore the mode I energy release rate should be set to 0 if an overlap occurs, which simultaneously circumvents the convergence issues connected with mode I. The mode III energy release rate is 0, due to the orientation of  $90^\circ$ , which prevents any non-uniform out-of-plane displacements and thus no mode III crack growth.

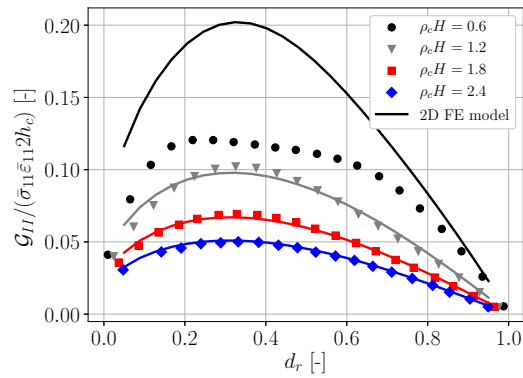


**Figure 45** Comparison of mode II energy release rate  $\mathcal{G}_{II}$  between the 3D periodic FE model from [CMQ19] and the 2D model for a laminate with layup  $[0_2/90_4]_s$ .

The second validation case from [MCQ18] considers the layup  $[0/45_c/-45]_s$  and the results are shown in fig. 46 for each of the energy release rates. Additionally note, that there are two delamination interfaces, as the crack is not located at the symmetry boundary. A good agreement is reached for mode II and mode III. The comparison for mode I is however not perfect. However, as discussed in section 5.2.1, the convergence properties are questionable and the results can not be trusted reliably. It is even surprising, that an agreement is found for all mode I energy release rates except for the tunnel cracking density  $\rho_c H = 0.45$ . But, as with the case from [CMQ19], the mode I energy release rate is two orders of magnitude smaller, than the total energy release rate and unphysical, due to the overlap also occurring for this layup except for very small delamination ratios  $d_r < 0.1$ . Thus the mode I energy release rate is in fact 0 and can be neglected.

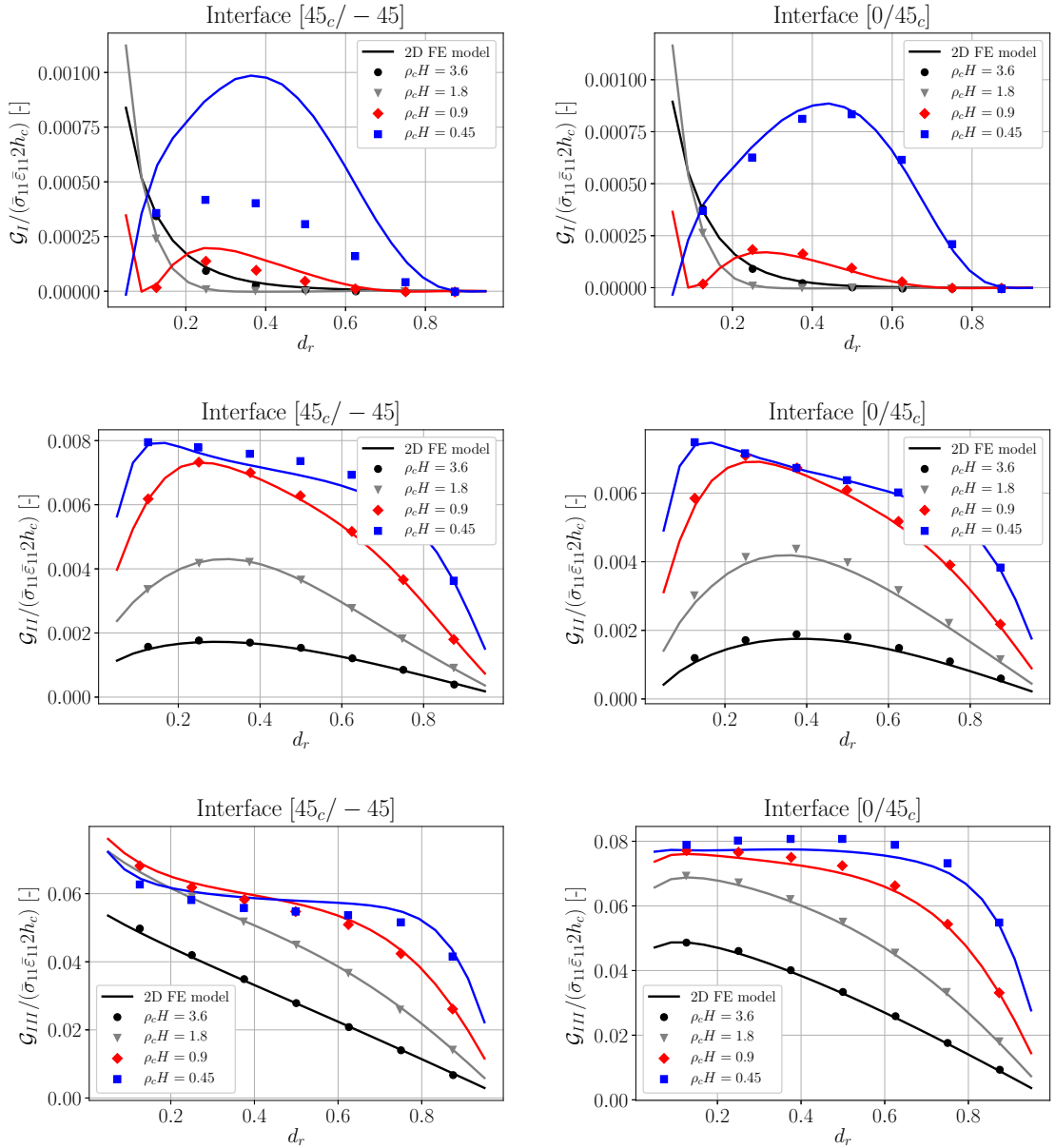


**Figure 46** Comparison of the energy release rates  $\mathcal{G}$  between the 3D periodic FE model from [MCQ18] and the 2D model for a laminate with layup  $[0/45_c / -45]_s$ . Left: Energy release rate for the interface  $[45_c / -45]$ . Right: Energy release rate for the interface  $[0/45_c]$ .

Hereby, the model is considered validated. Typically only the mode II and mode III energy release rates have to be considered, which resolves the difficulties with the mode I fracture. Before this can be done for a different layup, it still has to be checked, that the mode I energy release rate is significantly smaller than the total energy release rate or that there is an overlap present. The only unsuccessful part of the validation was seen in fig. 45 for a small tunnel cracking density. Although it is slightly suspicious, it is not considered concerning, as all other validation cases were successful. Also note, that the overlap could be considered by introducing contact to the model. Preliminary analyses by [CMQ19] however showed that the influence is negligible.

## 5.4. Results

The verified and validated model can now be applied to the layup  $[-\theta_c/0/\theta/0]_s$  using the materials GlassFRP and CarbonFRP from table 1. Several parametric studies will be conducted and compared to the results from [Mik+21] to compare the delamination propagation to the tunnel cracking propagation. Finally, all aspects of the model are combined to predict the fatigue life of an example laminate using algorithm 1.

First, the general delamination behavior is investigated. For this parametric studies with an orientation of  $\theta = 45^\circ$ , a varying delamination ratio  $d_r$ , and different crack densities  $\rho_c$  are conducted. The results are shown in fig. 47. It is seen, that the mode II and mode III components of the energy release rate are significantly larger. Additionally, it was observed, that no crack opening occurred in mode I, wherefore the mode I energy release rate  $\mathcal{G}_I$  should be neglected and set to 0. Mode II is the dominant fracture mode, where an unstable crack growth occurs until about  $d_r = 0.2$ , whereupon the energy release rate decreases, i.e. the growth slows down, due to a saturation effect. The effect is described as a shielding effect by [CMQ19], as the delamination from the neighboring cracks interferes and decreases the delamination ratio evolution.

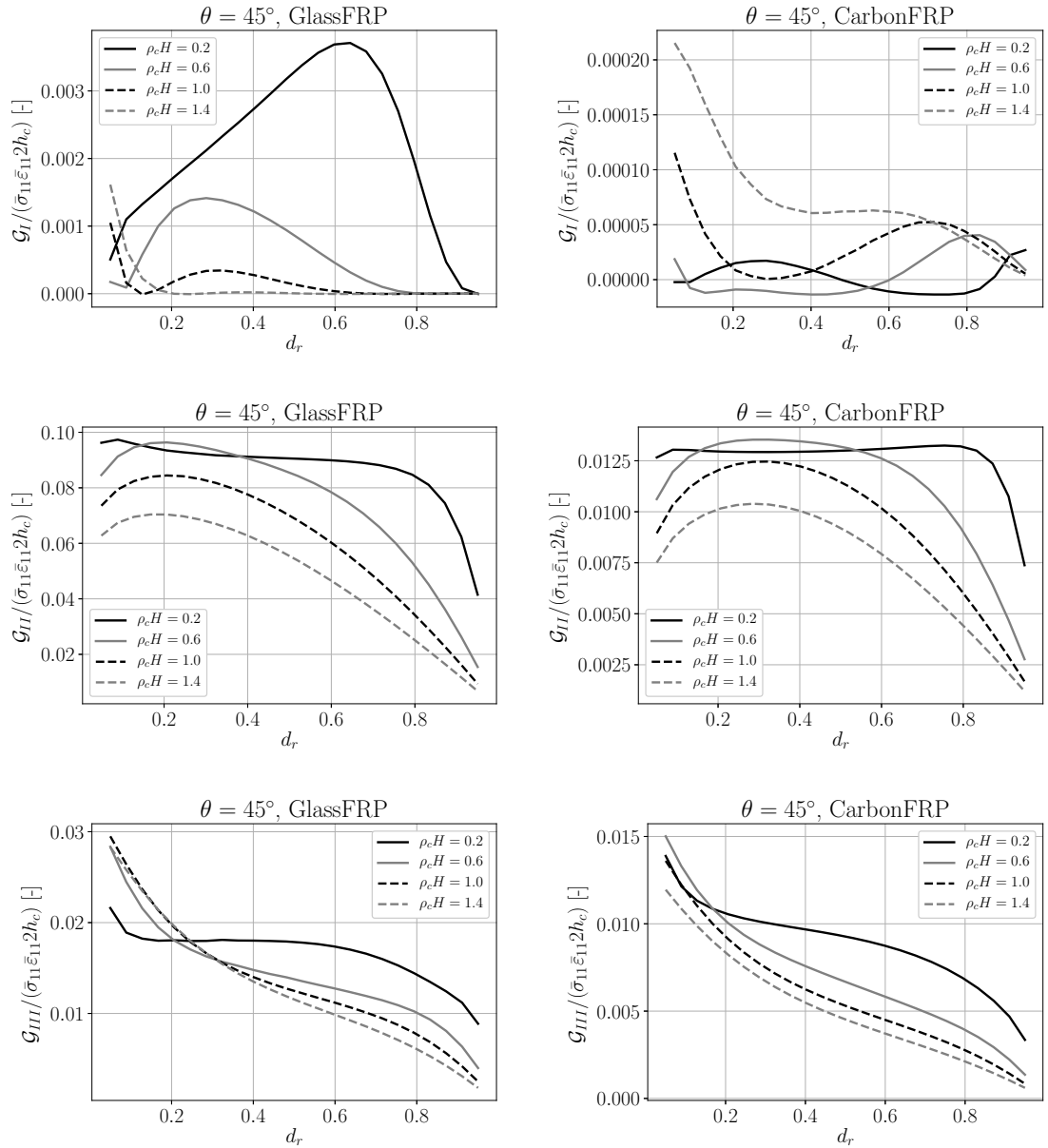


**Figure 47** Influence of the delamination ratio  $d_r$  on the delamination energy release rate using the layup  $[-\theta_c/0/\theta/0]_s$  for  $\theta = 45^\circ$ . From top to bottom, the energy release rates  $\mathcal{G}_I$ ,  $\mathcal{G}_{II}$  and  $\mathcal{G}_{III}$  are shown. Left: GlassFRP. Right: CarbonFRP.

Next the influence of the orientation  $\theta$  is studied with a parametric study shown in fig. 48. At the top, the total energy release rate  $\mathcal{G}$  is shown, whereas in the bottom the mode II and mode III contributions are shown. The mode II energy release rate converges to 0 for  $\theta = 0^\circ$ , as the delamination is then oriented perpendicular to the load and can therefore not grow in mode II. Similarly, the mode III energy release rate is 0 for both  $\theta = 0^\circ$  and  $\theta = 90^\circ$ , as no out-of-plane shear can occur and thus prevents growth in mode III. Therefore delamination does almost not happen at very small angles, which is however rare, as the off-axis layers are typically oriented in an angle different to  $\theta = 0^\circ$ .

An interesting comparison is the one to the tunneling crack growth, which can be made using

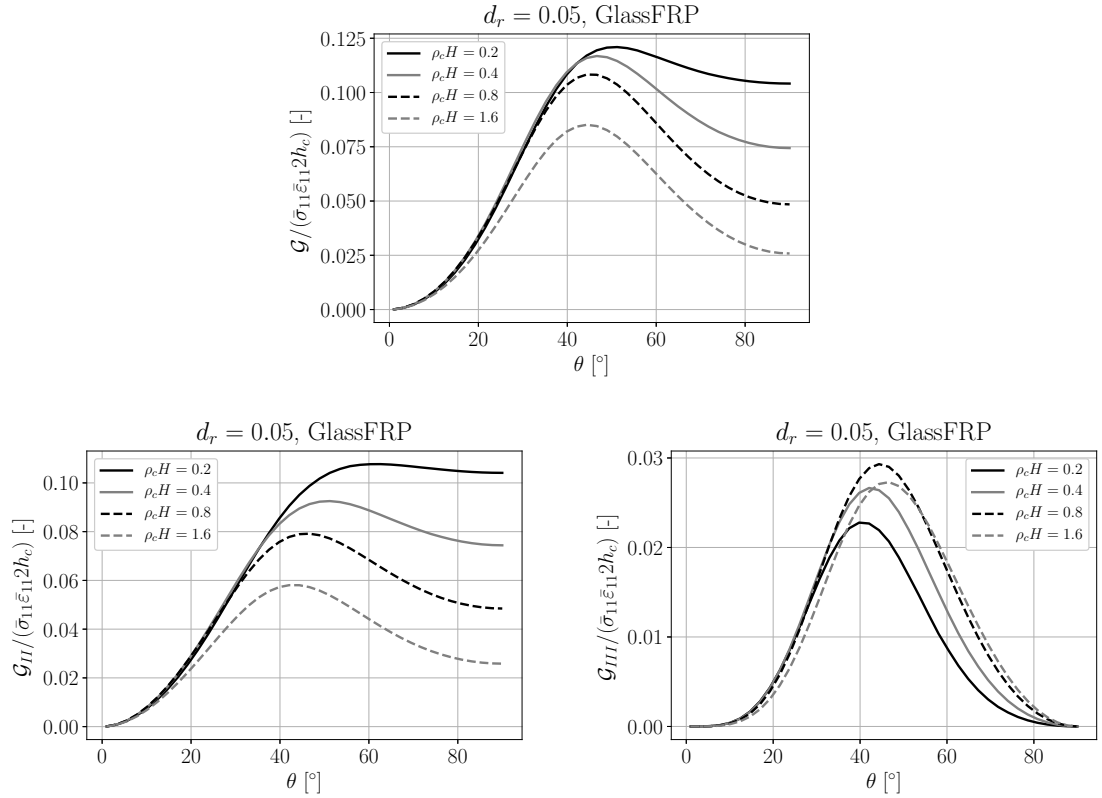


**Figure 48** Influence of the orientation  $\theta$  on the delamination energy release rate using the layup  $[-\theta_c/0/\theta/0]_s$  for GlassFRP. Top: mode II and mode III,  $\mathcal{G}$ . Left: mode II,  $\mathcal{G}_{II}$ . Right: mode III,  $\mathcal{G}_{III}$ .

the results from [Mik+20] and [Mik+21]. The simulations from [Mik+21] are rerun with slight modifications. First, the energy release rate is computed with the reaction forces, as shown in eq. (5.17) instead of the stresses. Secondly, the model to study the influence of the neighboring cracks is modified slightly. Here the periodic model, shown in fig. 41 is used, whereas [Mik+21] modelled three isolated cracks to study their interaction. The results are however very similar and presented in fig. 49, where the gray dots indicate the results obtained in [Mik+21] at  $\theta = 45^\circ$ . The deviations are small, but not unexpected, due to the differences in the models. Not only is the periodic model more useful in this case, but also computationally more efficient, as only one period has to be modelled.

The reason, why the comparison to the tunneling crack propagation is interesting, is, that it gives an idea of when which crack growth occurs. As seen in the left part of fig. 49 the tunneling crack energy release rate is much larger than that of the delamination cracks, seen in fig. 48. However, with an increasing crack density  $\rho_c$  the tunneling crack energy release rate decreases, allowing the delamination to take over.

This can be quantified by looking at specific orientations  $\theta$  and crack densities  $\rho_c$ , shown in fig. 50. On the left side, the energy release rate for the tunneling cracks is shown and on the right side for the delamination is shown. For an orientation of  $\theta = 60^\circ$  and a crack density of  $\rho_c H = 2$ , the

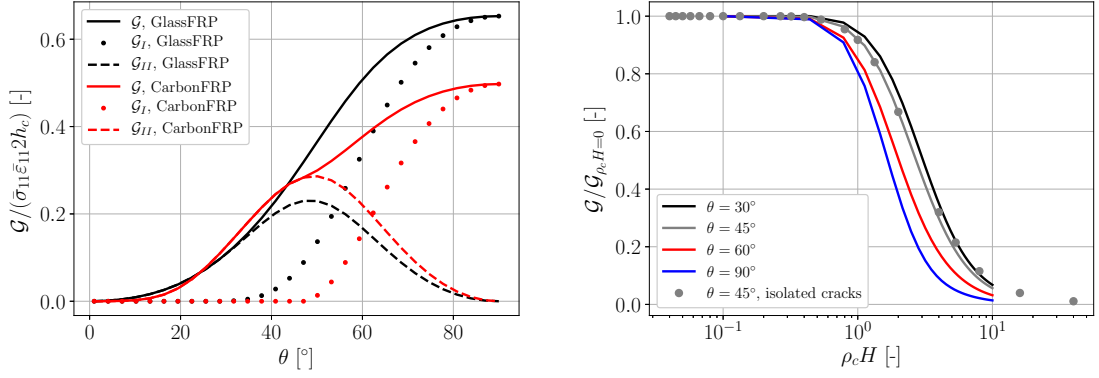


**Figure 49** Influence of the orientation  $\theta$  and the tunneling crack density  $\rho_c$  on the tunnel cracking energy release rate using the layup  $[-\theta_c/0/\theta/0]_s$  modified from [Mik+21]. Left: The influence of the orientation  $\theta$  for a single isolated tunneling crack. Right: The influence of the tunneling crack density  $\rho_c$  for the tunneling crack growth.

energy release rate is greater for the tunneling cracks at a low delamination ratio  $d_r$ , wherefore the tunneling cracks will dominate. However, for a density of  $\rho_c H = 4$ , the energy release rate of the delamination cracks is always greater. Thus at this density, only delamination will occur. Important to note is also, that this is the case along the entire spectrum of the delamination ratio  $d_r$ . If this were not the case, a mixture of tunnel cracking and delamination would occur. This result supports the model from fig. 2, where the two damage mechanisms can be separated, due to their sequential nature. Note, however, that this is typically a lower estimate of the transition point from tunnel cracking to delamination, as delamination, because mode II crack propagation typically encounters a higher fracture resistance.

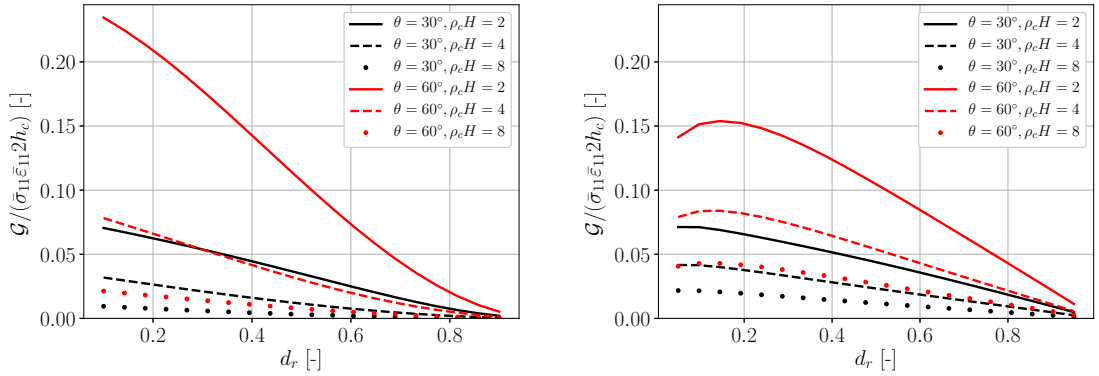


**Figure 50** Influence of the delamination ratio  $d_r$  on the energy release rate  $\mathcal{G}$  using the layup  $[-\theta_c/0/\theta/0]_s$ . Left: Tunnel cracking. Right: Delamination.

Furthermore, the influence of the layer thickness of the off-axis layers  $h_\theta$  is investigated with the results presented in fig. 51. As to be expected, the tunneling crack energy release rate decreases for an increasing off-axis layer thickness. Hence, if tunneling cracks or even delamination are problematic in a laminate, a simple solution might be increasing the off-axis layer thickness.

Finally, everything is combined to simulate the fatigue behavior of a laminate according to algorithm 1. To illustrate this a laminate with the layup  $[0/45/0/-45_c]_s$  is selected. Furthermore,

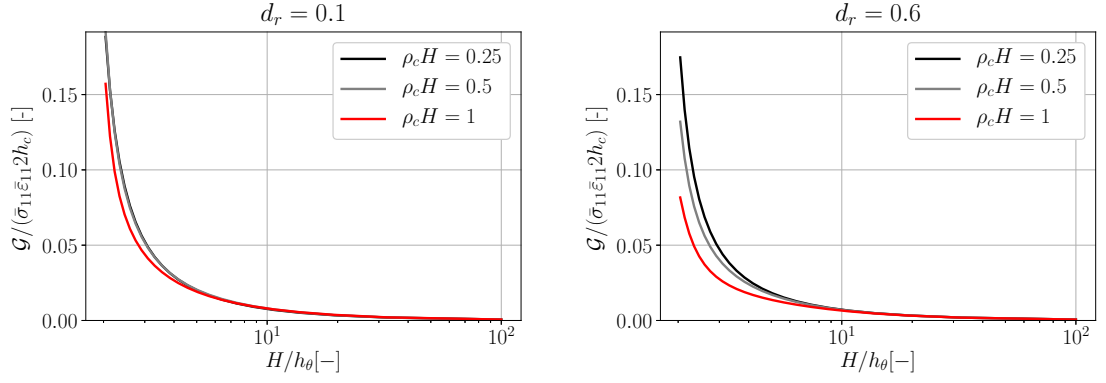


**Figure 51** Influence of the off-axis layer height  $h_\theta$  on the tunneling crack energy release rate using the layup  $[-\theta_c/0/\theta/0]_s$  with  $\theta = 45^\circ$  and GlassFRP.

a power law, that describes the tunneling crack propagation is required. Here the experimentally determined values from [QC14] obtained with the layup  $[0/50/0/-50_2]_s$  are used.

$$\text{TCGR}(\mathcal{G}) = 0.671\mathcal{G}^{4.41} \quad (5.19)$$

For the delamination propagation the following parameters are selected.

$$\text{DCGR}(\mathcal{G}) = 2 \cdot 10^{-6}\mathcal{G}^2 \quad (5.20)$$

Note, that the choice of the parameters of the power laws is relatively arbitrary, but is made to exemplify the usage of algorithm 1. If it were to be used properly, the power law has to be based on experiments of the chosen laminate layup, such as shown in [QC14] and [CMQ19]. Thus, the resulting fatigue behavior is not realistic and only serves as an example.

The chosen dimensions for the laminate are  $h = 0.35$  mm for the ply thickness and  $w = 350$  mm for the width of the laminate. An important ingredient for algorithm 1 is the initial crack density  $\rho_c^0$ . Due to the idealization of the crack density doubling during each iteration, illustrated in fig. 42, the final crack density  $\rho_c^N$  is related to the initial crack density  $\rho_c^0$  via a factor  $2^N$ , i.e.  $\rho_c^0 = \rho_c^N / 2^N$ . Hence, the initial crack density has to be estimated from the final crack density. Ideally, the final crack density could be based on experiments. An alternative is the determination via a comparison of the two energy release rates, which has been done for this layup in fig. 52. As mentioned previously, a factor should be applied to one of the energy release rates to take the difference in fracture resistance into account. To keep the example simple, this is neglected and the transition point is determined at about  $\rho_c H = 0.9$ .

The estimated transition point is then divided with  $2^5$  to provide the initial crack density  $\rho_c H = 0.9/2^5$ . Again the choice is arbitrary but could be improved by an experiment to assess the initial damage. Decreasing the initial density stretches the lifetime governed during tunnel cracking.

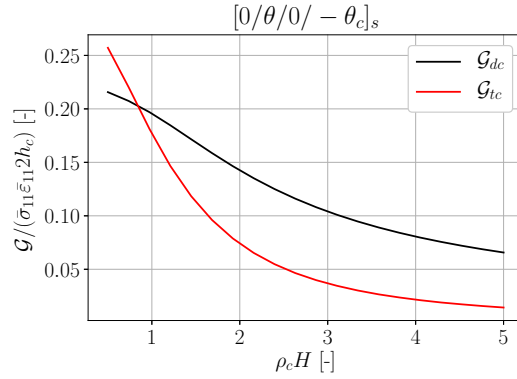


**Figure 52** Determination of the point of delamination for the layup  $[0/45/0/ - 45_c]_s$  and GlassFRP.

The result from the given example is provided in fig. 53. Here, the decrease in axial stiffness is shown against the number of cycles. The transition point from tunneling crack propagation to delamination is indicated with the red dashed line. Overall the graph is relatively rough, which in the first half is due to the doubling in crack density. A possible improvement could be by using an approach, that defines an average crack density evolution in a continuous manner, which would improve the resolution. The resolution of the second half, where delamination occurs can be improved by choosing a smaller delamination ratio step size  $\Delta d_r$ . Furthermore, the transition point seems to occur too early when compared to the tendencies shown in fig. 2, which is due to the missing factor between the energy release rates taking the difference in fracture resistances into account.

Also, the choice of the power law coefficients is essential. It will not influence the stiffness values, but their position with respect to the cycles, i.e. they are responsible for stretching the graph and determining an accurate lifetime, i.e. in this case the point of full delamination.

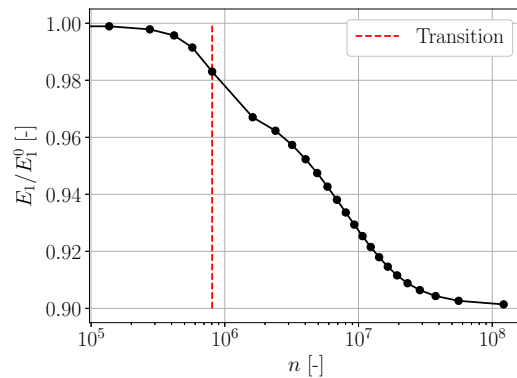


**Figure 53** Stiffness degradation with respect to the number of cycles.

However, as stated before, this is simply a model example showcasing the capabilities of the entire framework in the context of fatigue. Ideally, experiments should be conducted to determine

the power laws for both the tunneling cracks and the delamination ratio for a specific layup. Additionally, the initial and saturated crack density should be measured. Furthermore, initially it would be ideal if a layup was chosen with cracks in only a single layer or at least layers separated by thick load-carrying layers. Such a case would be great to validate and determine the accuracy of the approach.

## 6. Influence of the Fiber-Matrix Microstructure

Until this point, the materials in the plies have been assumed to be invariant throughout each ply. However, in reality, fiber-reinforced composites have strongly varying properties, due to the underlying fiber-matrix microstructure. This is typically, as also seen in the previous chapters, treated via a homogenization approach, which estimates a macro-scale material property, that can replace the microstructure. This concept is used widely and successfully for stiffness estimations, as e.g. explained in [ZB09]. The question is, however, if this concept also works well for the crack propagation or if it in fact should be modeled explicitly. Initial findings for tunneling cracks were presented in [Her+21b] and for delamination in [CMQ19]. The answer to this question is not easy and requires several investigations with a variety of fiber-matrix microstructures, which would expand the scope of this thesis too much. For this reason, the model to be used for these investigations is presented. It includes both regular and irregular fiber-matrix microstructures and the possibility to work with straight and non-straight cracks. Only basic investigations are presented to showcase the possibilities of the framework.

### 6.1. Model Description

It has been shown in [Her+21b], that modeling the fiber-matrix microstructure is only necessary in the vicinity of the crack. However, as cracks are present throughout the entirety of the laminate, the microstructure will be added throughout the entire length of the laminate without adding a lot of computational cost, due to the periodic nature of the problem. But, the microstructure will only be added in the layers with cracks, as illustrated in fig. 54. This is as the microstructure can not be represented by the two-dimensional model for the load-carrying layers, that are oriented at  $\theta = 0^\circ$ . The issue at this orientation is that the fibers are then parallel to the plane of the two-dimensional model. Although a longitudinal cut of the fibers could be modeled as rectangles in these layers, it would be an arbitrary cut, as these cuts are not invariant when moving along the out-of-plane axis.

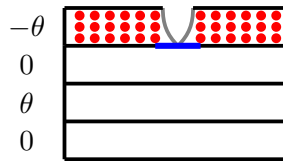


**Figure 54** Fiber-matrix microstructure model. The microstructure is only added in the plies with cracks.

The model is built up, such that an arbitrary fiber alignment may be added in the desired plies. In this thesis, two structures are presented. The first being a regular microstructure with a rectangular pattern. The second is an irregular microstructure extracted from a CT-scan from [MMA21]. Both have already been presented and can be seen in fig. 56. The reasoning behind the choice of the rectangular pattern is, that it allows for straight cracks, while e.g. a hexagonal pattern would require non-straight cracks, as cracking typically only occurs in the matrix material or at the

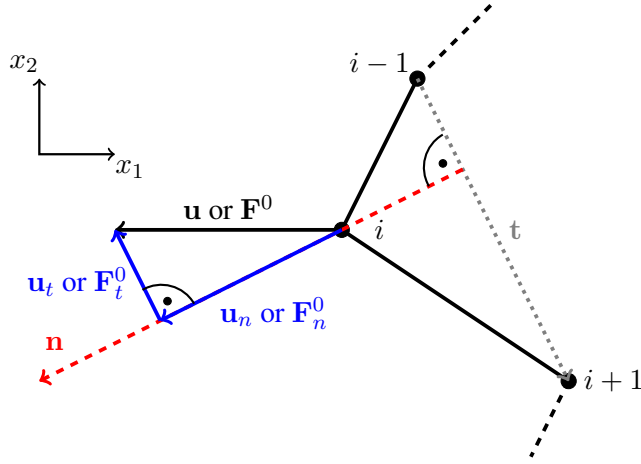


**Figure 55** Projection of nodal quantities, i.e. displacements  $\mathbf{u}$  and forces  $\mathbf{F}^0$  onto the normal direction  $\mathbf{n}$  of the crack surface.

fiber-matrix interface.

As previously stated, these studies have already been conducted for tunneling cracks in [Her+21b]. One key ingredient is however still missing, which is the computation of the energy release rate for non-straight cracks. For this task eq. (5.17) is recalled, where the energy release rate  $\mathcal{G}$  is computed with the crack opening displacements  $\Delta u$  and the reaction forces  $\mathbf{F}^0$  from the closed state. When considering the non-straight crack a challenge arises, when the fracture modes are to be distinguished, due to the variation of the normal direction of the fracture surface. Hence, each nodal quantity, i.e. the displacement and the force have to be projected via the individual crack surface normal. However, even the determination of the crack surface normal at each node poses difficulties, as the field between the elements, i.e. at the corner nodes, is only  $C^0$  continuous, which means that a normal vector is not defined in a mathematical sense. Instead, an approximation rule using the neighboring nodes will be employed, as is shown in fig. 55. Considering node  $i$ , the line between its neighbours  $i - 1$  and  $i + 1$  is defined as the transverse direction  $\mathbf{t}$ .

$$\mathbf{t}_i = \mathbf{x}_{i+1} - \mathbf{x}_{i-1} \quad (6.1)$$

Together with the off-axis direction, aligned with the tunneling cracks,  $\mathbf{r} = (\cos(\theta), 0, \sin(\theta))^T$ , the normal vector  $\mathbf{n}$  can be computed with the cross product.

$$\mathbf{n}_i = \mathbf{r} \times \mathbf{t}_i \quad (6.2)$$

Finally, the individual normal vectors  $\mathbf{n}$  and transverse vectors  $\mathbf{t}$  are used to project the global displacements  $\mathbf{u}$  and forces  $\mathbf{F}^0$  to the crack surface, yielding  $\mathbf{u}_n, \mathbf{u}_t, \mathbf{u}_r$  and  $\mathbf{F}_n^0, \mathbf{F}_t^0, \mathbf{F}_r^0$ .

$$\mathbf{u}_n = \frac{\mathbf{u} \cdot \mathbf{n}}{\mathbf{n} \cdot \mathbf{n}} \mathbf{n} \quad \mathbf{F}_n^0 = \frac{\mathbf{F}^0 \cdot \mathbf{n}}{\mathbf{n} \cdot \mathbf{n}} \mathbf{n} \quad (6.3)$$

$$\mathbf{u}_t = \frac{\mathbf{u} \cdot \mathbf{t}}{\mathbf{t} \cdot \mathbf{t}} \mathbf{t} \quad \mathbf{F}_t^0 = \frac{\mathbf{F}^0 \cdot \mathbf{t}}{\mathbf{t} \cdot \mathbf{t}} \mathbf{t} \quad (6.4)$$

$$\mathbf{u}_r = \frac{\mathbf{u} \cdot \mathbf{r}}{\mathbf{r} \cdot \mathbf{r}} \mathbf{r} \quad \mathbf{F}_r^0 = \frac{\mathbf{F}^0 \cdot \mathbf{r}}{\mathbf{r} \cdot \mathbf{r}} \mathbf{r} \quad (6.5)$$

In the same way, it can be applied to the crack opening displacements  $\Delta \mathbf{u}_n$ ,  $\Delta \mathbf{u}_t$ ,  $\Delta \mathbf{u}_r$ , which then can be used to compute the steady-state energy release rate  $\mathcal{G}_{ss}$  with a slightly modified version of eq. (5.17) to accommodate the additional mode III and the non-straight character of the crack,

$$\mathcal{G}_I = \frac{d\Pi_I}{dA} = -\frac{\sin(\theta)}{2l_c} \left( \sum_i \|\mathbf{u}_n\|_2 \|\mathbf{F}_n^0\|_2 \right) \quad (6.6)$$

$$\mathcal{G}_{II} = \frac{d\Pi_{II}}{dA} = -\frac{\sin(\theta)}{2l_c} \left( \sum_i \|\mathbf{u}_r\|_2 \|\mathbf{F}_r^0\|_2 \right) \quad (6.7)$$

$$\mathcal{G}_{III} = \frac{d\Pi_{III}}{dA} = -\frac{\sin(\theta)}{2l_c} \left( \sum_i \|\mathbf{u}_t\|_2 \|\mathbf{F}_t^0\|_2 \right) \quad (6.8)$$

$$\mathcal{G}_{ss} = \mathcal{G}_I + \mathcal{G}_{II} + \mathcal{G}_{III} \quad (6.9)$$

where  $l_c$  is the total crack length. Note, that this approach introduces numerical errors and that summing the individual energies  $d\Pi_I$ ,  $d\Pi_{II}$ , and  $d\Pi_{III}$  will not yield exactly the same as if the total energy was computed directly, i.e. without the projection step.

Instead of taking the microscopic crack surface directions into account, the macroscopic crack surface directions could be taken, i.e. if considering the crack from fig. 56 the macroscopic crack could be approximated by a vertical line for the projections. Thus the local projections are avoided and only the projection along the off-axis direction remains. The main argument for this approach is that when computing the energy release rate with the energy-based approach from [HS93], i.e. replacing the crack front with the stress state in front and the displacement state in the wake of the crack, the exact crack tip shape is already neglected. This is a reasonable approximation, as explained in [HS93], but also means, that the mode II and mode III contributions, due to the 3D crack tip, can not be determined accurately, as the crack tip is not considered. In other words, only the 2D wake of the crack is considered. However, as long as the fracture resistance with respect to mode II and mode III are similar, the distinction does not have to be made, which is why the proposed projection method most likely only introduces additional overhead without a significant benefit and purpose.

## 6.2. Verification

The verification step is kept short for the inclusion of the fiber-matrix microstructure, as it was already presented in previous work [Her+21b]. Convergence studies were successfully conducted and the most important observation was, that the different materials must be consistent with each other, i.e. the homogenized material and the inhomogeneous microstructure. Thus the choice of the homogenization approach is essential. The rule of mixtures did not yield satisfactory results and the Halpin-Tsai rule was a better analytical tool. The best results were obtained with a finite element-based homogenization using an Abaqus micro mechanics plugin [McL17]. For the following simulations, the Halpin-Tsai rule is used, as it yields the greatest flexibility with respect to different microstructures without the need for an additional computation. The Halpin-Tsai rule, mentioned in [ZB09], with an additional empirical estimate of  $\nu_{TT'} = 0.41$  is given as

$$\begin{aligned}
 E_L &= E_f \varphi + E_m (1 - \varphi) & G_{LT} &= G_m \frac{1 + \zeta \eta_G \varphi}{1 - \eta \varphi} & \nu_{LT} &= \nu_m (1 - \varphi) + \nu_f \varphi \\
 E_T &= E_m \frac{1 + \zeta \eta_E \varphi}{1 - \eta \varphi} & G_{LT'} &= G_{LT} & \nu_{LT'} &= \nu_{LT} \\
 E_{T'} &= E_T & G_{TT'} &= \frac{E_T}{2(1 + \nu_{TT'})} & \nu_{TT'} &= 0.41
 \end{aligned}$$

where

$$\eta_E = \frac{\frac{E_f}{E_m} - 1}{\frac{E_f}{E_m} + \zeta} \quad \eta_G = \frac{\frac{G_f}{G_m} - 1}{\frac{G_f}{G_m} + \zeta},$$

and  $\zeta = 2$  for circular fibers.

## 6.3. Results

Both fiber-matrix microstructures and the non-straight cracks can be applied to a great variety of problems and investigations, which however lies outside the scope of this thesis. Instead, three investigations aligned with the topics of the thesis are conducted to showcase the capabilities of the framework. First, the effect of the microstructure on the stiffness estimation is treated. Next, its influence on the delamination propagation is considered. Finally, the tunneling crack propagation of non-straight cracks is considered. This is done both without and with a microstructure present. The material properties of the fibers and matrix are taken from [QC14] based on typical Glass and Epoxy values. They are listed in table 4.

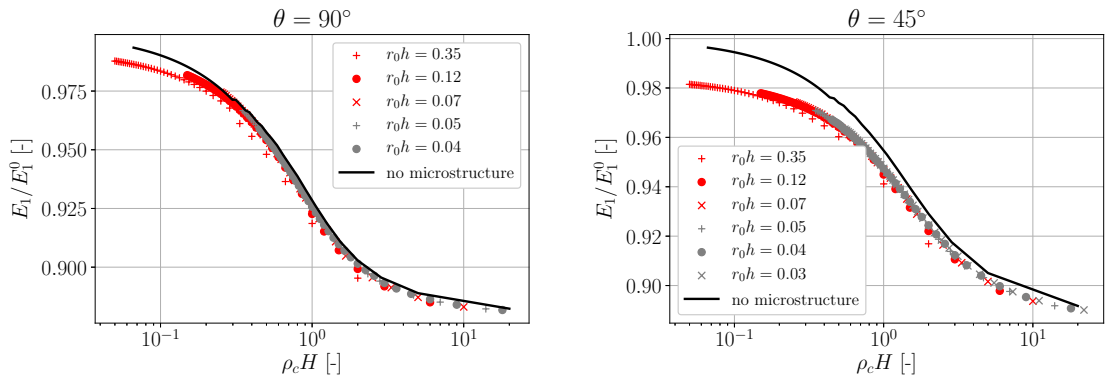
### 6.3.1. Stiffness Estimation and Degradation

The stiffness degradation  $\Delta E_1$  is investigated with a regular fiber alignment as shown on the left side of fig. 56. It is incorporated in the cracked layer of the layup  $[0/\theta/0/-\theta_c]_s$ , i.e the  $-\theta$ -layer, with the fiber and matrix materials presented in table 4. The material of the remaining

**Table 4** Fiber and matrix material properties I.

	$E$ [MPa]	$\nu$ [-]	$G$ [MPa]
Fiber	72000	0.20	30000
Matrix	4200	0.34	1567

layers is defined via the Halpin-Tsai rule using the fiber-density  $\varphi = 0.38$ . Assuming the same fiber crack spacing in both the  $x_1$ - and  $x_2$ -direction, only the fiber radius  $r_0$  can be varied. Thus a parametric study with respect to the tunneling crack density  $\rho_c$  is conducted at different fiber radii  $r_0$ . The results are provided for  $\theta = 90^\circ$  and  $\theta = 45^\circ$  in fig. 56. A comparison with the fully homogenized version, i.e. without a microstructure is made. Overall the tendencies are the same with the greatest errors at low crack densities. This is to be expected, as the influence of the cracked layer with the microstructure diminishes with an increasing crack density.

**Figure 56** Influence of the fiber-matrix microstructure on the stiffness degradation  $\Delta E_1$ , due to tunneling cracks using the layup  $[0/\theta/0/ -\theta_c]_s$ , and  $\varphi = 0.38$ .

Furthermore, a slight tendency towards the homogenized results is observed for decreasing fiber radii. This is therefore investigated more closely for  $\theta = 45^\circ$  in fig. 57. Here the stiffness degradation  $\Delta E_1$  is plotted against the fiber radius  $r_0$  at three crack densities  $\rho_c H = 0.5, 1, 2$ . The tendency is confirmed, however without a full convergence towards the results from the homogenized model. The final error is still under 1%, which means, that the homogenized model is accurate enough for most applications. The accuracy could likely be improved by using a better homogenization approach, as e.g. a finite element based approach instead of the Halpin-Tsai model. This is also in agreement with the results from [Her+21b], where larger deviations occurred, while using the Halpin-Tsai model, for cases with larger shear contributions, as is the case for an orientation of  $\theta = 45^\circ$ .

### 6.3.2. Delamination Propagation

Similarly to the previous study the layup  $[0/\theta/0/ -\theta_c]_s$  with a microstructure in the  $-\theta$ -layer is analyzed. Again a regular fiber distribution with the fiber density  $\varphi = 0.38$  is chosen. Now the influence of the fiber radius  $r_0$  on the energy release rate during delamination is investigated and illustrated in fig. 58 for both  $d_r = 0.1$  and  $d_r = 0.5$  at  $\theta = 45^\circ$ . Again, the tendencies between the

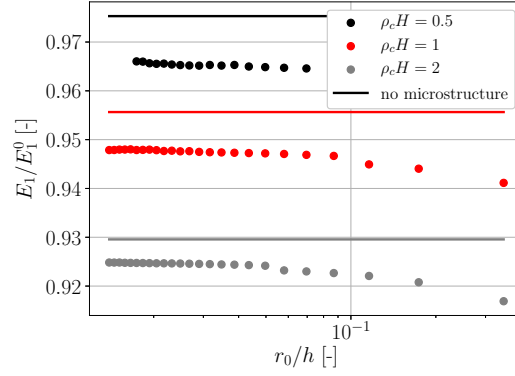


**Figure 57** Influence of the fiber radius  $r_0$  on the stiffness degradation  $\Delta E_1$  for the layup  $[0/\theta/0/-\theta_c]_s$ ,  $\theta = 45^\circ$ , and  $\varphi = 0.38$ .

homogenized and microstructure models are very similar with a few outliers in the microstructure model, likely caused by numerical difficulties for the large crack density cases. Furthermore, an oscillatory phenomenon occurs for the microstructure.

The errors between the two models are greater with a maximum of about 15%. Again, the error can likely be reduced by an improved homogenization method. The relatively large error does not necessarily have to be a cause for concern, as the results obtained with the microstructure are in this case always lower. Thus the homogenized model provides an upper bound estimate of the energy release rate, i.e. a conservative estimate with regard to crack propagation. This is however only an observation for this specific case and not a general rule, which should be investigated further.

### 6.3.3. Tunneling Crack Propagation

Finally, also the tunneling crack propagation is investigated further. Here two interesting aspects are studied non-straight cracks and the microstructure. First the non-straight cracks in a homogenized laminate are tackled to ensure, the correctness of the implementation presented in section 6.1. For this task, a simple model is constructed with a single crack in the  $\theta$ -layer of the  $[0/\theta/0/-\theta_c]_s$  layup. An illustration of the model is provided in fig. 59, where the parameter  $a \in [0, 0.5]$  defines the eccentricity of the crack.

The model is then used to set up a parametric study considering the influence of the influence of  $a$  on the tunnel cracking energy release rate  $\mathcal{G}$ , which is shown in fig. 60. The material is GlassFRP and two orientations  $\theta = 90^\circ$  and  $\theta = 45^\circ$  are considered. Here it is seen, that the energy release rate  $\mathcal{G}$  is maximal for  $a = 0$ , which is to be expected, as this is the crack with the smallest crack area and thereby least resistance. Furthermore, no mode II propagation is encountered for  $\theta = 90^\circ$ , which is also expected, as the crack is then aligned perpendicular to the load. Interestingly, the mode III component of the energy release rate increases to a certain point for  $a > 0$ . It is 0 for  $a = 0$ , as the problem then reduces to a vertically anti-symmetric crack not allowing a mode III crack opening.

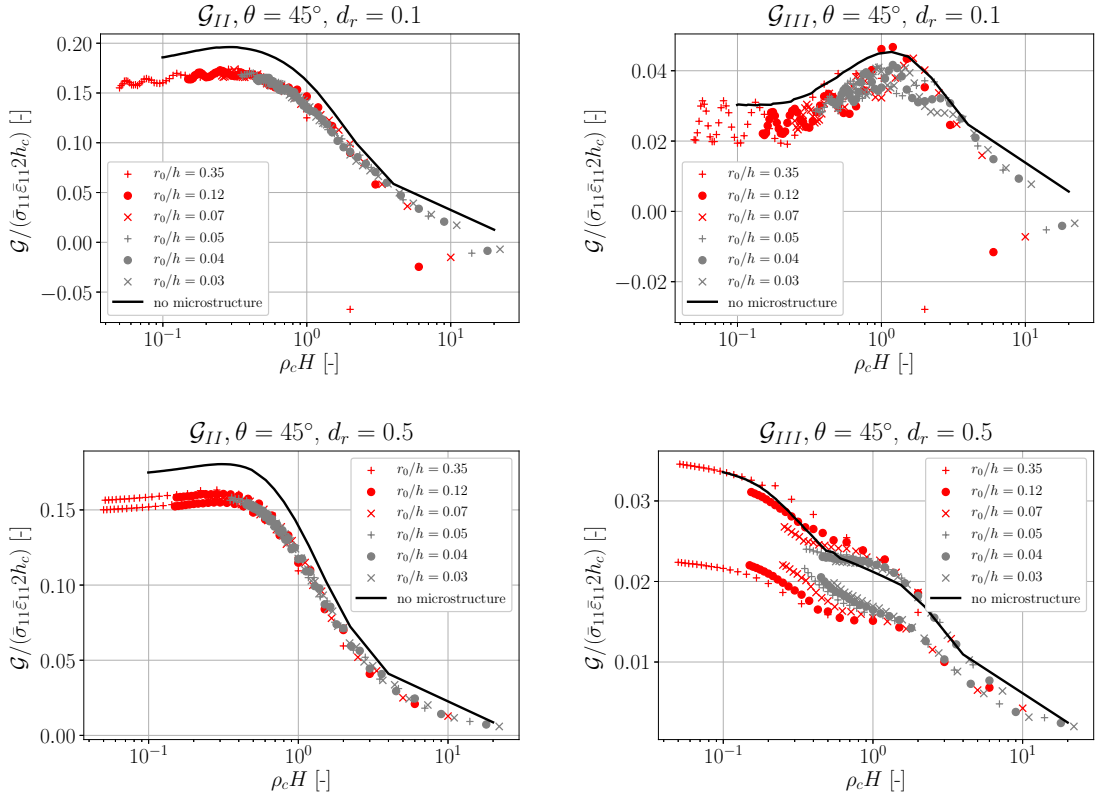


**Figure 58** Influence of the fiber-matrix microstructure on the delamination energy release rate  $\mathcal{G}$  using the layout  $[0/\theta/0/-\theta_c]_s$ ,  $\theta = 45^\circ$ , and  $\varphi = 0.38$ . Top: Delamination ratio  $d_r = 0.1$ . Bottom: Delamination ratio  $d_r = 0.5$ .

This anti-symmetry is however removed, as soon as  $a > 0$ , as is illustrated in the contour plots in fig. 63, where an in-plane sliding of the crack surfaces is seen. This explains, why the mode III energy release rate increases. The reason for its decrease afterward is the increase of the crack length countering this effect and thereby lowering the total energy release rate  $\mathcal{G}$ .

Important to note is also, that the computation of the energy release rate, as seen in eq. (6.9), is done with the total crack length  $l_c$ , while the normalization seen in fig. 60 uses the cracked layer height  $h_c$ . The choice was made, as it provides a better comparison for cracks with a varying crack length  $l_c$ . Furthermore, it can be argued, that the normalization with the crack length  $l_c$  is arbitrary, as the crack length in a real structure is not well-defined. Zooming in closer to the crack will always provide an increased resolution and thereby an increase in crack length. This is also known as the coastline paradox in fractal theory [Man82]. Nevertheless the crack length  $l_c$  given as a function of  $a$  is provided in fig. 62, as the crack length is well-defined in this specific case. Also note, that the issue of the definition of the crack length is not problematic in eq. (6.9), as first an integral is performed along the entire crack, which subsequently is divided by the crack length, removing the problematic definition of the crack length from the result.

Finally, the non-straight crack and fiber-matrix microstructure are combined in a single case. For this purpose, the CT-scan from [MMA21] is used for both the crack and the microstructure. Correspondingly the material parameters are also taken from [MMA21] and presented in table 5.

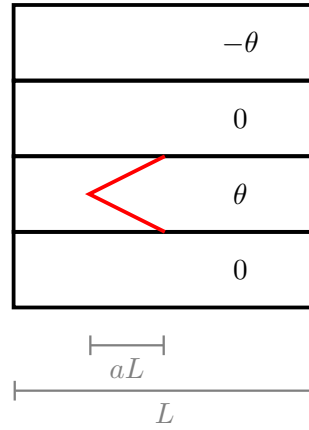


**Figure 59** Model of a non-straight crack defined via the eccentricity parameter  $a \in [0, 0.5]$  in the layup  $[0/\theta/0/ -\theta_c]_s$ .

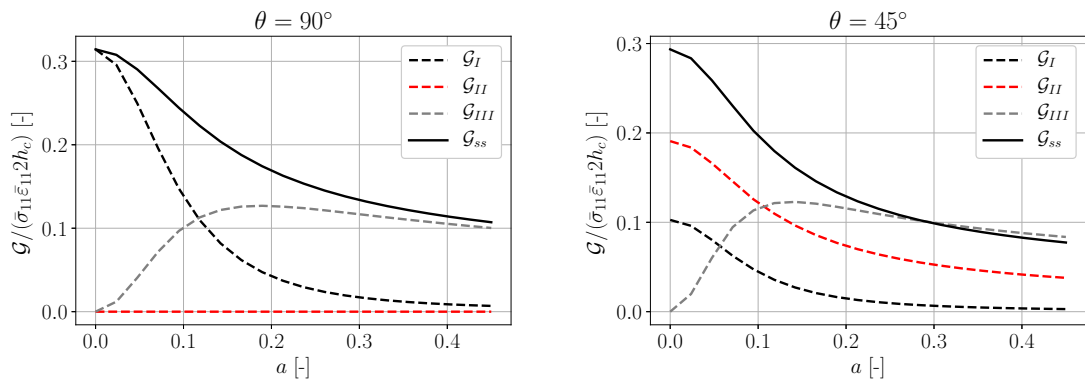


**Figure 60** Influence of the eccentricity parameter  $a$  on the tunnel cracking energy release rate  $\mathcal{G}$  in the layup  $[0/\theta/0/ -\theta_c]_s$  with the material GlassFRP.

Again only the cracked layer is modeled with a microstructure. Thus, the remaining materials use a homogenized material computed with the Halpin-Tsai model and a fiber density of  $\varphi = 0.4$ .

**Table 5** Fiber and matrix material properties II.

	$E$ [MPa]	$\nu$ [-]	$G$ [MPa]
Fiber	85000	0.22	34836
Matrix	3000	0.4	1071

One of the main conclusions from [Her+21b] was, that the homogenization approach is of great importance and that the Halpin-Tsai model, in particular, is not ideal for the energy release rate computation of tunneling cracks. Therefore unlike before, now a homogenization with a finite element RVE is performed using the Abaqus plugin from [McL17]. The resulting homogenized properties are listed in table 6.

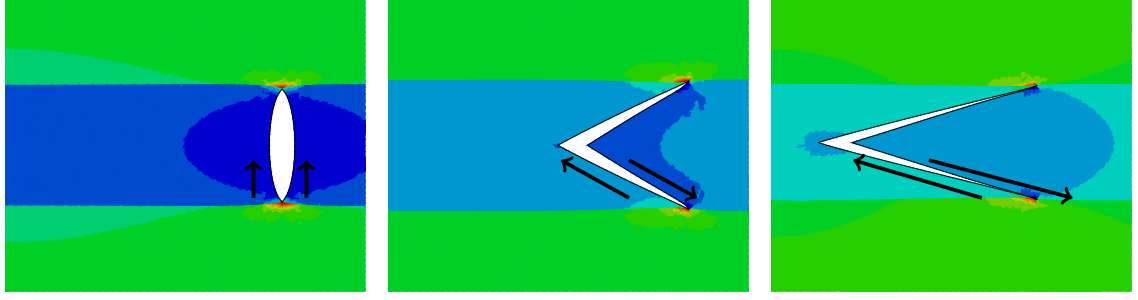


**Figure 61** Contour plot illustrating the increasing mode III energy release rate. From left to right:  $a = 0$ ,  $a = 0.2$ , and  $a = 0.4$ .

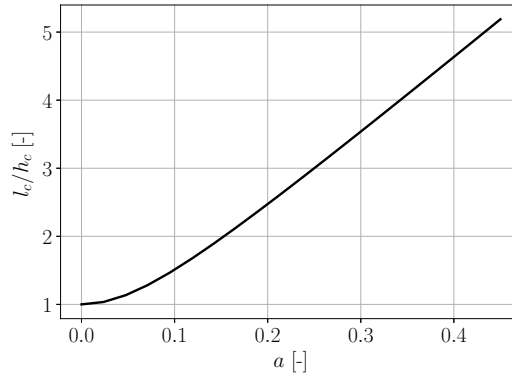


**Figure 62** The crack length  $l_c$  expressed as a function of the eccentricity  $a$ .

**Table 6** Homogenized material properties.

$E_L$ [GPa]	$E_T$ [GPa]	$E_{T'}$ [GPa]	$G_{LT}$ [GPa]	$G_{LT'}$ [GPa]	$G_{TT'}$ [GPa]	$\nu_{LT}$ [-]	$\nu_{LT'}$ [-]	$\nu_{TT'}$ [-]
34.28	7.459	7.661	2.259	2.423	2.265	0.3266	0.3195	0.5173

The considered layup is  $[0_4/\theta/0_4/-\theta_c]_s$ , where it is important to note, that the layup should be symmetric, but due to the irregular microstructure slight asymmetries are introduced. This does not pose a problem for the model, as they are not large enough to cause any noticeable bending effects, but mean, that the full laminate has to be modeled, instead of only the lower half. The model is then applied to three orientations  $\theta = 90^\circ$ ,  $\theta = 60^\circ$ , and  $\theta = 30^\circ$ , where for the sake of comparison a study is conducted with the non-straight crack and microstructure, with the non-straight crack in a homogenized material, and finally with a straight crack in a homogenized material. The results are listed in table 7.

First, the previously mentioned errors introduced by the projection can be noticed, as the sum of the individual energy release rates  $\mathcal{G}_I$ ,  $\mathcal{G}_{II}$ , and  $\mathcal{G}_{III}$  does not match the total energy release rate  $\mathcal{G}_{ss}$  exactly. To clarify, that this is indeed the reason, the computation has been repeated without the projection for  $\theta = 90^\circ$ , as shown in table 8. Here, the sum of the components results exactly in the total energy release rate. Another observable difference is, that the mode III contribution is significantly smaller, which makes sense, as it in an average sense is close to zero and only appears

**Table 7** Energy release rate of a non-straight crack in an irregular fiber-matrix microstructure with three orientations  $\theta = 30^\circ$ ,  $\theta = 60^\circ$ , and  $\theta = 90^\circ$ .

		$\frac{\mathcal{G}_I}{\bar{\sigma}_{11}\bar{\varepsilon}_{11}2h_c}$	$\frac{\mathcal{G}_{II}}{\bar{\sigma}_{11}\bar{\varepsilon}_{11}2h_c}$	$\frac{\mathcal{G}_{III}}{\bar{\sigma}_{11}\bar{\varepsilon}_{11}2h_c}$	$\frac{\mathcal{G}_{ss}}{\bar{\sigma}_{11}\bar{\varepsilon}_{11}2h_c}$
$\theta = 30^\circ$	straight crack	$2.6217 \cdot 10^{-3}$	$2.5694 \cdot 10^{-3}$	$8.0599 \cdot 10^{-15}$	$5.1911 \cdot 10^{-3}$
	non-straight crack	$9.8917 \cdot 10^{-4}$	$1.2884 \cdot 10^{-3}$	$1.0308 \cdot 10^{-3}$	$2.6117 \cdot 10^{-3}$
	non-straight crack with microstructure	$1.3622 \cdot 10^{-3}$	$1.6553 \cdot 10^{-3}$	$1.3135 \cdot 10^{-3}$	$3.3028 \cdot 10^{-3}$
$\theta = 60^\circ$	straight crack	$1.0237 \cdot 10^{-2}$	$2.3908 \cdot 10^{-3}$	$1.8095 \cdot 10^{-14}$	$1.2628 \cdot 10^{-2}$
	non-straight crack	$5.1525 \cdot 10^{-3}$	$1.5762 \cdot 10^{-3}$	$2.5063 \cdot 10^{-3}$	$8.5270 \cdot 10^{-3}$
	non-straight crack with microstructure	$7.0956 \cdot 10^{-3}$	$1.8318 \cdot 10^{-3}$	$2.3137 \cdot 10^{-3}$	$1.0366 \cdot 10^{-2}$
$\theta = 90^\circ$	straight crack	$1.6655 \cdot 10^{-2}$	$7.1438 \cdot 10^{-21}$	$4.3543 \cdot 10^{-14}$	$1.6655 \cdot 10^{-2}$
	non-straight crack	$8.7984 \cdot 10^{-3}$	$5.8646 \cdot 10^{-21}$	$3.1129 \cdot 10^{-3}$	$1.1908 \cdot 10^{-2}$
	non-straight crack with microstructure	$1.2202 \cdot 10^{-2}$	$1.5681 \cdot 10^{-20}$	$2.5203 \cdot 10^{-3}$	$1.4312 \cdot 10^{-2}$

if the local crack surface is taken into account. Even when taking the projection into account as in table 7, the mode III contribution is still always the smallest. Thus, if a material is considered with a fracture resistance independent of the modes or a larger fracture resistance in mode III, the projection method from fig. 55 is not necessary and the projection is not recommended, due to the numerical errors it introduces.

In general, the difference between the three computations in table 7 is most noticeable in the mode-mixities, i.e. the relative differences in the energies of the different modes. However, the dominant mode is always the same. Furthermore, an important observation is, that the total energy release rate is always maximal for the straight crack. Thus, the straight crack approximation in a homogenized medium seems to represent an upper limit and thereby yield a conservative estimate if crack growth is undesirable. This conclusion is only based on three computations and does not necessarily hold in general. However, when comparing the straight crack to the non-straight crack in the same homogenized material, it is always the case, as the crack surface area is greater for the non-straight crack. Interestingly the addition of the microstructure increases the energy release rate slightly, but in this case not enough to overtake the estimate provided by the straight crack. Although not proven in a general sense, it is to be expected, that the non-straight crack without a microstructure yields an upper estimate of the energy release rate and thereby the crack propagation rate. Thus when considering fatigue, it provides a lower estimate of the fatigue life.

**Table 8** Energy release rate of a non-straight crack in an irregular fiber-matrix microstructure at the orientations  $\theta = 30^\circ$ ,  $\theta = 60^\circ$ , and  $\theta = 90^\circ$  without the projection to the microscopic crack surface.

		$\frac{G_I}{\bar{\sigma}_{11}\bar{\varepsilon}_{11}2h_c}$	$\frac{G_{II}}{\bar{\sigma}_{11}\bar{\varepsilon}_{11}2h_c}$	$\frac{G_{III}}{\bar{\sigma}_{11}\bar{\varepsilon}_{11}2h_c}$	$\frac{G_{ss}}{\bar{\sigma}_{11}\bar{\varepsilon}_{11}2h_c}$
$\theta = 30^\circ$	non-straight crack with microstructure	$1.8950 \cdot 10^{-3}$	$1.6553 \cdot 10^{-3}$	$4.6172 \cdot 10^{-6}$	$3.3028 \cdot 10^{-3}$
$\theta = 60^\circ$	non-straight crack with microstructure	$8.8976 \cdot 10^{-3}$	$1.8318 \cdot 10^{-3}$	$1.1627 \cdot 10^{-4}$	$1.0366 \cdot 10^{-2}$
$\theta = 90^\circ$	non-straight crack with microstructure	$1.4261 \cdot 10^{-2}$	$1.1080 \cdot 10^{-23}$	$5.1097 \cdot 10^{-5}$	$1.4312 \cdot 10^{-2}$

Finally also a contour plot of the specimen oriented at  $90^\circ$  showing  $\sigma_{11}$  is provided in fig. 63. In the center, the  $-90^\circ$ -layer with the microstructure and the non-straight crack is seen. On the bottom and top of it, the  $0^\circ$ -layers with the homogenized material are seen, which the irregularity does not seem to impact much. Furthermore, the contour plot showcases the possible contact situations during the crack opening, as discussed in [Her+21b].

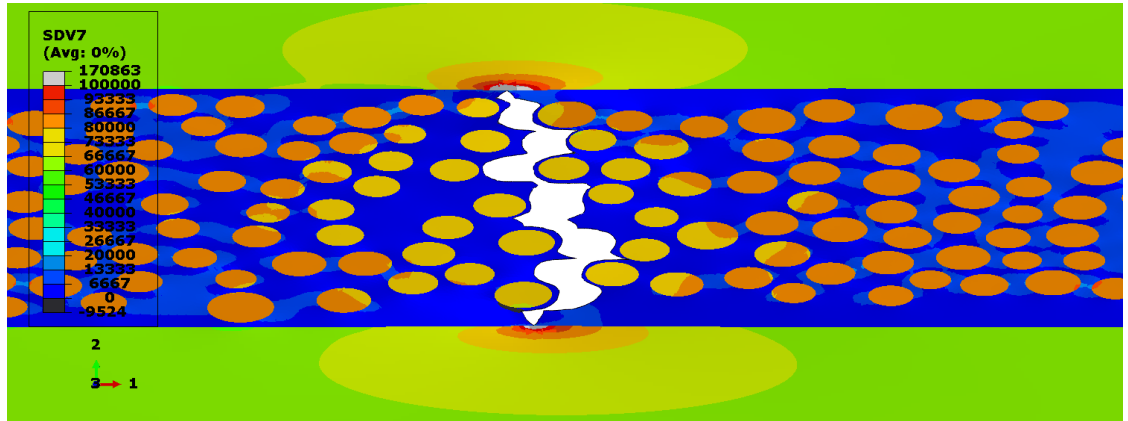


**Figure 63** Contourplot ( $\sigma_{11}$ ) of the non-straight crack embedded in a fiber-matrix microstructure using the layup  $[0_4/\theta/0_4/-\theta_c]_s$  oriented at  $\theta = 30^\circ$ .

The crack opening displacements  $\Delta u$  of the  $\theta = 30^\circ$  case can be compared to the ones obtained with the straight crack in the homogenous material, as seen in fig. 64. The non-straight character does not seem to influence the shape of the crack opening very much. However, the magnitude of the crack opening is affected, where the straight crack only opens about 85% when compared to the non-straight crack. Simultaneously, the reaction forces of the straight crack are however greater, resulting in the higher energy release rate presented in table 7.

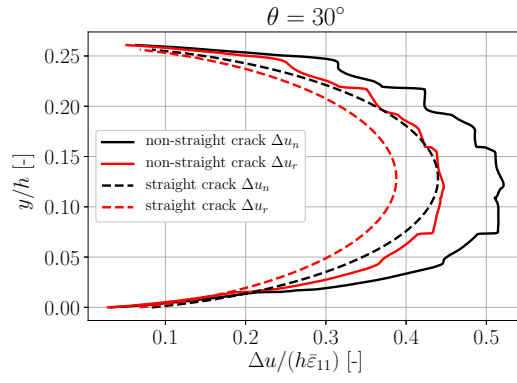


**Figure 64** Comparison of straight and non-straight crack profiles using the layup  $[0_4/\theta/0_4/-\theta_c]_s$  oriented at  $\theta = 30^\circ$ . The non-straight crack is embedded in a fiber-matrix microstructure, whereas the straight crack is in a homogenized material.

## 7. Discussion

It was demonstrated, that the off-axis framework from [Mik+21] has a potential in the field of fracture and composites, where it outperforms a lot of other methods in accuracy, computational efficiency, and ease of usage. However with that come several limitations, which will be clarified in the following. Furthermore, the assumptions used during this thesis, that could potentially be avoided inside the framework, are highlighted as well. Finally, possible extensions of the framework and applications are proposed as an outlook.

### 7.1. Limitations

The major limitation of the off-axis framework is, that it can only handle cracks oriented in a single direction, as multiple orientations would not allow the reduction to a 2D problem. This limitation is the most important, as multiple orientations are very common in laminates. This is because balanced laminates are typically desirable, which leads to at least two different orientations in the off-axis layers unless they are oriented at  $90^\circ$ . The limitation can however be circumvented if the interaction between the individually oriented cracks is negligible. This is the case, if the layers between the off-axis layers, i.e. the load-carrying layers, are sufficiently large, as shown in [CQ15]. This is not uncommon, as the load-carrying layers are the most important layers and therefore usually the largest. If the interaction can be neglected the individual cracks can be investigated separately and the results may be superposed.

Another critical limitation not discussed in this thesis is the compression side during fatigue, i.e. buckling. Buckling would most likely perturb the out-of-plane field and thereby violate the assumption of a steady-state in the off-axis direction. Therefore, buckling is probably difficult or even impossible to treat inside of this framework. Its effect is however an increased crack propagation rate, due to the interaction. Thus it might be sufficient to include this effect in the empirical power laws without modeling it inside the finite element model. However, if the compression behavior is either not dominated by buckling or if the buckling mainly occurs in the plane, compression could potentially be added to the model by introducing contact at the fracture surfaces.

Furthermore, the 2D nature of the model does not allow to have tunneling cracks, that aren't either fully tunneled or still tunneling, i.e. there is no in-between, that can describe half tunneled cracks. This is also the reason for the relatively rough axial stiffness prediction during the fatigue life computation. A full 3D model would produce a much smoother graph, as it could take the intermediate tunneling steps into account. A solution to this problem would be to smooth the graph via an interpolation of the points, as the points are still equivalent to the ones, that would be obtained with a 3D model. It is just the intermediate points, that are unknown, but also not absolutely necessary. Alternatively, an average crack density evolution approach could be employed,

that possibly circumvents this issue.

Similar to this issue are the edge effects of the laminate. It is always assumed, that the cracks are far away from the edges and thereby a steady-state off-axis field exists. This limitation is also not a concern, as the dimension of the layer heights and thereby the crack heights are significantly smaller than the width and length of the laminates. Therefore it is reasonable to assume and treat the laminate as infinite in both the width and length dimension. Hence, the edge effects can typically be neglected.

Finally, also a limitation concerning the fiber-matrix microstructure exists. The microstructure can only be added in layers oriented at angles different from  $0^\circ$ . As the circular fibers would reduce to rectangles, as the fibers are aligned parallel to the modeling plane. The rectangular fibers could be included, however, the slice would be arbitrary, as the slice parallel to the fibers is not invariant with respect to the out-of-plane direction. Thus the microstructure in the load-carrying layers can not be included. A workaround would be to study multiple slices and investigate the differences between different slices. Most likely the differences are small and it is acceptable to use an arbitrary slice to model the microstructure in the  $0^\circ$ -plies.

## 7.2. Assumptions

A variety of assumptions and simplifications has been made throughout this thesis, to simplify the proposed model. Not all of them are necessary and could be taken into account by extending the model.

The first and most prevalent assumption is the one of linearity, specifically linear elasticity. This is valid for the fiber material, but typically not the case for the matrix, which can show both visco-elastic behavior and plasticity, as mentioned in [GS99]. This does not pose a serious challenge for the off-axis framework, as the steady-state is probably still reached. However, the finite element implementation has to be extended to account for a non-linear finite element approach. Difficulties arise for the determination of the crack propagation properties, which until now were computed with linear elastic fracture mechanics. A possible alternative for the delamination would be a cohesive zone approach, as described in [Fei05] and [PP12]. However, the tunneling cracks are challenging, as it is questionable if the plasticity occurring at the crack tip can be taken into account while only considering the wake of the crack in the 2D model. This would have to be analyzed more closely including a possible validation with a 3D model. However, plasticity still only occurs in a limited sense in this model and these proposed changes imply a major overhead in workload with potentially only minor improvements. It is a common methodology to model fiber-reinforced composites with linear elastic materials, especially when considering high-cycle fatigue. In some cases plasticity does not even occur, as e.g. observed experimentally in [Mar14]. Thus if experiments show, that the plasticity only occurs in a limited sense for a specific layup, an extension of this framework in the context of high-cycle fatigue is not recommended.

A further simplification, that avoids non-linearities is the contact of the fracture surfaces. The contact directly affects the mode I crack opening and indirectly affects the mode II and mode III crack opening through friction. Thus contact affects mode I the most, which is however not as important as the mode I fracture contribution during contact is typically small. More interestingly is how mode II and mode III are affected, which according to [CMQ19] and [DS91] is negligible. However, when considering non-straight cracks contact becomes more important, as local contact occurs during the crack opening, which would typically not experience contact. As contact does not interfere with the energy-based methods for the estimation of the energy release rate, the implications of this assumption could be investigated. Again it requires an extension to a non-linear finite element implementation, which is however also useful for other analyses.

Related to the plasticity and the manufacturing process are the residual stresses, which were not taken into account. These can however be added, even without modeling the plasticity or introducing non-linearities to the model. This should not pose severe complications and is very interesting, as the residual stresses introduced during manufacturing, i.e. the curing process, have a major influence on the lifetime of the components, as discussed in [Nie13]. Thus an extension of the model with residual stresses and studies on its influence is highly recommended. This would create the possibility to directly link the steps during manufacturing to the cause of the crack propagation and thereby the fatigue behaviour of the laminate.

Another major assumption is the symmetry of the laminate, which ensures no bending coupling effects. In reality, most laminates in industry obey this principle, but when considering asymmetric defects, as e.g. an asymmetric microstructure or asymmetric delamination patterns, the laminate becomes asymmetric. This assumption is more a restriction, as the off-axis framework is capable of handling these coupling effects, as the steady-state is not violated by it and no additional far-field components are introduced, i.e.  $\bar{\epsilon}_{11}$ ,  $\bar{\epsilon}_{33}$ ,  $\bar{\epsilon}_{13}$  should still be sufficient. Until now the only asymmetric layup was the case with the microstructure from the CT-scan. Here the asymmetry is minimal and has an almost negligible influence. However, as stated, the framework should be capable of handling asymmetry, which should however first be verified and validated before applying it to asymmetric layups. The validation could be conducted with a basic comparison to classical laminate theory.

As mentioned before, only symmetric delamination patterns were investigated, i.e. the H-shaped configuration. However, a variety of configurations occur, as shown in fig. 7 and [CMQ19]. These could be added to the model to study their influence. The H-shaped pattern is the most common delamination shape and most likely no large differences between the modes will be observed. The occurrence of these variations in delamination modes is highly dependent on the underlying microstructure or other defects. Thus a possibility would be to study, the likelihood of a specific delamination pattern occurring given a specific microstructure. However, if the macroscopic behaviour is not influenced by the differences in delamination patterns, the value of this investigation is limited. The investigations are however also not difficult to implement and only require a slightly larger model, as both the horizontal symmetry and vertical antisymmetry

no longer exist. Thus the model would be four times as large and have four times as many elements. As the model is computationally cheap, this can easily be performed and would be a simple investigation.

Finally, a little, but noteworthy technical assumption was made during the implementation of the non-straight crack. It is assumed, that the crack shape is monotonically decreasing or increasing in the  $x_2$ -direction, which was done due to technical difficulties in Abaqus during the projection computations. This also means that this assumption is only necessary if the different energy release rate modes are to be determined via the projection approach.

### 7.3. Outlook

This thesis limited itself to the introduction of several basic, but useful applications, which should be investigated further depending on the purpose.

The most promising application is the prediction of the fatigue behavior and lifetime with algorithm 1. If it were to be validated via a series of experiments, the algorithm could have great potential. Thus, a series of experiments on a selection of laminates to determine the tunneling crack growth rate, delamination crack growth rate, the saturated crack density, the fracture resistance, and the corresponding stiffness degradation is highly recommended to determine the accuracy of the algorithm. Furthermore, it would provide insights on possibilities to improve the fatigue model, i.e. which of the previously mentioned assumptions are acceptable and which are questionable.

The fatigue algorithm can be improved in several ways. One major improvement would be the tunneling crack density evolution, where a more sophisticated approach from e.g. [CMQ17] could be employed. Here the tunneling crack initiation is determined via the local hydrostatic stress and local maximum principal stress inside a fiber-matrix RVE. Thus a permanent regular fiber-matrix microstructure inside the off-axis plies could be added to replace the RVE, such that the initiation criterion can directly be based on the computation inside the corresponding ply. Similarly, a criterion in the load-carrying layers could also be added to include the fiber-breakage and thus model the complete fatigue life cycle of a laminate.

Additionally, the remaining constitutive and even thermal parameters could be determined, instead of only the axial stiffness. This requires multiple simulations, which in the case of the out-of-plane and shear components increases the complexity of the model slightly, due to the boundary conditions. Inspiration could be taken from [MCQ18], where all constitutive parameters are determined with their periodic model. The material parameter approach could even be extended to a general homogenization model independent of laminate structures, where the only requirement is an invariant field in an off-axis direction. E.g. the fiber-matrix microstructure cross-section could be modeled in 2D oriented at  $90^\circ$  to determine all constitutive parameters including the out-of-plane shear, which otherwise would require a 3D RVE.

When considering the fiber-matrix microstructure and the non-straight cracks, more investigations with a variety of microstructures and crack shapes could be conducted, to ensure, that the approximation via the homogenization approach is indeed an upper estimate, i.e. in fatigue a conservative estimate. Instead of using a crack shape from a CT-scan attempts could be made to predict the actual crack shape via a cohesive zone approach, as e.g. presented in [Mar14], where the microcracks form at the fiber-matrix interfaces and coalesce. If the microstructure is in fact reconsidered, plasticity, contact, and the residual stresses on the microstructure level could be considered. As stated before, plasticity introduces several severe complications, which might not be unifiable with the current framework. However, the contact at the tunneling crack fracture surface is interesting. Also, the residual stresses on the microstructure level are interesting, as these can then be related to and used to estimate the macroscopic residual stresses. As mentioned before an investigation of the macroscopic residual stresses, i.e. in the homogenized model are also important, as these can be related to the manufacturing process. Thus the different variables during manufacturing can thereby be related to the lifetime.

Another aspect, that has already been prepared inside the framework is multi-axial loading. In this thesis, only uni-axial loading has been considered. The framework is however capable of applying all possible load combinations. Note, however, that the off-axis framework has only been validated for the three normal loads. For the shear loads, special care has to be taken during the application of the boundary conditions. This is also important to remember if an attempt is made to extract the remaining constitutive properties.

Lastly, several implementational improvements could be made to increase computational efficiency. Currently, the mesh is composed of uniformly sized quadrilaterals, in the absence of a fiber-matrix microstructure. This is a waste of resources, which can be avoided by solely refining the mesh at the crack tips. The mesh could be improved even further with quarter elements [Bar74] at the crack tips, that capture the weak stress singularity in linear elastic fracture mechanics accurately. This requires an extension of the off-axis user element library. Additionally, the user element implementation is implemented in a sequential manner and not making use of the parallel architecture. Thus, a parallel implementation is highly desirable to reduce simulation times, especially if fiber-matrix microstructures are to be considered.

On a different scale, further applications of the off-axis finite element framework could be explored, that possibly aren't even related to fracture or fiber-reinforced composites. Thus applications with the inherent off-axis property are to be identified and thereupon tackled with the framework.

## 8. Conclusion

The answer to the main question from the aims and objectives in chapter 3, if the specialized off-axis finite element framework from [Mik+21] can be used as a tool in different tension-tension fatigue damage mechanisms in fiber-reinforced composites, is yes. A periodic finite element model was developed and used to predict the axial stiffness degradation caused by tunneling and delamination cracks, the delamination crack propagation, and the tunneling crack propagation. Not only were the predictions in good agreement with results from literature but also the efficiency of the computations was impressive. The 2D model is capable of predicting the stiffness degradation and the energy release rate within seconds or minutes, depending on the crack density, and thereby has a clear advantage over previous expensive 3D numerical models or complex analytical models.

Additionally, it was shown, how the energy release rates can be used to predict the entire fatigue behavior until fiber-breakage via Paris-like power laws. The method is however not validated yet but shows potential. The efficient computation of the energy release rate is not only useful for the crack propagation prediction, but also during experiments, where the Paris-like power laws are identified, as here the crack growth rate is related to the energy release rate.

Finally, also the influence of a fiber-matrix microstructure in the laminate model is investigated. Preliminary results show, that the commonly used, homogenized models seem to represent an upper bound for the crack propagation. Thus for most applications, the homogenization approach seems safe and reliable.

Overall a wide variety of problems have been identified, that can be tackled with the developed periodic finite element model based on the off-axis finite element from [Mik+21]. Due to the variety of problems, not all of them have been tackled in-depth. But a lot have been identified and possible solution strategies have been provided, thus creating a breeding ground for more in-depth studies with possibilities of extending the framework.

## A. Appendix

### A.1. Difference between Load-Controlled and Displacement-Controlled Energy Release Rate Computation

Consider the simplified model of a laminate presented in fig. 65. The upper ply is represented by the blue spring with stiffness  $k_1$ , whereas the remaining plies are represented by the spring with stiffness  $k_2$ . Additionally a spring with stiffness  $k_b$  is added to model the remaining stiffness of the laminate, that is unaffected by the crack growth. The model is either loaded with a prescribed displacement  $\Delta$  or a prescribed force  $N$ . Two situations are considered. The uncracked state, situation 1, where the blue spring is intact, and the cracked state, situation 2, where the blue spring is removed, i.e. no stiffness remains.

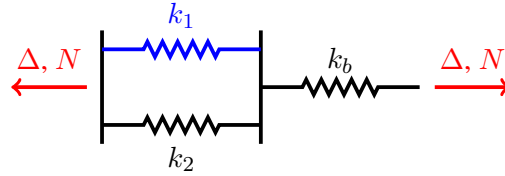


**Figure 65** Toy-example illustrating the differences during the computation of the energy release rate for load-control and displacement control. The blue spring is used to demonstrate the crack growth. Before the propagation the blue spring is intact with the stiffness  $k_1$  and afterward it is removed, thus resulting in a zero stiffness.

For the two situations, the stiffness of the total system can be expressed with  $K_1$ , and  $K_2$ .

$$K_1 = \left( \frac{1}{k_1 + k_2} + \frac{1}{k_b} \right)^{-1} \quad K_2 = \left( \frac{1}{k_1} + \frac{1}{k_b} \right)^{-1}$$

#### A.1.1. Load-Control

If a load-controlled approach is chosen, where the force  $N$  is constant throughout the two situations, the displacements  $\Delta$  can be computed as

$$\Delta_1 = \frac{N}{K_1}, \quad (\text{A.1})$$

$$\Delta_2 = \frac{N}{K_2}. \quad (\text{A.2})$$

This enables the computation of the differences in the external work  $\Delta W$  and the internal energy  $\Delta U$  as

$$\Delta W = W_2 - W_1 = -\Delta_2 N + \Delta_1 N = -K_2 N^2 + K_1 N^2 = -N^2 \frac{k_1}{(k_1 + k_2)k_2}, \quad (\text{A.3})$$

$$\Delta U = U_2 - U_1 = \frac{N^2}{2K_2} - \frac{N^2}{2K_1} = \frac{N^2}{2} \frac{k_1}{(k_1 + k_2)k_2}, \quad (\text{A.4})$$

which can be used to estimate the change in potential energy  $\Delta\Pi$ , due to the crack propagation.

$$\Delta\Pi = \Delta U + \Delta W = \frac{N^2}{2} \frac{k_1}{(k_1 + k_2)k_2} \quad (\text{A.5})$$

Here, it is observed, that the change in external work is double the change in internal work with the opposite sign, which is in accordance with Clapeyron's theorem [FT05]. Note however, that this is not always the case, but seems to be upheld for the laminates in this work. Due to this relation, two possibilities for the computation of  $\Delta\Pi$  arise. The first possibility is the estimation via the internal energy, i.e. via eq. (2.8). For this purpose, the internal force  $N_i$  in situation 1 and the displacement  $\Delta_i$  in situation 2 at spring 1 are computed as

$$N_i = \frac{k_1}{k_1 + k_2} N, \quad (\text{A.6})$$

$$\Delta_i = \frac{1}{k_2} N. \quad (\text{A.7})$$

The quantities can be combined to estimate the change in internal energy and thereby also the change in potential energy.

$$\Delta\Pi = \Delta U_i \frac{1}{2} N_i \Delta_i = \frac{N^2}{2} \frac{k_1}{(k_1 + k_2)k_2} \quad (\text{A.8})$$

Alternatively, the external work can be used to estimate the change in potential energy, which can be reformulated in terms of the compliance  $C$ , and corresponds to the compliance method seen in [And17].

$$\Delta\Pi = \frac{1}{2} \Delta W = \frac{N}{2} (-\Delta_2 + \Delta_1) = \frac{N^2}{2} (-C_2 + C_1) = \frac{N^2}{2} \Delta C \quad (\text{A.9})$$

The equivalence of the approaches has also successfully been investigated empirically with a variety of laminates.

### A.1.2. Displacement-Control

Instead of using a constant force throughout situation 1 and 2, a constant displacement  $\Delta$  is applied in the displacement controlled approach. This yields the following forces for each situation

$$N_1 = K_1 \Delta, \quad (\text{A.10})$$

$$N_2 = K_2 \Delta. \quad (\text{A.11})$$

No external work is performed, due to the displacement being constant. Thus, the change in potential work is equal the change in internal work, expressed as

$$\Delta\Pi = \Delta U = U_2 - U_1 = \frac{K_2 \Delta^2}{2} - \frac{K_1 \Delta^2}{2} = \frac{k_b^2 k_1 \Delta^2}{2(k_b + k_1 + k_2)(k_b + k_2)}. \quad (\text{A.12})$$

This leads to a different expression, than encountered in eq. (A.5). Interestingly the stiffness  $k_b$

also appears. It can be shown, that the magnitude of the difference is given by the differences in areas from fig. 38. Thus the displacement-control leads to an underestimation of the change in potential energy and thereby the energy release rate. In order to compare the different results, the prescribed displacement  $\Delta$  is expressed in terms of the required force  $N$  in situation 1

$$\Delta = \frac{N}{K_1}, \quad (\text{A.13})$$

which is inserted in eq. (A.12).

$$\Delta\Pi = \frac{N^2}{2} \frac{k_1(k_1 + k_2 + k_b)}{(k_2 + k_b)(k_1 + k_2 + k_b)^2} \quad (\text{A.14})$$

Again, a difference is observed. However, in the case, that the stiffness  $k_b$  goes towards zero, an equivalence is reached.

$$\lim_{k_b \rightarrow 0} \frac{N^2}{2} \frac{k_1(k_1 + k_2 + k_b)}{(k_2 + k_b)(k_1 + k_2 + k_b)^2} = \frac{N^2}{2} \frac{k_1}{(k_1 + k_2)k_2} \quad (\text{A.15})$$

This raises the question of when the stiffness  $k_b$  can be considered zero. In the previous work performed in [Mik+20] and [Mik+21] a displacement-controlled approach was applied. Here, a finite number of cracks was embedded in a very long laminate, that in principle could be considered infinitely long. In this case the stiffness unaffected by the crack  $k_b$  can be considered to be zero, due to the infinite length. Thus in this case the two approaches are equivalent. However, in this thesis, where infinitely many cracks appear due to the periodicity of the problem, differences arise, and the force-based approach has to be used.

## A.2. Program Documentation

The code is available in a git repository<sup>1</sup>. The driver files, named `Config.py` and written in Python define the model and are the files, that are to be run through Abaqus. Five driver files are supplied to showcase the different possibilities with the framework.

- `Config_axialstiffness_VCCT.py`
- `Config_tunnelcrack.py`
- `Config_nonstraightcrack.py`
- `Config_multipletunnelcracks.py`
- `Config_fatigue.py`

The driver file will make use of the `laminatemodel.py` file defining the laminate model with its cracks and of the helper functions and classes defined in `utilities.py`. Furthermore the `laminatemodel.py` requires the Fortran subroutines `OA2D.f` and `koutvar.inc.f` for the

---

<sup>1</sup> <https://github.com/Leon-Herrmann/Fracture-Modeling-with-OA2D>

user elements of the off-axis framework including their visualization through the shadow element technique discussed in [Mik+21]. An overview of this structure including the contents of the individual files is provided in fig. 66.

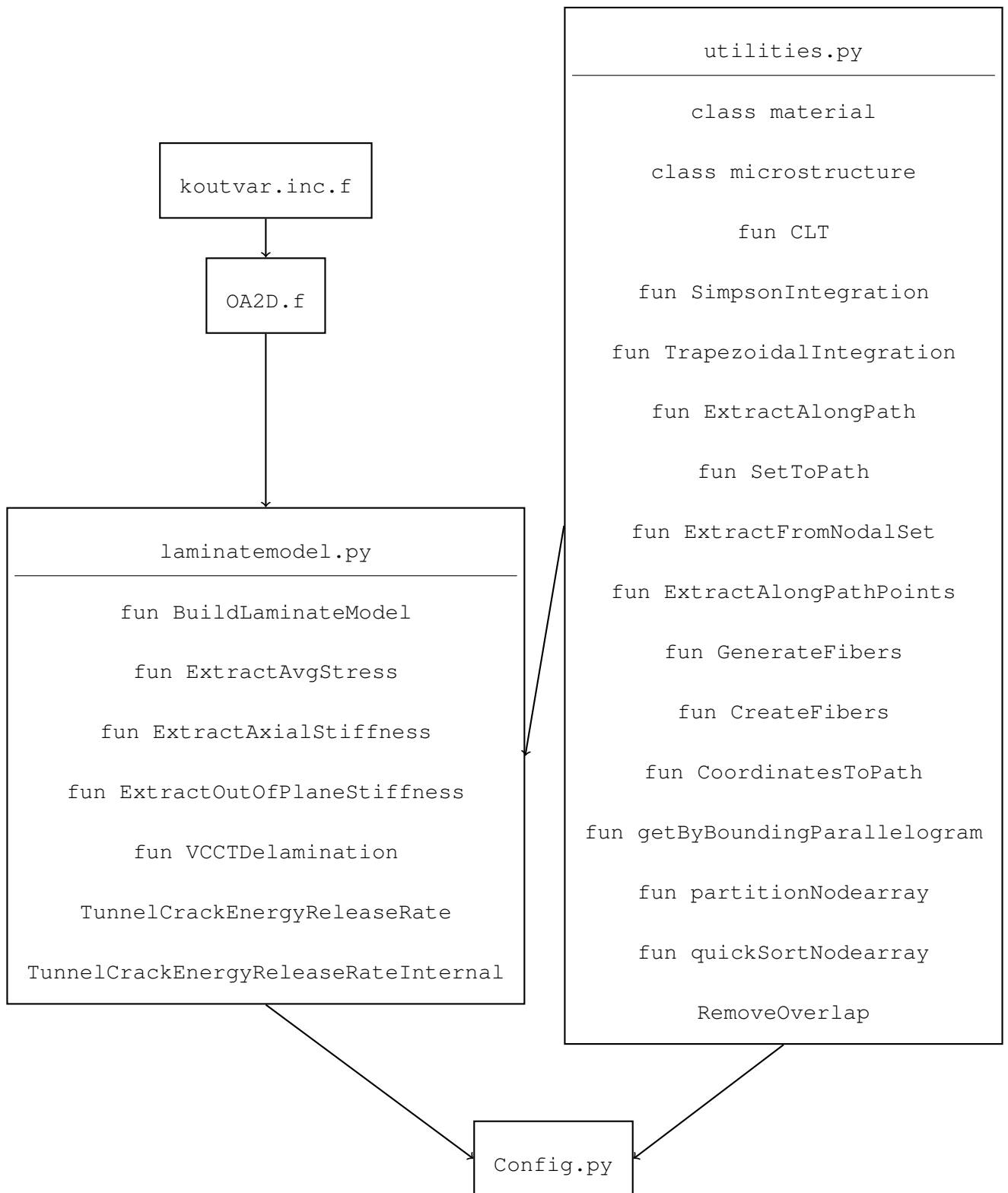


**Figure 66** Program structure.

The most important function inside the `laminatemodel.py` file is `BuildLaminateModel`, which creates the entire finite element model including the modifications of the input file to accommodate the off-axis framework. The remaining functions are all related to the post-processing, i.e. extracting the average stresses, the axial stiffness, and the energy release rates.

Due to its importance, the parameters of `BuildLaminateModel` are explained. For this task, an example model is provided in fig. 67. The geometry of the model is defined by the following parameters.

```
thetaB
rhoH
layup_heights = [1,2,1,2]
layup_angles = [thetaB,0,-thetaB,0]
```

The crack at the boundary as seen in fig. 67 together with the delamination in blue, are defined with the following two arrays.

```
layup_crack = [1,0,0,0]
layup_delaminationcrack = [0,1,0,0]
dr
```

The material is defined via the `material` class defined in `utilities.py`. The applied load on the left edge is defined with `Ni` as an array of the three components, normal, out-of-plane or out-of-plane shear. Via the boolean parameter `force_bc` either a force or displacement boundary condition may be selected. Furthermore, a crack on the left boundary can be introduced with

```
crack_left = True
layup_crack_left = [0,0,1,0]
```

which in this example would introduce a crack in the `-thetaB` ply.

The mesh is defined by the parameter `nle`, which in the absence of both non-straight cracks and a fiber-matrix microstructure, is defined as in fig. 67a, i.e. the element length. It might however be modified, if the parameter `nle_mod` is `True` so that it fits with the delamination crack. In the case of a microstructure or non-straight cracks `nle` will simply be close to the average element length.

Furthermore, the user material subroutine for the visualization may be turned off, via the boolean parameter `UMAT`, which is however not recommended, as the computational speed-up is small and it is required for the defined post-processing functions.

Interior cracks, as shown in fig. 67b, may be defined with the following parameters

```
crack_int = [[x1, x2, x3], [y1, y2, y3]]
crack_int_active = [0, 1, 0, 0]
crack_int_RF
```

where `crack_int_active` defines the plies in which the crack is present and `crack_int` the coordinates, that are rescaled to fit inside the corresponding ply. The boolean `crack_int_RF` states if the crack is to be tied together or not, so that the reaction forces can be extracted if set to `True`.

The microstructure is defined via the class `microstructure` from `utilities.py`, where the following members are used for the example illustrated in fig. 67b. In this case a regular microstructure is defined via `regular=True`, whereas an irregular microstructure is defined via `regular=False` with the corresponding coordinates in the array `fiber_arr`.

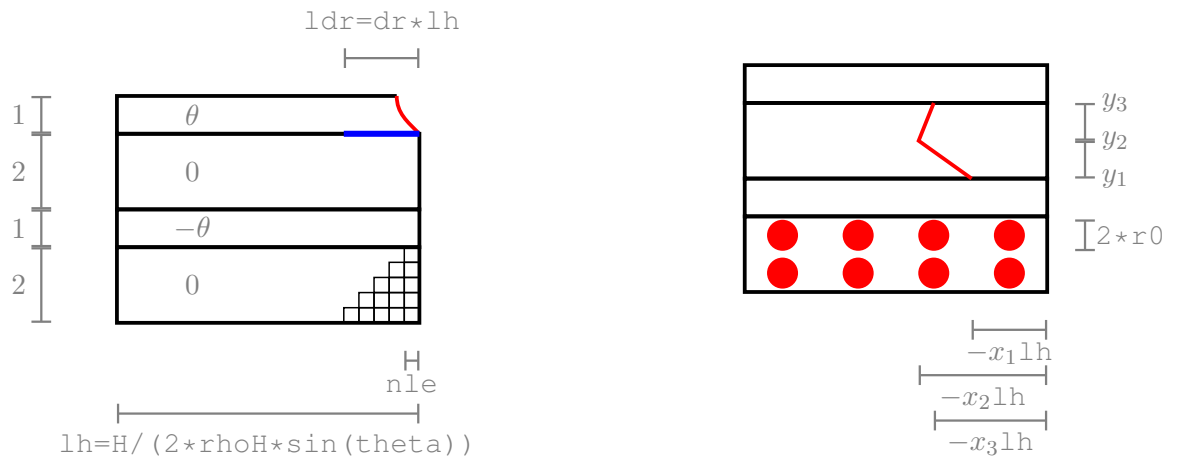
```
layup_microstructure = [0, 0, 0, 1]
nx = 4
ny = 2
r0
```

Finally, also the symmetry boundary condition at the top edge can be turned off with the boolean `symmetry` if a non-symmetric laminate is to be analyzed. Here, the symmetric boundary condition is replaced by a homogeneous Dirichlet boundary condition in the  $x_2$ -direction at a single node to prevent rigid body movement.

Lastly, also the model names, to be used inside the Abaqus environment can be changed.

```
NameModel
NameJob
NamePart
NameInstance
```

This is useful if multiple models with different names are to be created, as is e.g. required for the computation of the energy release rate of the tunneling cracks.



(a) Base model with tunneling cracks and delamination.

(b) Interior cracks and fiber-matrix microstructure.

**Figure 67** Model Description of the model defined in `BuildLaminateModel`.

To showcase the different possible inputs and how they are handled an example configuration is supplied in Listing A.1, which produces the model shown in fig. 68.

```

1 import LaminatedModel
2 import utilities
3 import math
4 import numpy as np
5
6 # geometrical definitions
7 dr = 0.3
8 rhoH = 0.5
9 theta = -90.
10
11 thetaB=math.pi/180.*theta #radians
12
13 # mesh
14 nle=0.05 # characteristic element length
15
16 # loading
17 Ni = np.array([1e5,0,0]) # [N1, N3, N13]
18
19 # material properties
20 mat = utilities.material(E1=30620., E2=8620., E3=8620.,
21                          nu23=0.33, nu13=0.29, nu12=0.29,
22                          G23=2900., G13=3250., G12=3250.)
23
24 # layup definition
25 layup_crack = np.array([1,0])
26 layup_delaminationcrack = np.array([0,1])
27 layup_angles = np.array([thetaB,-thetaB])
28 layup_heights = np.array([1.,1.])*0.5
29
30 # microstructure definition
31 mic = utilities.microstructure(layup_microstructure=np.zeros(len(layup_crack))
32                               )
33
34 # abaqus model parameters
35 UMAT = True
36
37 NameModel='CompModel'
38 NameJob='CompJob'
39 NamePart='Laminated'
40 NameInstance='Laminated_0'
41
42 # classical laminate theory calculation for the normalization
43 layup_active = np.ones(len(layup_crack))
44 eps, sig_0, sig_0_l = utilities.CLT(layup_angles, layup_heights, mat,
45                                     Ni, layup_active)
46 K1_CLT = Ni[0] / np.sum(layup_heights) / eps[0]
47 K3_CLT = Ni[1] / np.sum(layup_heights) / eps[1]
48
49 # ply discount as lower bound of stiffness drop
50 layup_active = layup_active - layup_crack
51 eps_pd, sig_0_pd, sig_0_l_pd = utilities.CLT(layup_angles, layup_heights, mat,
52                                               Ni, layup_active)

```

```

52 K1_CLT_pd = Ni[0]/ np.sum(layup_heights) / eps_pd[0]
53
54 # create the model
55 job, NameJob, nle_adjusted, num_nodes = LaminareModel.BuildLaminareModel(dr,
56     rhoH, thetaB, mat, Ni,
57     layup_crack, layup_delaminationcrack,
58     layup_angles, layup_heights,
59     nle, UMAT, mic)
60
61 mdb.jobs[NameJob].submit(consistencyChecking=OFF)
62 job.waitForCompletion()
63
64 # postprocessing
65 if Ni[0] != 0:
66     K1 = LaminareModel.ExtractAxialStiffness(Ni, rhoH, thetaB, layup_heights)
67     K1_norm = K1 / K1_CLT
68
69 if dr != 0.:
70     G1, G2, G3, dU1 = LaminareModel.VCCTDelamination(layup_heights,
71     layup_delaminationcrack, layup_crack, nle_adjusted, sig_0, eps)

```

Listing A.1: Example configuration file

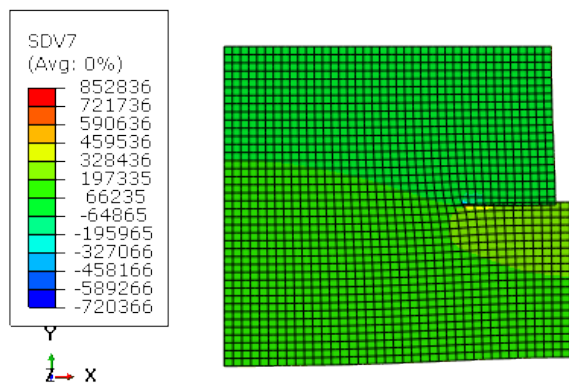


Figure 68 Model produced by configuration file from Listing A.1. Contourplot shows the normal stress in the  $x_1$ -direction  $\sigma_{11}$ .

### A.3. Appended Manuscripts

# An efficient stiffness degradation model for layered composites with arbitrarily oriented tunneling and delamination cracks

Leon Herrmann<sup>c,\*</sup>, Lars P. Mikkelsen<sup>a,\*\*</sup>, Brian N. Legarth<sup>b</sup>, Fabian Duddeck<sup>d</sup>, Christian F. Niordson<sup>b</sup>,

<sup>a</sup>Department of Wind Energy, Technical University of Denmark, DK-4000 Roskilde, Denmark

<sup>b</sup>Department of Mechanical Engineering, Solid Mechanics, Technical University of Denmark, DK-2800 Kgs. Lyngby, Denmark

<sup>c</sup>Chair of Computational Modeling and Simulation, Technical University of Munich, D-80333 Munich, Germany

<sup>d</sup>Chair of Computational Mechanics, Technical University of Munich, D-80333 Munich, Germany

---

## Abstract

*Tunneling and delamination cracks are two of the most important damage mechanisms encountered in fiber-reinforced composites. The damage is accompanied by a loss in stiffness. A periodic 2D finite element model is proposed to identify the axial stiffness degradation for arbitrarily oriented tunneling cracks, as long as the cracks are aligned in a single direction. This is achieved with a previously developed off-axis framework taking the 3D deformation into account via a special kinematic formulation. The proposed model is successfully validated against a variety of cases from literature. Furthermore, a good agreement with the ply discount estimate is reached when the damage is saturated. Not only is the model capable of producing results, that were previously only possible with expensive 3D models, or complex analytical methods, but at the same time, it is achieved with remarkably small finite element models and thereby only takes seconds for the computations. The model is made available in form of a Python script and can represent any arbitrary layup. Lastly, the model is applied to a variety of layups to showcase its capabilities.*

*Keywords:* Stiffness estimation, Stiffness degradation, Tunnel cracks, Delamination, Laminate, Finite element method, Damage, Fracture mechanics

---

## 1. Introduction

Fiber-reinforced composites have become highly desirable materials in a variety of industries, due to their high strength and stiffness to weight ratio. During their lifetime, they experience several damage mechanisms. To ensure the safety and reliability in their usage, it is essential, that these mechanisms are understood. They can be described in three steps, as described in Jespersen et al., Zhang and Herrmann, and Crossman and Wang. This is shown in figure 1, where a [0/90] layup is chosen for illustration purposes. In the first stage, tunneling cracks, marked in red initiate in the off-axis layers, i.e. in this case the 90°-layer, and tunnel along the fibers. This occurs in a sequential manner leading to a periodic distribution of tunneling cracks. The cracks lead to stress concentrations at the interface to the neighboring plies, which then leads to a decohesion of the layers, marked in blue. This second stage is referred to as the delamination. Finally, the damage in the off-axis layers weakens, the entire laminate sufficiently, leading to fiber breakage in the load-carrying layers and thereby representing the third stage. The fiber breakage quickly

---

\*Corresponding author. leon.herrmann@tum.de

\*\*Corresponding author. lapm@dtu.dk

leads to fiber-pullout and thereby a full separation of the laminate, i.e. the end of the laminate.

Important for the deployment of fiber-reinforced composites is not only the prediction of their lifetime but also of their performance. In particular, the stiffness degradation caused by the damage mechanisms is of interest. This is both important for its usage, but also for monitoring methods, that determine the amount of internal damage based on the stiffness degradation. The greatest falls in stiffness typically occur in the first and third stages. However, also the second stage is important.

A variety of tools exist to determine the stiffness degradation due to both tunnelling, and delamination cracks. A good overview is provided in Carraro and Quaresimin, where analytical, semi-analytical, numerical, and even variational approaches are compared. Even though, many approaches exist, most lack either flexibility, simplicity, or efficiency. The proposed model dealing with tunnelling, and delamination cracks attempts to circumvent these issues.

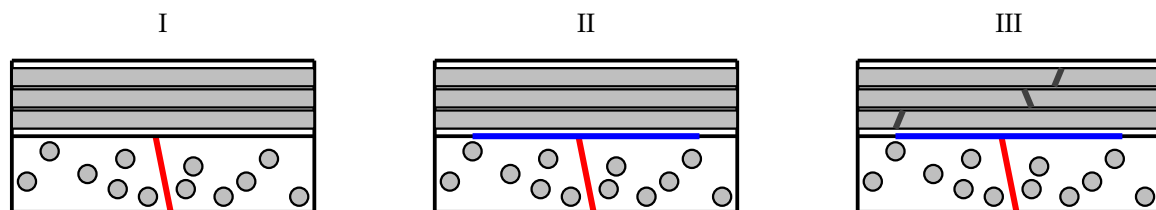


Figure 1: The three damage mechanisms in fiber reinforced composites under tension. I: Tunnelling cracks (red) are initiated and propagated in off-axis layers. II: The stress concentrations due to the tunnelling cracks initiate delamination cracks (blue) between the off-axis layers and load-carrying layers. III: Fiber fracture (dark gray) of the load-carrying fibers leads to a major loss in strength and thereby leads to final failure.

## 2. Problem

The stiffness degradation resulting from tunnelling cracks and delamination (the damage mechanism I and II in Fig. 1), in a uniaxially loaded symmetric laminate with layup  $[0/\theta/0/-\theta]_s$  is considered. This layup is also considered in Mikkelsen et al. (a), and Mikkelsen et al. (b). The tunnelling cracks are all oriented in the same direction, which is given by the fiber orientation  $\theta$ . The plies with tunneling cracks in a layup are always denoted by a subindex  $c$ , i.e.  $[0/\theta/0/-\theta_c]_s$ .

In the case of tunnelling and delamination cracks a steady state condition can be assumed, when the tunnelling cracks are only oriented in a single direction and the edge effects of the laminate can be neglected. This is a reasonable assumption as long as the length and width of the laminate are much greater than the height. The laminate is illustrated in Fig. 2, where the  $(x_1, x_2)$ -plane and the  $(x_1, x_3)$ -plane, i.e. the side and the top view of the laminate are illustrated. The stress and strain fields are invariant with respect to the  $x_L$ -axis, i.e. along the cracks, marked in red. Hence, the problem is essentially a 2D problem even for arbitrarily angles  $\theta$ .

As symmetric laminates are considered in this work only one-half of the laminate height is analyzed as shown in Fig. 3 by the red horizontal dashed line. The framework can however be applied to arbitrary layups with the only restriction being, that the cracks have to be aligned in the same direction. The layer

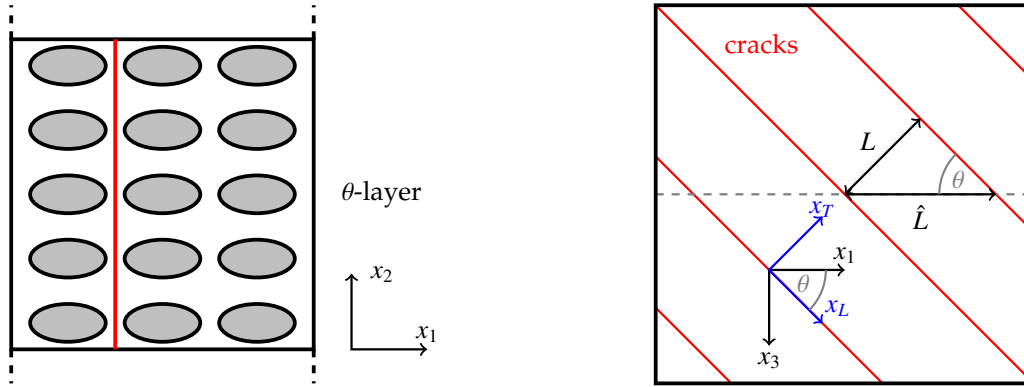


Figure 2: The cracked laminate. Left: Side view in  $(x_1, x_3)$ -plane showing the cracked  $\theta$ -layer. Right: Top view in the  $(x_1, x_3)$ -plane showing the periodic cracks in red, the distances between the cracks  $L, \hat{L}$  and the global and local coordinate systems.

height is indicated with  $h$ . Here all layers have the same height, which does not always have to be the case. The half height of the laminate is then denoted as  $H$  and the half height of the crack as  $h_c$ . Furthermore, a uniform tunneling crack distribution is assumed, i.e. the crack spacing,  $L$ , is constant. This is in agreement with experimental observations in Carraro et al., and Jespersen. Due to the constant crack spacing, a tunneling crack density,  $\rho_c = 1/L$ , may be defined and will from now on be used to define the crack spacing. The implications of assuming a constant crack spacing on the stiffness were investigated and are discussed later. This assumption permits a further simplification of the model to a periodic model, as also indicated in Fig. 3 by the blue vertical dashed lines around a full period. Note also, that the normal distance between the cracks  $L$  can be projected onto the  $x_1$ -axis by  $\hat{L} = L/\sin(\theta)$  for  $\theta \neq 0$ , see Fig. 2.

Additionally, the delamination caused by the stress concentrations of the tunneling cracks is added to the model. It is introduced at the tips of the tunneling cracks and travels along with the neighboring interface. It is indicated in blue in Fig. 3. Note, also, that the usage of the two symmetry planes shown in Fig. 3 means, that the delamination is also symmetric and occurs in a so-called H-shape, as discussed in Carraro et al.. The H-shaped delamination is the most dominant, but others exist. In this work, only H-shaped delamination is considered, but the model is capable of modeling all possible patterns.

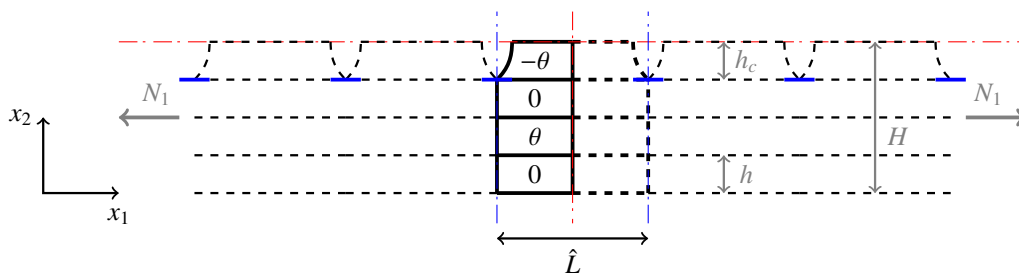


Figure 3: Lower half of the deformed laminate  $[0/\theta/0/-\theta_c]_s$  under a uni-axial tension load  $N_1$  illustrating the periodicity and symmetry lines. The horizontal red dashed line is a symmetry, whereas the vertical red and blue dashed lines are anti-symmetries.

### 3. Numerical Method

As discussed above, the problem can be modeled on a 2D plane, indicated by the gray dashed line in Fig. 2 and shown in detail in the  $(x_1, x_2)$ -plane in Fig. 4. This 2D problem is tackled with the off-axis finite element framework from Mikkelsen et al. (b), with which the 3D steady-state problem is projected onto a 2D plane and thus solved as a 2D model. This is achieved by using a specialized kinematic formulation, that leads to a modification of the strain-displacement matrix in the finite element code. This 2D technique was validated thoroughly against full 3D simulations in Mikkelsen et al. (b).

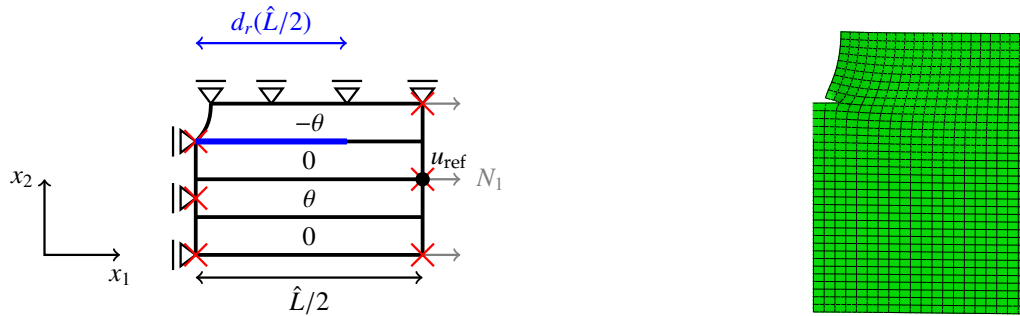


Figure 4: The deformed periodic model with boundary conditions exploiting the symmetries illustrated in figure 3. Left: The roller supports restrict the degrees of freedom in the  $x_1$  or  $x_2$  dimension, whereas the red crosses restrict the displacement in the  $x_3$  direction. The gray arrows indicate the prescribed axial load  $N_1$ . The delamination is marked in blue and is implemented disconnecting the mesh at the interface. Right: Illustration of the typical mesh with 720 quadratic quadrilateral elements in its deformed state. This is under the load  $N_1 = 10^5$  at an orientation  $\theta = 60^\circ$ , a crack density of  $\rho_c H = 1$  and a delamination ratio  $d_r = 0.1$  with the material GlassFRP.

Anti-symmetry of the problem is also exploited. Thus only a half period is modeled, as shown with the corresponding boundary conditions. The periodicity is enforced by anti-symmetry boundary conditions at each edge, i.e. restricting the out-of-plane displacement indicated by the red crosses and maintaining a straight edge. On the left edge, the straightness is ensured by the homogeneous Dirichlet boundary conditions, whereas the right edge uses multi-point constraints to ensure, that the displacement in the  $x_1$ -direction is aligned with the displacement of the reference node  $u_{\text{ref}}$ . The axial force  $N_1$  is then applied at the reference node. The validity of the boundary conditions has been verified via a comparison with a full model with 100 cracks.

In the finite element model, the delamination, which is shown in blue in Fig. 4 is implemented via a seam, which disconnects the meshes between the interfaces. The extend of the delamination is given by the dimensionless delamination ratio,  $d_r \in [0; 1[$ , such that  $d_r$  is zero for no delamination and unity for a full separation of the plies.

In the right part of Fig. 4 a typical mesh and solution of the model is shown. This specific mesh uses 720 quadratic quadrilateral elements leading to convergence errors smaller than 0.05%. A typical runtime for a case with 500-1000 elements lies at around 10-20 seconds for the model on a single node of an AMD EPYC 7351 (2.9 GHz) processor with 16 cores. The computational demand decreases significantly for smaller crack densities, i.e. larger crack spacing,  $L$ .

An implementation is available in a Python script<sup>1</sup>, that is to be run through Abaqus, and can represent any arbitrary laminate layup.

<sup>1</sup>It can be accessed under <https://github.com/Leon-Herrmann/Fracture-Modeling-with-OA2D>

#### 4. Validation

In this section different validation cases are presented. First it was ensured, that the numerical solution converges with a finer mesh refinement. Here a relative error of under 0.1% is realized at 100 elements for a model with the crack density  $\rho_c H = 1$ . Afterward the validity of the periodicity was investigated. Here, a model with an irregular crack distribution was analyzed to determine the sensitivity of the stiffness distribution with respect to the irregularity of the distribution. The sensitivity was very small and the irregularity is thereby deemed negligible and the idealization via a perfectly periodic model is appropriate.

Hereafter, the model is validated against several cases from literature. An overview is provided in Tab. 1, which contains semi-analytical, numerical, as well as experimental cases. All layups are symmetric and have cracks oriented in only a single direction. Note also, that the ply thickness information is in principle obsolete for this model. This is due to a geometrical non-dimensionalization. The crack density  $\rho_c$ , commonly expressed in cracks per mm will always be defined in combination with the total laminate height  $H$ , i.e. as  $\rho_c H$  in a non-dimensional form. The only exception is if the layer thicknesses vary, such as in the Katerelos et al. (b), Katerelos et al. (a) case, but typically this is handled in relative terms in the layup definition.

The axial stiffness per width in the  $x_1$ -direction,  $E_1$ , is extracted from the geometrical properties,  $H$  and  $\hat{L}$ , the prescribed displacement in the  $x_1$ -direction,  $u_1$ , and the applied load,  $N_1$ , as

$$E_1 = \frac{\sigma_1}{\epsilon_1} = \frac{N_1/H}{u_1/(\hat{L}/2)} = \frac{N_1/H}{u_1/(L/\sin(\theta)/2)} \quad (1)$$

The stiffness will be normalized by the initial value,  $E_1^0$ , i.e. of the undamaged laminate. This can either be estimated by classical laminate theory or the presented finite element model without defects. The estimates are equivalent apart from numerical errors. In this work the classical laminate theory estimate is used. Another important application of the classical laminate theory is estimation of a lower stiffness degradation bound. Here a modeling choice can be made. Either the damaged ply loses its entire stiffness or it only loses its local transverse and shear stiffness and retains its longitudinal stiffness along the tunneling crack direction. The second modeling choice, i.e. no degradation of the longitudinal stiffness, is closer to the proposed model. This will therefore be used as a limit case to and thus assessing the quality of the model. Henceforth it will be referred to as *the upper ply discount estimate*. The traditional approach of neglecting the entire stiffness of the ply leads to an even lower value, which can be considered as an ultimate bound, that is not to be breached by any simulation results. This does not occur for any of the analyzed layups, wherefore this bound is not discussed further.

The cases with tunneling cracks oriented at  $\theta = 90^\circ$ , i.e. Joffe and Varna and McCartney, are considered first. In the case of Joffe and Varna a comparison is made to values from experiments. For McCartney the comparison is made to an analytical approach, called the stress transfer model. Note that two different layups and material systems are used. The comparison is provided in Fig. 5, where a good agreement is observed for the experimental values and slight deviations occur for greater crack densities, especially for the stress transfer model. The errors are however below 0.04%. Furthermore, a convergence towards the

---

<sup>2</sup>The ply thickness information is found in Katerelos et al. (a).

Table 1: Five different validation cases with type, layup, material properties and ply thickness. Note that the subindex c in the layup definition indicates the ply containing the tunnelling crack.

Validation Case	Joffe and Varna	McCartney	Katerelos et al. (b)	Maragoni et al.	Barbero et al.
Type	Experimental	Analytical	Experimental	Numerical (3D)	Numerical (3D)
Layup	$[\pm\theta/90_{4c}]_s$	$[\pm 45/0/90_c]_s$	$[0/45_c]_s$	$[0/45_c]_s$ or $[0/45_c/-45]_s$	$[0/\theta_{4c}/-\theta_4/0]_s$
$E_L$ [GPa]	44.73	136.6	43.00	48.83	44.70
$E_T = E_{T'}$ [GPa]	12.76	9.790	13.00	14.07	12.70
$G_{LT} = G_{LT'}$ [GPa]	5.800	6.474	4.690	5.200	5.800
$G_{TT'}$ [GPa]	4.490	3.364	4.643	5.025	4.500
$\nu_{LT} = \nu_{LT'}$ [-]	0.2970	0.2860	0.3000	0.3080	0.2970
$\nu_{TT'}$ [-]	0.4200	0.4550	0.4000	0.4000	0.4111
Ply thickness [mm]	0.1440	0.1250	0.6100 in $45^\circ$ -ply <sup>2</sup> 0.6400 in $0^\circ$ -ply	0.6000	0.1440

upper ply discount estimate occurs for both cases.

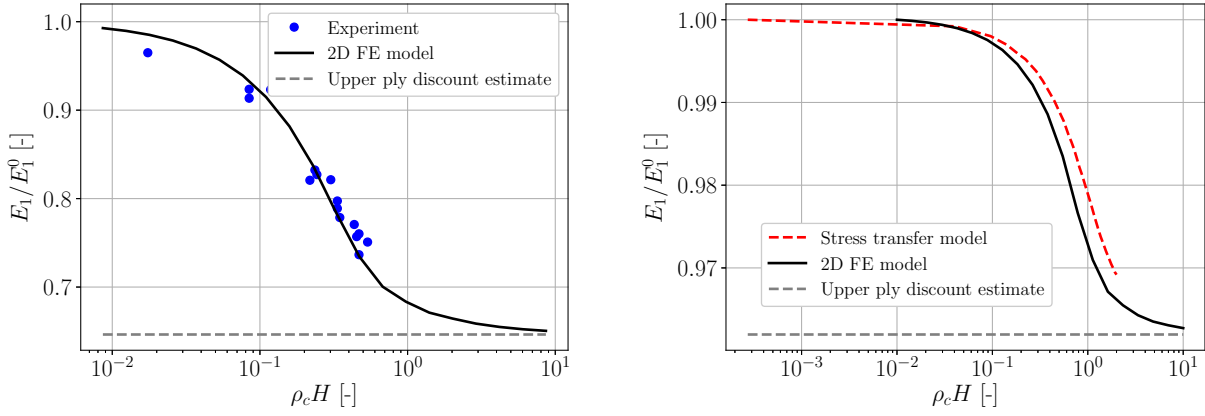


Figure 5: Comparison of periodic off-axis model to experimental and analytical values. Left: Comparison to experiment from Joffe and Varna using the layup  $[\pm\theta/90_{4c}]_s$ . Right: Comparison to analytical stress transfer model from McCartney using the layup  $[\pm 45/0/90_c]_s$ .

Secondly, the novel model presented here is applied to the case studied by Katerelos et al. (b) and Katerelos et al. (a), where an orientation of  $\theta = 45^\circ$  appears for the crack. Until now, this case has not been treatable with a 2D finite element model, unlike the previous two cases, which can be analyzed within generalized plane strain finite element models as the  $\theta = 45^\circ$  layer is undamaged. The  $\theta = 45^\circ$ -case traditionally requires 3D simulations. Thus, the  $\theta = 45^\circ$ -case is the first case, where the off-axis framework shows its benefit. A comparison with experimental values as well as 3D periodic finite element results from Maragoni et al. is shown in Fig. 6, where a good agreement is observed. Surprisingly, the two finite element models only show minor differences.

Thus, it is shown that the 2D framework can tackle unbalanced layups and represent the coupling effects. Once again a convergence towards the upper ply discount estimate is evident.

Due to the slight deviation with the 3D finite element model in the left part of Fig. 6, yet another comparison to Maragoni et al. is conducted and presented in the right part of Fig. 6. However, the layup is now  $[0/45_c/-45]_s$  and in this case a better agreement is reached.

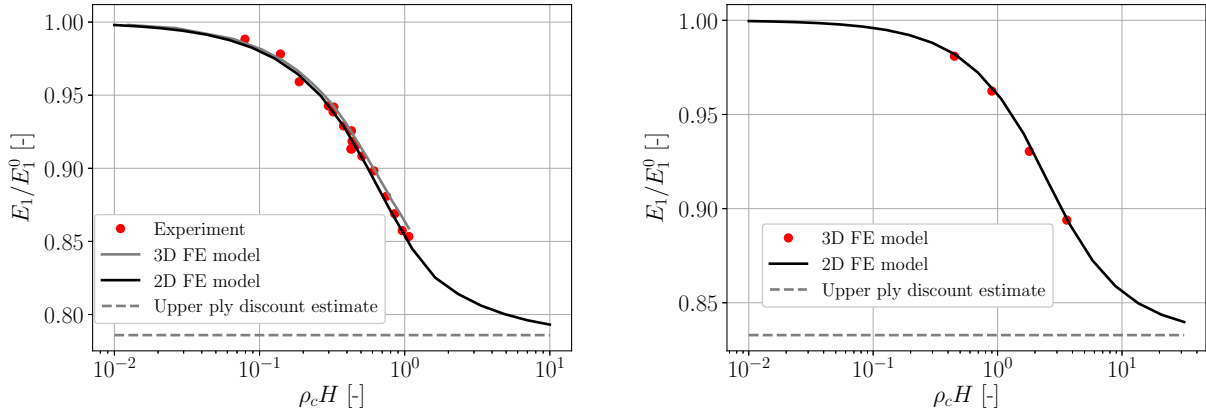


Figure 6: Comparison of model to experimental values and a 3D numerical model. Left: Comparison with experimental values from Katerelos et al. (b), Katerelos et al. (a) using the layup  $[0/45_c]_s$ . Additional comparison to results from a periodic 3D Finite element model by Maragoni et al. Right: Comparison with values obtained with a periodic 3D Finite element model by Maragoni et al. using the layup  $[0/45_c/-45]_s$ .

Finally, another 3D finite element model by Barbero et al. is used as a validation case, where a greater range of tunneling crack densities is explored reaching up to  $\rho_c H = 10^3$ . Both an orientation of  $\theta = 55^\circ$  and  $\theta = 70^\circ$  are investigated, as illustrated in Fig. 7. Again a good agreement and a convergence toward the upper ply discount are observed.

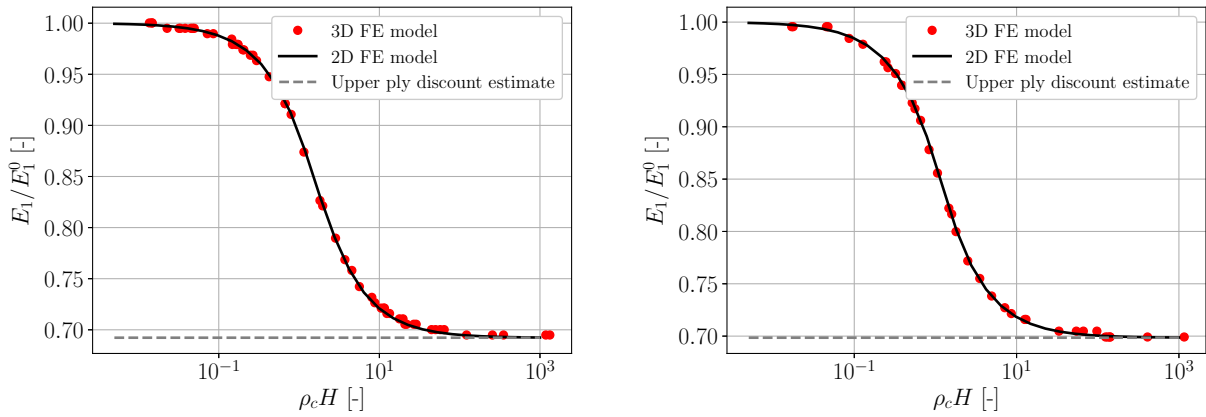


Figure 7: Comparison of model to values obtained with a periodic finite element mode by Barbero et al. using the layup  $[0/\theta_{4c}/-\theta_4/\bar{0}]_s$ . Left:  $\theta = 55^\circ$ . Right:  $\theta = 70^\circ$

Thus the method for the estimation of the axial stiffness degradation, due to the tunneling cracks is considered validated. Now, the delamination is included in the model, where the number of validation cases in the literature is sparse. Only one case with an orientation different from  $\theta = 90^\circ$  was identified, which is the case presented in Maragoni et al. with their 3D periodic finite element model. Here the layup  $[0/45_c/-45]_s$  is revisited, however with delamination cracks between the neighbouring interfaces of the

tunneling cracks, i.e. at  $[0/45_c]$ , and  $[45_c/-45]$ , see also Fig. 4. The results are presented in Fig. 8 for values delaminations given by  $d_r$ , where the red symbols are from the 3D finite element model by Maragoni et al. and the black lines from the present 2D off-axis finite element model. Once again, a good agreement is reached with errors lower than 0.2%, showing the validity of the novel 2D model.

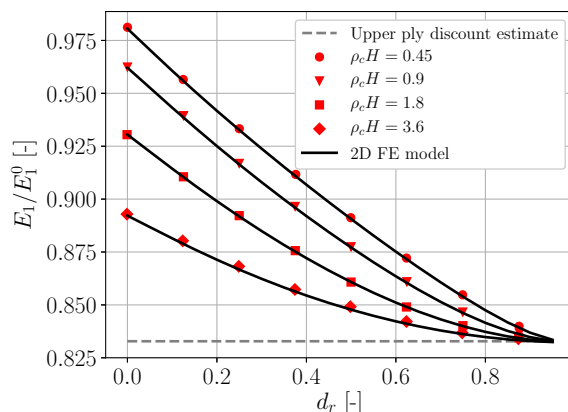


Figure 8: Comparison with values obtained with a periodic 3D Finite element by Maragoni et al. using the layup  $[0/45_c/-45]_s$ . The stiffness degradation as function of the delamination ratio.

As this is the only validation case concerning the delamination, a more in-depth comparison is performed. For this, the stresses presented in Maragoni et al. are considered. A satisfactory agreement is achieved with minor deviations at the crack tip. Thus the model is also considered validated with respect to the inclusion of delamination cracks.

## 5. Results

The model is now applied to the layup  $[0/\theta/0/-\theta_c]_s$  with the materials GlassFRP and CarbonFRP presented in Tab. 2, which is taken from Mikkelsen et al. (a), and Mikkelsen et al. (b). To showcase the capabilities of the developed model multiple parametric studies are conducted and presented.

Table 2: Material properties.

Material	$E_L$ [GPa]	$E_T = E_{T'}$ [GPa]	$G_{LT} = G_{LT'}$ [GPa]	$G_{TT}$ [GPa]	$\nu_{LT} = \nu_{LT'}$ [-]	$\nu_{TT}$ [-]
GlassFRP	30.62	8.620	3.250	2.900	0.2900	0.3300
CarbonFRP	266.0	5.490	3.540	2.370	0.2700	0.4000

First, similar to the validation cases for the stiffness degradation, caused by an increasing tunneling crack density is considered, see Fig. 9. Results for both GlassFRP and CarbonFRP are presented for three orientations  $\theta = 30^\circ$ ,  $\theta = 60^\circ$ , and  $\theta = 90^\circ$ . For both cases, a convergence toward the upper ply discount estimate exists, with slight errors in the GlassFRP case.

For GlassFRP the stiffness degradation is the least severe for  $\theta = 30^\circ$ , which might be expected, due to the local longitudinal stiffness not being affected as much for smaller angles. Surprisingly, the opposite

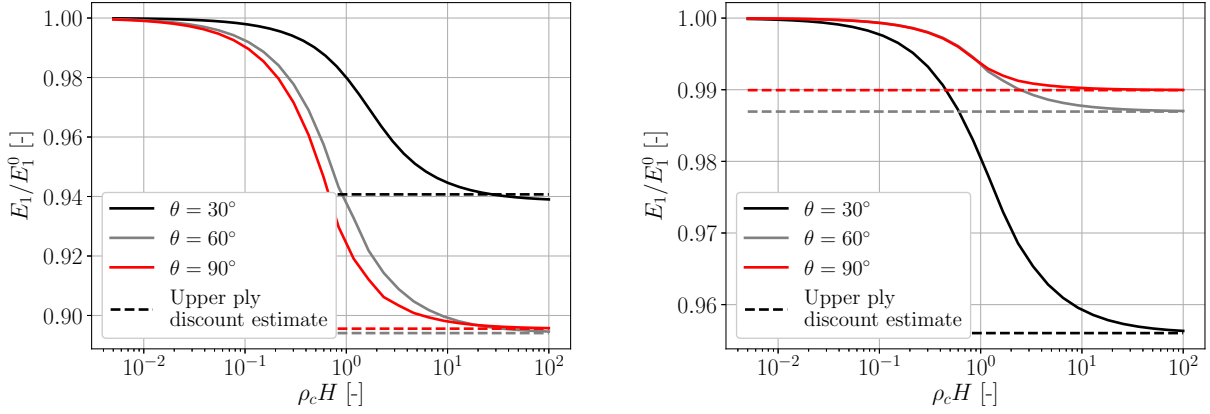


Figure 9: Influence of the tunnelling crack density  $\rho_c$  on the stiffness degradation for the layup  $[0/\theta/0/-\theta_c]_s$ . Left: GlassFRP. Right: CarbonFRP.

occurs for CarbonFRP, where the greatest stiffness degradation happens for  $\theta = 30^\circ$ . To explain, this phenomenon a parametric study with respect to the orientation  $\theta$  is performed, shown in figure 10. Here, it becomes clear, that the tendency of a lower stiffness degradation for very small angles holds true. However, for CarbonFRP, the maximal stiffness degradation is reached at about  $\theta = 30^\circ$ . This effect can probably be explained in part, by the ratio of the longitudinal stiffness and shear stiffness  $E_L/G_{LT}$ . A lower ratio moves the minimum to the right for CarbonFRP.

Additionally, the upper ply discount estimate captures the tendencies with respect to the orientation well, except for small angles. Especially in the case of GlassFRP, an underestimation of the degradation occurs for the upper ply discount estimate with a stiffness increase. This is an artifact of the method, where at small orientations, the lack of transverse and shear stiffness leads to an increase in longitudinal stiffness due to the Poisson effect. This spurious effect is however not captured by the 2D finite element model, which is preferable, as it most likely is not a physical effect. Furthermore, it is not very relevant, as laminates rarely use off-axis layers with such small orientations  $|\theta| < 10^\circ$ . If they were used, off-axis cracks would not even occur, due to the small energy release rates at these angles, as explored in Mikkelsen et al. (b).

Now, in addition to the tunneling cracks, delamination cracks are added. Yet again, the influence of the orientation  $\theta$  is investigated given different delamination ratios  $d_r$  and crack densities  $\rho_c$ . This is only performed for CarbonFRP and illustrated in figure 11, where a similar behavior as in figure 10 is observed. For a greater tunneling crack density, the differences between the different delamination ratios are smaller, as a lot of stiffness is already lost due to the tunneling cracks. Thus delamination can have a large impact on the stiffness for low crack densities.

Finally, the combined influence of the tunneling cracks and the delamination cracks is quantified. This is done in form of a contour plot, shown in figure 12 for GlassFRP. For this  $24 \times 24 = 576$  datapoints were created taking about 3 hours on one node of an AMD EPYC 7351 (2.9 GHz) processor with 16 cores.

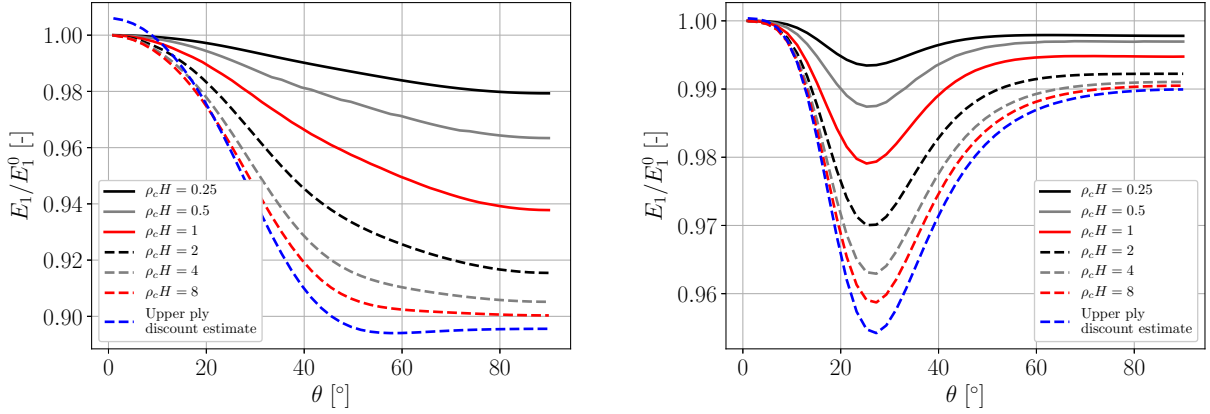


Figure 10: Influence of the orientation  $\theta$  on the axial stiffness degradation for the layup  $[0/\theta/0/-\theta_c]_s$ . Left: GlassFRP. Right: CarbonFRP.

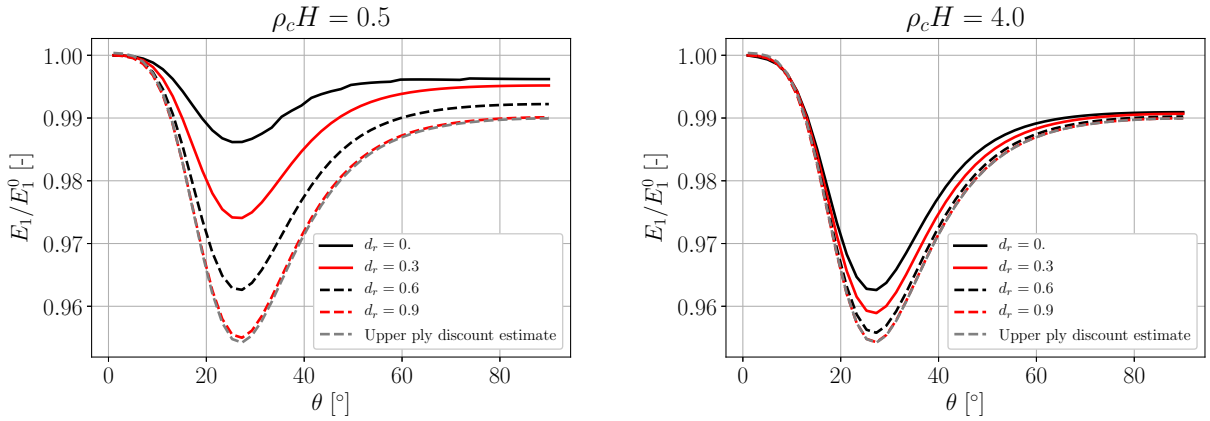


Figure 11: Influence of the orientation  $\theta$ , the tunneling crack density  $\rho_c$  and the delamination ratio  $d_r$  on the stiffness degradation for the layup  $[0/\theta/0/-\theta_c]_s$  with the material CarbonFRP.

The left part shows the results for the layup  $[0/30/0/-30_c]_s$ , whereas the right part shows them for the layup  $[90/60/90/-60_c]_s$ . In both cases, a slower decrease in stiffness is visible for damage with a final plateau corresponding to the upper ply discount estimate. The connection between the two layups is, that the second layup is simply the first layup rotated by  $90^\circ$ , as the layup  $[90/120/90/60_c]_s$  and the layup  $[90/60/90/-60_c]_s$  are equivalent. Thus, the axial stiffness degradation of the second layup is in fact the out-of-plane stiffness degradation of the first layup. This is useful in the context of monitoring structures. If the axial stiffness degradation and the tunneling crack density are known, the delamination ratio can be identified with the presented figures. Alternatively, if the axial and out-of-plane stiffness degradation are known, the two contour plots can be combined into one, as in figure 13. Thereby given two measurements both the tunneling crack density and the delamination ratio can be identified. To illustrate this consider a stiffness degradation measurement in the  $x_1$ -direction of 0.972, and in the  $x_3$ -direction of 0.875. Using Fig. 12, a tunneling crack density of  $\rho_c H = 0.16$  and a delamination ratio of  $d_r = 0.375$  can uniquely be identified.

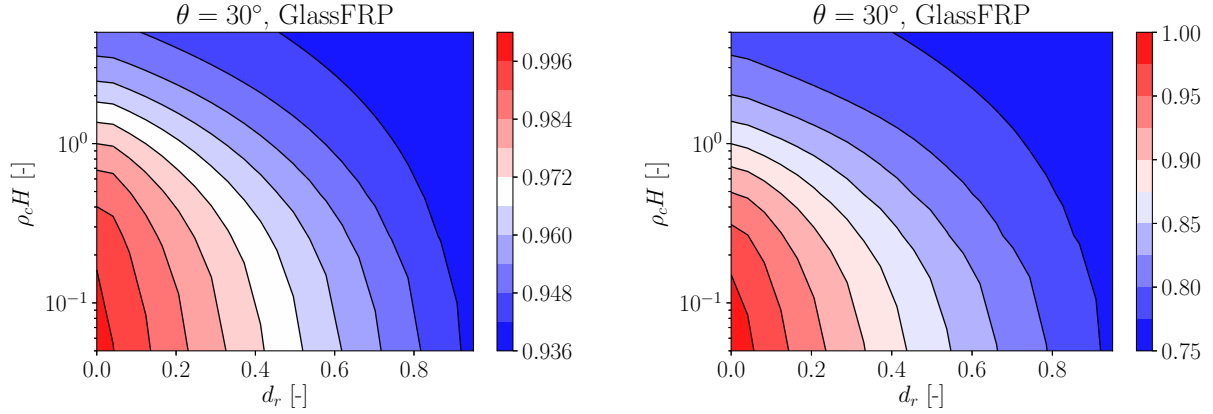


Figure 12: Influence of the tunneling crack density  $\rho_c$  and the delamination ratio  $d_r$  on the axial stiffness degradation for the rotated layup  $[90/\theta + 90/90/-\theta + 90_c]_s$ . Left: Non-rotated layup  $[0/30/0/-30_c]_s$  with GlassFRP Right: Rotated layup  $[90/60/90/-60_c]_s$  with GlassFRP.

## 6. Discussion

As previously mentioned, the one major limitation of the proposed model is, that it can only be applied to cases with cracks oriented in a single direction. This does however not always have to be a cause for concern, even though multiple orientations commonly occur in laminate structures. Because if the interaction between the cracks can be neglected, as is the case, if a large enough load-carrying layer is located in between, the degradations can be superposed, as discussed in Carraro and Quaresimin.

Another minor limitation is, that the tunneling cracks can only be taken into account, if they have tunneled through the entire laminate, and not only partly. Furthermore, edge effects can not be taken into account, which is however also not of interest, due to the width and length of the laminate being much greater than the height and are thereby negligible.

Apart from the mentioned limitations, the models' efficiency makes it very useful. For tunneling crack densities of about  $\rho_c H = 1$ , models with less than 1000 2D elements are sufficient for reasonable results. Thus single simulations take seconds and entire parametric studies take only minutes. The model becomes more expensive for lower tunneling crack densities, where the number of elements increases linearly. The delamination ratio does not impact the computational time.

Another restriction of the presented work is that only the axial stiffness degradation was presented. This is also the most important property when considering fiber-reinforced composites and was chosen to keep the model as simple as possible. The off-axis framework from Mikkelsen et al. (b) in combination with the presented periodic model is however fully capable of estimating all constitutive terms, where the in-plane quantities can be treated with the reaction force-based approach and the out-of-plane quantities require an integration over the corresponding stress fields.

## 7. Conclusion

A previously developed off-axis framework has been applied to the estimation of the axial stiffness degradation caused by tunneling and delamination cracks, commonly encountered in fiber-reinforced com-

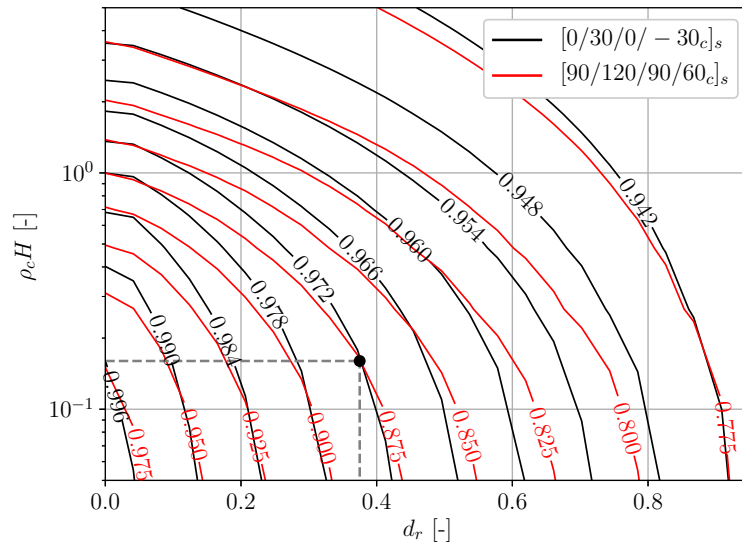


Figure 13: The axial stiffness degradation of the layup  $[0/30/0/-30_c]_s$  marked in black and of the layup  $[90/120/90/60_c]_s$ , equivalent to  $[90/60/90/-60_c]_s$  marked in red is shown.

posites. The result is a highly efficient periodic 2D finite element model, that estimates the stiffness in seconds. A good agreement with a variety of cases from literature has been shown as validation of the model. Furthermore, multiple parametric studies were performed to showcase the capabilities of the model, which are useful during the design process to avoid problematic stiffness degradations. But they are also useful during monitoring of structures, where the progression of the internal damage can be assessed via the stiffness degradation. Only the axial stiffness degradation was discussed and presented, but the model is fully capable of handling all constitutive terms. A Python implementation of the model, that is to be run through Abaqus and can represent any arbitrary layup with cracks oriented in one direction, is also available.

## References

- E. J. Barbero, F. A. Cosso, and F. A. Campo. Benchmark solution for degradation of elastic properties due to transverse matrix cracking in laminated composites. 98:242–252. ISSN 02638223. doi: 10.1016/j.compstruct.2012.11.009. URL <https://linkinghub.elsevier.com/retrieve/pii/S0263822312005612>.
- P. A. Carraro and M. Quaresimin. A stiffness degradation model for cracked multidirectional laminates with cracks in multiple layers. 58:34–51. ISSN 00207683. doi: 10.1016/j.ijsolstr.2014.12.016. URL <https://linkinghub.elsevier.com/retrieve/pii/S0020768314004843>.
- P. A. Carraro, L. Maragoni, and M. Quaresimin. Characterisation and analysis of transverse crack-induced delamination in cross-ply composite laminates under fatigue loadings. 129:105217. ISSN 01421123. doi: 10.1016/j.jfatigue.2019.105217. URL <https://linkinghub.elsevier.com/retrieve/pii/S0142112319303214>.
- F. Crossman and A. Wang. The dependence of transverse cracking and delamination on ply thickness in graphite/epoxy laminates. In K. Reifsnider, editor, *Damage in Composite Materials: Basic Mechanisms, Accumulation, Tolerance, and Characterization*, pages 118–118–22. ASTM International. ISBN 9780803106963. doi: 10.1520/STP34324S. URL <http://www.astm.org/doiLink.cgi?STP34324S>.
- K. M. Jespersen. Fatigue damage evolution in fibre composites for wind turbine blades.
- K. M. Jespersen, J. Zangenberg, T. Lowe, P. J. Withers, and L. P. Mikkelsen. Fatigue damage assessment of uni-directional non-crimp

- fabric reinforced polyester composite using x-ray computed tomography. 136:94–103. ISSN 02663538. doi: 10.1016/j.compscitech.2016.10.006. URL <https://linkinghub.elsevier.com/retrieve/pii/S0266353816314130>.
- R. Joffe and J. Varna. Analytical modeling of stiffness reduction in symmetric and balanced laminates due to cracks in 90° layers. 59(11):1641–1652. ISSN 02663538. doi: 10.1016/S0266-3538(99)00025-1. URL <https://linkinghub.elsevier.com/retrieve/pii/S0266353899000251>.
- D. T. G. Katerelos, M. Kashtalyan, C. Soutis, and C. Galiotis. Matrix cracking in polymeric composites laminates: Modelling and experiments. 68(12):2310–2317, a. ISSN 02663538. doi: 10.1016/j.compscitech.2007.09.013. URL <https://linkinghub.elsevier.com/retrieve/pii/S0266353807003661>.
- D. T. G. Katerelos, L. N. McCartney, and C. Galiotis. Effect of off – axis matrix cracking on stiffness of symmetric angle-ply composite laminates. 139(3):529–536, b. ISSN 0376-9429, 1573-2673. doi: 10.1007/s10704-006-0100-9. URL <http://link.springer.com/10.1007/s10704-006-0100-9>.
- L. Maragoni, P. A. Carraro, and M. Quaresimin. Periodic boundary conditions for FE analyses of a representative volume element for composite laminates with one cracked ply and delaminations. 201:932–941. ISSN 02638223. doi: 10.1016/j.compstruct.2018.06.058. URL <https://linkinghub.elsevier.com/retrieve/pii/S0263822317339727>.
- L. N. McCartney. Stress transfer mechanics for ply cracks in general symmetric laminates.
- L. P. Mikkelsen, S. J. Klitgaard, C. F. Niordson, and B. F. Sørensen. Tunneling cracks in arbitrary oriented off-axis lamina. 226(2):161–179, a. ISSN 0376-9429, 1573-2673. doi: 10.1007/s10704-020-00485-9. URL <http://link.springer.com/10.1007/s10704-020-00485-9>.
- L. P. Mikkelsen, B. N. Legarth, L. Herrmann, M. M. Christensen, and F. N. Niordson. A special finite element method applied to off-axis tunnel cracking in laminates. b.
- J. Zhang and K. P. Herrmann. Stiffness degradation induced by multilayer intralaminar cracking in composite laminates. 30(5): 683–706. ISSN 1359835X. doi: 10.1016/S1359-835X(98)00106-7. URL <https://linkinghub.elsevier.com/retrieve/pii/S1359835X98001067>.

# List of Symbols

$0$	Superscript indicating the undamaged structure 5, 9, 10, 13, 20, 39, 44–46, 61, 62
$A$	Crack surface area 7, 43, 45, 62
$a$	Crack length 8, 13, 39–41
$\mathbf{A}$	Extensional stiffness matrix 19, 20
$\mathbf{B}$	Extension-bending coupling matrix 19
$\mathbf{C}$	Compliance matrix 22
$c$	Subscript indicating a cracked ply 3, 11, 16–18, 22–25, 27–31, 33–38, 43, 49–58, 63–68, 70, 71
$D$	Damage parameter 22
$\mathbf{D}$	Bending stiffness matrix 19
$dc$	Subscript to indicate delamination crack 46, 47
DCGR	Delamination crack growth rate 47, 57
$d_r$	Delamination ratio 32, 33, 35–38, 47, 51, 53, 54, 56, 58, 64, 66
$E$	Young's modulus 5, 8, 16, 19, 20, 22, 25, 33, 50, 63, 68
$E_1$	Axial stiffness 15, 20, 22–24, 33, 34, 43, 44, 47, 105
$\hat{E}_1$	Converged axial stiffness 23, 33
$F$	Reaction force at an interface 39–41, 45, 46, 61
$\mathbf{F}$	Force vector 61, 62
$f$	Internal nodal force 40
$f$	Subscript to indicate fiber 63
$G$	Shear modulus 16, 19, 22, 25, 50, 63, 68

$\mathcal{G}$	Energy release rate 7–9, 15, 39, 42–44, 46, 47, 52, 54–57, 61, 65–68
$\mathcal{G}_I$	Mode I energy release rate 7–9, 13, 39, 40, 45, 50, 51, 53, 54, 62, 68
$\mathcal{G}_{II}$	Mode II energy release rate 8, 9, 40, 45, 51, 54, 55, 62, 68
$\mathcal{G}_{III}$	Mode III energy release rate 40, 54, 55, 62, 68
$\mathcal{G}_{ss}$	Steady state energy release rate 9, 44–46, 62
$H$	Half height of the symmetric laminate 18, 23, 25, 26, 29, 33, 34, 36, 43, 49–51, 55–57, 64
$h$	Ply height 9, 17–19, 33, 35, 45, 57
$h_c$	Half crack height 18, 43, 66
$h_\theta$	Ply thickness in the off-axis layers 37, 38, 56, 57
$L$	Normal distance between periodic tunneling cracks 17, 18, 29
$\hat{L}$	Projection of normal distance between periodic tunneling cracks on $x_1$ 17, 18, 20, 32, 43
$l_c$	Crack length 62, 66, 68
$M$	Bending moment 4
$\mathbf{M}$	Bending moment vector 19
$m$	Subscript to indicate matrix 63
$N$	Normal force 4, 18–22, 26, 35, 43, 44, 78–80, 105
$N$	Number of cycles 8
$\bar{\mathbf{N}}$	Total far field force vector 20, 21
$\mathbf{N}$	Normal force vector 19, 20, 22
$\mathbf{n}$	Normal direction vector 61, 62
$n_{EI}$	Smallest element length 23, 33, 49

<b>Q</b>	Constitutive matrix 19, 22
<b>r</b>	Off-axis direction vector 61, 62
$r_0$	Fiber radius 64
<b>s</b>	Subscript to indicate symmetric layup 11, 16–18, 23–31, 33–38, 43, 49–58, 63–68, 70, 71
<b>T</b>	Transformation matrix 19, 20
<b>t</b>	Transverse direction vector 61, 62
<b>tc</b>	Subscript to indicate tunneling crack 46, 47
<b>TCGR</b>	Tunnel crack growth rate 47, 57
$U$	Internal energy 42, 43, 78, 79
<b>u</b>	Displacement vector 61, 62
$u$	Displacement 21, 24, 40
$W$	External work 42, 43, 78, 79
$w$	Laminate width 47, 57
<b>x</b>	Nodal position vector 61
$x_1$	Global coordinate 3, 4, 13, 17–22, 32, 36, 37, 39, 40, 64, 86
$x_2$	Global coordinate 3, 4, 9, 17, 19, 20, 22, 32, 64, 75
$x_3$	Global coordinate 3, 4, 17–20, 24, 32, 36, 37
$x_L$	Longitudinal coordinate 3
$x_T$	Out-of-plane transverse coordinate 3
$x_{T'}$	In-plane transverse coordinate 3
$\Delta$	Displacement at undamaged boundary 18–20, 43, 44, 78–80, 105
$\Delta a$	Crack extension length 7, 13, 39–41, 47, 49

$\Delta E_1$	Relative axial stiffness degradation 20, 29, 63–65
$\Delta u$	Crack opening displacement 9, 10, 13, 39, 40, 44–46, 61, 70
$\Pi$	Potential energy 7, 13, 42, 43, 45, 62, 79, 80
$\bar{\varepsilon}$	Far field strain vector 20
$\varepsilon$	Strain vector 19, 22
$\varepsilon$	Strain 4, 19, 20, 22, 44, 74, 105
$\zeta$	Halpin-Tsai shape parameter 63
$\eta$	Halpin-Tsai material parameter 63
$\theta$	Ply orientation 3, 4, 16–18, 20, 22–26, 28–31, 34–38, 43, 45, 47, 53–57, 60–71
$\kappa$	Curvature vector 19
$\kappa$	Curvature 4
$\nu$	Poisson's ratio 16, 19, 20, 22, 25, 50, 63, 68
$\rho_c$	Tunneling crack density 17, 23, 25–27, 29–31, 33–38, 42–44, 46, 47, 50, 51, 53, 55–57, 64, 105
$\sigma$	Stress vector 22
$\sigma$	Stress 9, 10, 13, 15, 26, 35, 39, 44–46, 70, 86, 105
$\varphi$	Fiber density 63–67

# List of Figures

Figure 1	A generic laminate introducing the notation.....	4
Figure 2	Effect of the three damage stages on the stiffness. ....	5
Figure 3	The three damage mechanisms in fiber reinforced composites under tension. ....	6
Figure 4	The three fracture modes.....	7
Figure 5	The linear correlation of the crack growth rate $da/dN$ and the range of the stress intensity factor $\Delta K$ in a log-log plot. ....	8
Figure 6	The fiber-matrix microstructures. ....	10
Figure 7	Delamination configurations. ....	12
Figure 8	Schematic illustrating the crack closure integral and virtual crack closure technique. ....	13
Figure 9	Top view of the laminate illustrating the periodicity.....	18
Figure 10	Lower half of the deformed laminate under uni-axial tension.....	18
Figure 11	The deformed periodic model with tunneling cracks.....	19
Figure 12	Convergence study with respect to the axial stiffness with tunneling cracks.....	23
Figure 13	Comparison of the displacements in a unbalanced laminate between the full and periodic model.....	24
Figure 14	Comparison of the axial stiffness in an unbalanced laminate between the full and periodic model.....	24
Figure 15	Validation case with classical laminate theory.....	26
Figure 16	Stiffness degradation validation case with crack orientated at $90^\circ$ from [JV99] and [McC96].....	27
Figure 17	Stiffness degradation validation case from [KMG06], [Kat+08].....	27
Figure 18	Stiffness degradation validation case from [MCQ18].....	28
Figure 19	Stiffness degradation validation case from [BCC13].....	28
Figure 20	Stochastic Investigation of the effect of irregularly spaced tunneling cracks on the stiffness degradation.....	29
Figure 21	Example tunneling crack distribution.....	29
Figure 22	Influence of the orientation on the axial stiffness degradation.....	30
Figure 23	Influence of the orientation on the axial stiffness degradation using the layup from [BCC13].....	31

Figure 24	Influence of the tunneling crack density on the stiffness degradation.....	31
Figure 25	The deformed periodic model with tunneling and delamination cracks.....	32
Figure 26	Example of two isotropic layers with delamination leading to overlap at the interface.....	33
Figure 27	Convergence study with respect to the axial stiffness with tunneling and delamination cracks.....	34
Figure 28	Comparison with the local transverse stresses from [MCQ18].....	35
Figure 29	Comparison with the stiffness degradation caused by delamination from [MCQ18]	35
Figure 30	Influence of the tunneling crack density and the delamination ratio on the axial stiffness.....	36
Figure 31	Influence of the tunneling crack density and the delamination ratio on the axial stiffness using a laminate rotated by $90^\circ$ . ....	37
Figure 32	The stiffness degradation in the axial direction and out-of-plane direction to estimate the internal damage.....	37
Figure 33	Influence of the orientation on the axial stiffness in the presence of tunneling cracks and delamination. ....	38
Figure 34	Influence of the off-axis layer thickness on the axial stiffness in the presence of tunneling cracks and delamination.....	38
Figure 35	Schematic illustrating the virtual crack closure technique for elements with quadratic shape functions. ....	40
Figure 36	Schematic of the reaction force extraction method via multi-point constraints.....	41
Figure 37	Periodic tunnel cracking cracking problem. ....	42
Figure 38	Force-displacement curve showing the change in potential energy for load-control in gray and for displacement control in red. ....	43
Figure 39	Transformation of the stiffness $E_1 = \sigma_{11}/\varepsilon_{11}$ to the compliance $C = \Delta_1/N_1$ . ....	44
Figure 40	Energy release rate for the doubling of the tunnel cracking density, given the current density $\rho_c$ obtained with the compliance method. ....	44
Figure 41	Two periodic tunnel cracking models for the computation of the energy release rate of cracks between other cracks.....	46
Figure 42	Top view of the laminate showing the sequential cracking.....	46
Figure 43	Convergence study with respect to the energy release rate during delamination.....	49

Figure 44	Convergence study with respect to the mode I energy release rate during delamination. ....	50
Figure 45	Delamination energy release rate validation case from [CMQ19]. ....	51
Figure 46	Delamination energy release rate validation case from [MCQ18] ....	52
Figure 47	Influence of the delamination ratio on the delamination energy release rate. ....	54
Figure 48	Influence of the orientation on the delamination energy release rate.....	55
Figure 49	Influence of the orientation and the tunneling crack density on the tunnel crack- ing energy release rate. ....	56
Figure 50	Influence of the delamination ratio on the energy release rate.....	56
Figure 51	Influence of the off-axis layer height on the tunneling crack energy release rate. ...	57
Figure 52	Determination of the point of delamination.....	58
Figure 53	Stiffness degradation with respect to the number of cycles. ....	58
Figure 54	Fiber-matrix microstructure model. ....	60
Figure 55	Projection of nodal quantities onto the surface normal. ....	61
Figure 56	Influence of the fiber-matrix microstructure on the stiffness degradation. ....	64
Figure 57	Influence of the fiber radius on the stiffness degradation.....	65
Figure 58	Influence of the fiber-matrix microstructure on the delamination energy release rate. ....	66
Figure 59	Model of a simple non-straight crack. ....	67
Figure 60	Influence of the eccentricity of a non-straight crack on the tunnel cracking en- ergy release rate. ....	67
Figure 61	Contour plot illustrating the mode III energy release rate.....	68
Figure 62	The crack length as function of the eccentricity.....	68
Figure 63	Contourplot of the non-straight crack embedded in a fiber-matrix microstructure. .	70
Figure 64	Comparison of straight and non-straight crack profiles.....	71
Figure 65	Toy-example illustrating the differences during the computation of the energy release rate for load-control and displacement control.....	78
Figure 66	Program structure.....	81
Figure 67	Model Description of the model defined in <code>BuildLaminateModel</code> .....	84
Figure 68	Model produced by example configuration file.....	86

# List of Tables

Table 1	Material properties. ....	16
Table 2	Validation cases for the stiffness degradation. ....	25
Table 3	Validation cases for the delamination crack propagation. ....	50
Table 4	Fiber and matrix material properties I. ....	64
Table 5	Fiber and matrix material properties II. ....	67
Table 6	Homogenized material properties. ....	68
Table 7	Energy release rate of a non-straight crack in an irregular fiber-matrix microstructure. ....	69
Table 8	Energy release rate of a non-straight crack in an irregular fiber-matrix microstructure without projection. ....	70

# Bibliography

- [And17] T. L. Anderson. *Fracture Mechanics: Fundamentals and Applications*. 3rd ed. CRC Press, Mar. 3, 2017. ISBN: 9781315370293. DOI: [10.1201/9781315370293](https://doi.org/10.1201/9781315370293).
- [Bak+14] B. L. V. Bak, C. Sarrado, A. Turon, and J. Costa. “Delamination Under Fatigue Loads in Composite Laminates: A Review on the Observed Phenomenology and Computational Methods”. In: *Applied Mechanics Reviews* 66.6 (Nov. 1, 2014), p. 060803. ISSN: 0003-6900, 2379-0407. DOI: [10.1115/1.4027647](https://doi.org/10.1115/1.4027647).
- [Bao+92] G. Bao, S. Ho, Z. Suo, and B. Fan. “The role of material orthotropy in fracture specimens for composites”. In: *International Journal of Solids and Structures* 29.9 (1992), pp. 1105–1116. ISSN: 00207683. DOI: [10.1016/0020-7683\(92\)90138-J](https://doi.org/10.1016/0020-7683(92)90138-J).
- [Bar74] R. S. Barsoum. “Application of quadratic isoparametric finite elements in linear fracture mechanics”. In: *International Journal of Fracture* 10.4 (Dec. 1, 1974), pp. 603–605. ISSN: 1573-2673. DOI: [10.1007/BF00155266](https://doi.org/10.1007/BF00155266).
- [BCC13] E. J. Barbero, F. A. Cosso, and F. A. Campo. “Benchmark solution for degradation of elastic properties due to transverse matrix cracking in laminated composites”. In: *Composite Structures* 98 (Apr. 2013), pp. 242–252. ISSN: 02638223. DOI: [10.1016/j.compstruct.2012.11.009](https://doi.org/10.1016/j.compstruct.2012.11.009).
- [Bel+14] T. Belytschko, W. K. Liu, B. Moran, and K. I. Elkhodary. *Nonlinear finite elements for continua and structures*. Second edition. Chichester, West Sussex, United Kingdom: Wiley, 2014. 804 pp. ISBN: 9781118632703.
- [Beu92] J. L. Beuth. “Cracking of thin bonded films in residual tension”. In: *International Journal of Solids and Structures* 29.13 (1992), pp. 1657–1675. ISSN: 00207683. DOI: [10.1016/0020-7683\(92\)90015-L](https://doi.org/10.1016/0020-7683(92)90015-L).
- [BZC13] H. G. Beom, X. R. Zhuo, and C. B. Cui. “Tunneling cracks in the adhesive layer of an orthotropic sandwich structure”. In: *International Journal of Engineering Science* 63 (Feb. 2013), pp. 40–51. ISSN: 00207225. DOI: [10.1016/j.ijengsci.2012.11.001](https://doi.org/10.1016/j.ijengsci.2012.11.001).
- [CMQ17] P. A. Carraro, L. Maragoni, and M. Quaresimin. “Prediction of the crack density evolution in multidirectional laminates under fatigue loadings”. In: *Composites Science and Technology* 145 (June 2017), pp. 24–39. ISSN: 02663538. DOI: [10.1016/j.compscitech.2017.03.013](https://doi.org/10.1016/j.compscitech.2017.03.013).
- [CMQ19] P. A. Carraro, L. Maragoni, and M. Quaresimin. “Characterisation and analysis of transverse crack-induced delamination in cross-ply composite laminates under fatigue loadings”. In: *International Journal of Fatigue* 129 (Dec. 2019), p. 105217. ISSN: 01421123. DOI: [10.1016/j.ijfatigue.2019.105217](https://doi.org/10.1016/j.ijfatigue.2019.105217).

- [CMQ21] P. A. Carraro, L. Maragoni, and M. Quaresimin. “Stiffness degradation of symmetric laminates with off-axis cracks and delamination: an analytical model”. In: *International Journal of Solids and Structures* 213 (Mar. 2021), pp. 50–62. ISSN: 00207683. DOI: [10.1016/j.ijsolstr.2020.12.013](https://doi.org/10.1016/j.ijsolstr.2020.12.013).
- [Coo01] R. D. Cook, ed. *Concepts and applications of finite element analysis*. 4th ed. New York, NY: Wiley, 2001. 719 pp. ISBN: 9780471356059.
- [CQ15] P. A. Carraro and M. Quaresimin. “A stiffness degradation model for cracked multidirectional laminates with cracks in multiple layers”. In: *International Journal of Solids and Structures* 58 (Apr. 2015), pp. 34–51. ISSN: 00207683. DOI: [10.1016/j.ijsolstr.2014.12.016](https://doi.org/10.1016/j.ijsolstr.2014.12.016).
- [CR15] William D. Callister and David G. Rethwisch. *Materials science and engineering*. 9. ed., SI version. Hoboken, NJ: Wiley, 2015. 905 pp. ISBN: 9781118319222.
- [CW82] Fw Crossman and Asd Wang. “The Dependence of Transverse Cracking and Delamination on Ply Thickness in Graphite/Epoxy Laminates”. In: *Damage in Composite Materials: Basic Mechanisms, Accumulation, Tolerance, and Characterization*. Ed. by KI Reifsnider. 100 Barr Harbor Drive, PO Box C700, West Conshohocken, PA 19428-2959: ASTM International, Jan. 1, 1982, pp. 118–118–22. ISBN: 9780803106963. DOI: [10.1520/STP34324S](https://doi.org/10.1520/STP34324S).
- [DI94] Isaac M. Daniel and Ori Ishai. *Engineering mechanics of composite materials*. New York: Oxford University Press, 1994. 395 pp. ISBN: 9780195075069.
- [DS91] A. Dollar and P. S. Steif. “The Branched Crack Problem Revisited”. In: *Journal of Applied Mechanics* 58.2 (June 1, 1991), pp. 584–586. ISSN: 0021-8936, 1528-9036. DOI: [10.1115/1.2897227](https://doi.org/10.1115/1.2897227).
- [Fei05] S. Feih. “Development of a user element in ABAQUS for modelling of cohesive laws in composite structures”. In: *Technical Report, Risø DTU-National Laboratory for Sustainable Energy* (2005).
- [FT05] R. Fosdick and L. Truskinovsky. “About Clapeyron’s Theorem in Linear Elasticity”. In: *The Rational Spirit in Modern Continuum Mechanics*. Ed. by C. Man and R. L. Fosdick. Dordrecht: Kluwer Academic Publishers, 2005, pp. 399–426. ISBN: 9781402018282. DOI: [10.1007/1-4020-2308-1\\_24](https://doi.org/10.1007/1-4020-2308-1_24).
- [Gri21] A. A. Griffith. “The Phenomena of Rupture and Flow in Solids”. In: *Philosophical Transactions of the Royal Society of London. Series A, Containing Papers of a Mathematical or Physical Character* 221 (1921), pp. 163–198. ISSN: 0264-3952.
- [GS18] D. Gross and T. Seelig. *Fracture Mechanics: With an Introduction to Micromechanics*. Mechanical Engineering Series. Cham: Springer International Publishing, 2018. ISBN: 9783319710891 9783319710907. DOI: [10.1007/978-3-319-71090-7](https://doi.org/10.1007/978-3-319-71090-7).

- [GS99] E. K. Gamstedt and B. A. Sjögren. “Micromechanisms in tension-compression fatigue of composite laminates containing transverse plies”. In: *Composites Science and Technology* 59.2 (Feb. 1999), pp. 167–178. ISSN: 02663538. DOI: [10.1016/S0266-3538\(98\)00061-X](https://doi.org/10.1016/S0266-3538(98)00061-X).
- [Her+21a] L. Herrmann, L. P. Mikkelsen, B. N. Legarth, F. Duddeck, and C. F. Niordson. “An efficient stiffness degradation model for layered composites with arbitrarily oriented tunneling and delamination cracks”. In: *in preparation* (2021).
- [Her+21b] L. Herrmann, L. P. Mikkelsen, B. N. Legarth, and C. F. Niordson. “The influence of the fiber-matrix microstructure on off-axis tunnel cracking in laminates”. In: *in preparation* (2021).
- [HS91] J. W. Hutchinson and Z. Suo. “Mixed Mode Cracking in Layered Materials”. In: *Advances in Applied Mechanics*. Vol. 29. Elsevier, 1991, pp. 63–191. ISBN: 9780120020294. DOI: [10.1016/S0065-2156\(08\)70164-9](https://doi.org/10.1016/S0065-2156(08)70164-9).
- [HS93] S. Ho and Z. Suo. “Tunneling Cracks in Constrained Layers”. In: *Journal of Applied Mechanics* 60.4 (Dec. 1, 1993), pp. 890–894. ISSN: 0021-8936, 1528-9036. DOI: [10.1115/1.2900998](https://doi.org/10.1115/1.2900998).
- [Irw56] G. R. Irwin. *Onset of fast crack propagation in high strength steel and aluminium alloys*. Fort Belvoir, VA: Defense Technical Information Center, May 24, 1956. DOI: [10.21236/AD0099305](https://doi.org/10.21236/AD0099305).
- [Jes+16] K. M. Jespersen, J. Zangenberg, T. Lowe, P. J. Withers, and L. P. Mikkelsen. “Fatigue damage assessment of uni-directional non-crimp fabric reinforced polyester composite using X-ray computed tomography”. In: *Composites Science and Technology* 136 (Nov. 2016), pp. 94–103. ISSN: 02663538. DOI: [10.1016/j.compscitech.2016.10.006](https://doi.org/10.1016/j.compscitech.2016.10.006).
- [Jes17] K. M. Jespersen. “Fatigue damage evolution in fibre composites for wind turbine blades”. PhD thesis. Risø Campus, Denmark: DTU Wind Energy, 2017.
- [JM17] K. M. Jespersen and L. P. Mikkelsen. “Three dimensional fatigue damage evolution in non-crimp glass fibre fabric based composites used for wind turbine blades”. In: *Composites Science and Technology* 153 (Dec. 2017), pp. 261–272. ISSN: 02663538. DOI: [10.1016/j.compscitech.2017.10.004](https://doi.org/10.1016/j.compscitech.2017.10.004).
- [Jør17] J. B. Jørgensen. “Adhesive joints in wind turbine blades”. PhD thesis. DTU Wind Energy, 2017.
- [JSK18] J. B. Jørgensen, B. F. Sørensen, and C. Kildegaard. “Tunneling cracks in full scale wind turbine blade joints”. In: *Engineering Fracture Mechanics* 189 (Feb. 2018), pp. 361–376. ISSN: 00137944. DOI: [10.1016/j.engfracmech.2017.11.016](https://doi.org/10.1016/j.engfracmech.2017.11.016).
- [JV99] R. Joffe and J. Varna. “Analytical modeling of stiffness reduction in symmetric and balanced laminates due to cracks in 90° layers”. In: *Composites Science and Technology* 59.11 (Aug. 1999), pp. 1641–1652. ISSN: 02663538. DOI: [10.1016/S0266-3538\(99\)00025-1](https://doi.org/10.1016/S0266-3538(99)00025-1).

- [Kat+08] D. T. G. Katerelos, M. Kashtalyan, C. Soutis, and C. Galiotis. “Matrix cracking in polymeric composites laminates: Modelling and experiments”. In: *Composites Science and Technology* 68.12 (Sept. 2008), pp. 2310–2317. ISSN: 02663538. DOI: [10.1016/j.compscitech.2007.09.013](https://doi.org/10.1016/j.compscitech.2007.09.013).
- [KMG06] D. T. G. Katerelos, L. N. McCartney, and C. Galiotis. “Effect of Off – Axis Matrix Cracking on Stiffness of Symmetric Angle-Ply Composite Laminates”. In: *International Journal of Fracture* 139.3 (June 2006), pp. 529–536. ISSN: 0376-9429, 1573-2673. DOI: [10.1007/s10704-006-0100-9](https://doi.org/10.1007/s10704-006-0100-9).
- [Kru04] R. Krueger. “Virtual crack closure technique: History, approach, and applications”. In: *Applied Mechanics Reviews* 57.2 (Mar. 1, 2004), pp. 109–143. ISSN: 0003-6900, 2379-0407. DOI: [10.1115/1.1595677](https://doi.org/10.1115/1.1595677).
- [LD10] J. Lemaître and R. Desmorat. *Engineering damage mechanics: ductile, creep, fatigue and brittle failures*. OCLC: 804771444. Berlin: Springer, 2010. ISBN: 9783642059988.
- [Lem96] J. Lemaître. *A course on damage mechanics*. 2nd rev. and enl. ed. Berlin ; New York: Springer, 1996. 228 pp. ISBN: 9783540609803.
- [Li08] S. Li. “Boundary conditions for unit cells from periodic microstructures and their implications”. In: *Composites Science and Technology* 68.9 (July 2008), pp. 1962–1974. ISSN: 02663538. DOI: [10.1016/j.compscitech.2007.03.035](https://doi.org/10.1016/j.compscitech.2007.03.035).
- [LST09] S. Li, C. V. Singh, and R. Talreja. “A representative volume element based on translational symmetries for FE analysis of cracked laminates with two arrays of cracks”. In: *International Journal of Solids and Structures* 46.7 (Apr. 2009), pp. 1793–1804. ISSN: 00207683. DOI: [10.1016/j.ijsolstr.2009.01.009](https://doi.org/10.1016/j.ijsolstr.2009.01.009).
- [LV05] P. Lundmark and J. Varna. “Constitutive Relationships for Laminates with Ply Cracks in In-plane Loading”. In: *International Journal of Damage Mechanics* 14.3 (July 2005), pp. 235–259. ISSN: 1056-7895, 1530-7921. DOI: [10.1177/1056789505050355](https://doi.org/10.1177/1056789505050355).
- [LV20] M. S. Loukil and J. Varna. “Crack face sliding displacement (CSD) as an input in exact GLOB-LOC expressions for in-plane elastic constants of symmetric damaged laminates”. In: *International Journal of Damage Mechanics* 29.4 (Apr. 2020), pp. 547–569. ISSN: 1056-7895, 1530-7921. DOI: [10.1177/1056789519866000](https://doi.org/10.1177/1056789519866000).
- [Man82] B. B. Mandelbrot. *The fractal geometry of nature*. San Francisco: W.H. Freeman, 1982. 460 pp. ISBN: 9780716711865.
- [Mar14] K. Martyniuk. “Microscale fracture of composite materials for wind turbine blades”. PhD thesis. DTU Wind Energy, 2014.
- [McC96] L. N. McCartney. “Stress transfer mechanics for ply cracks in general symmetric laminates”. In: *Technical Report, National Physical laboratory, Centre for Materials Measurement & Technology* (1996).
- [McL17] R. McLendon. *Micromechanics Plugin for Abaqus*. Simulia Learning Community. Feb. 1, 2017. URL: <https://r1132100503382-eu1-3dswym.3dexperience.3ds.com/#community:39/post:4167> (visited on 08/19/2021).

- [MCQ18] L. Maragoni, P. A. Carraro, and M. Quaresimin. “Periodic boundary conditions for FE analyses of a representative volume element for composite laminates with one cracked ply and delaminations”. In: *Composite Structures* 201 (Oct. 2018), pp. 932–941. ISSN: 02638223. DOI: [10.1016/j.compstruct.2018.06.058](https://doi.org/10.1016/j.compstruct.2018.06.058).
- [Mik+20] L. P. Mikkelsen, S. J. Klitgaard, C. F. Niordson, and B. F. Sørensen. “Tunneling cracks in arbitrary oriented off-axis lamina”. In: *International Journal of Fracture* 226.2 (Dec. 2020), pp. 161–179. ISSN: 0376-9429, 1573-2673. DOI: [10.1007/s10704-020-00485-9](https://doi.org/10.1007/s10704-020-00485-9).
- [Mik+21] L. P. Mikkelsen, B. N. Legarth, L. Herrmann, M. M. Christensen, and F. N. Niordson. “A special finite element method applied to off-axis tunnel cracking in laminates”. In: *in review* (2021).
- [MMA21] U. A. Mortensen, L. P. Mikkelsen, and T. L. Andersen. “Observations of fatigue damage in uni-directional non-crimp fabric composites subjected to cyclic bending loads”. In: *in preparation* (2021).
- [Nie13] M. W. Nielsen. “Prediction of process induced shape distortions and residual stresses in large fibre reinforced composite laminates”. PhD thesis. DTU Wind Energy, 2013.
- [PE63] P. Paris and F. Erdogan. “A Critical Analysis of Crack Propagation Laws”. In: *Journal of Basic Engineering* 85.4 (Dec. 1, 1963), pp. 528–533. ISSN: 0021-9223. DOI: [10.1115/1.3656900](https://doi.org/10.1115/1.3656900).
- [PP12] K. Park and G. H. Paulino. “Computational implementation of the PPR potential-based cohesive model in ABAQUS: Educational perspective”. In: *Engineering Fracture Mechanics* 93 (Oct. 2012), pp. 239–262. ISSN: 00137944. DOI: [10.1016/j.engfracmech.2012.02.007](https://doi.org/10.1016/j.engfracmech.2012.02.007).
- [Pup+16] A. Pupurs, J. Varna, M. Loukil, H. Ben Kahla, and D. Mattsson. “Effective stiffness concept in bending modeling of laminates with damage in surface 90-layers”. In: *Composites Part A: Applied Science and Manufacturing* 82 (Mar. 2016), pp. 244–252. ISSN: 1359835X. DOI: [10.1016/j.compositesa.2015.11.012](https://doi.org/10.1016/j.compositesa.2015.11.012).
- [QC14] M. Quaresimin and P.A. Carraro. “Damage initiation and evolution in glass/epoxy tubes subjected to combined tension–torsion fatigue loading”. In: *International Journal of Fatigue* 63 (June 2014), pp. 25–35. ISSN: 01421123. DOI: [10.1016/j.ijfatigue.2014.01.002](https://doi.org/10.1016/j.ijfatigue.2014.01.002).
- [Rei91] K. L. Reifsnider, ed. *Fatigue of composite materials*. Composite materials series 4. Amsterdam ; New York: Elsevier, 1991. 519 pp. ISBN: 9780444705075.
- [RJ82] K. L. Reifsnider and R. Jamison. “Fracture of fatigue-loaded composite laminates”. In: *International Journal of Fatigue* 4.4 (Oct. 1982), pp. 187–197. ISSN: 01421123. DOI: [10.1016/0142-1123\(82\)90001-9](https://doi.org/10.1016/0142-1123(82)90001-9).
- [RK77] E. F. Rybicki and M. F. Kanninen. “A finite element calculation of stress intensity factors by a modified crack closure integral”. In: *Engineering Fracture Mechanics* 9.4 (Jan. 1977), pp. 931–938. ISSN: 00137944. DOI: [10.1016/0013-7944\(77\)90013-3](https://doi.org/10.1016/0013-7944(77)90013-3).

- [SF04] A. S. J. Suiker and N. A. Fleck. “Crack tunneling and plane-strain delamination in layered solids”. In: *International Journal of Fracture* 125.1 (Jan. 2004), pp. 1–32. ISSN: 0376-9429. DOI: [10.1023/B:FRAC.0000021064.52949.e2](https://doi.org/10.1023/B:FRAC.0000021064.52949.e2).
- [SJ09] B. F. Sørensen and T. K. Jacobsen. “Characterizing delamination of fibre composites by mixed mode cohesive laws”. In: *Composites Science and Technology* 69.3 (Mar. 2009), pp. 445–456. ISSN: 02663538. DOI: [10.1016/j.compscitech.2008.11.025](https://doi.org/10.1016/j.compscitech.2008.11.025).
- [Sør+06] B. F. Sørensen, K. Jørgensen, T. K. Jacobsen, and R. C. Østergaard. “DCB-specimen loaded with uneven bending moments”. In: *International Journal of Fracture* 141.1 (Sept. 2006), pp. 163–176. ISSN: 0376-9429, 1573-2673. DOI: [10.1007/s10704-006-0071-x](https://doi.org/10.1007/s10704-006-0071-x).
- [Sri08] S. Sridharan, ed. *Delamination behaviour of composites*. Woodhead Publishing in materials. OCLC: 551366924. Cambridge: Woodhead Publ. [u.a.], 2008. 762 pp. ISBN: 9781845692445 9781420079678 9781845694821.
- [Sun10] B. Sundström. *Handbook of solid mechanics*. Kungliga tekniska högskolan, Institutionen för hållfasthetslära. OCLC: 938957431. Stockholm: Department of Solid Mechanics, KTH, 2010. ISBN: 9789197286046.
- [Sys20] Dassault Systems. *Abaqus user manual*. 2020.
- [Ton+97] J. Tong, F. J. Guild, S. L. Ogin, and P. A. Smith. “On matrix crack growth in quasi-isotropic laminates—I. Experimental investigation”. In: *Composites Science and Technology* 57.11 (Jan. 1997), pp. 1527–1535. ISSN: 02663538. DOI: [10.1016/S0266-3538\(97\)00080-8](https://doi.org/10.1016/S0266-3538(97)00080-8).
- [TV16] R. Talreja and J. Varna, eds. *Modeling damage, fatigue and failure of composite materials*. Woodhead publishing series in composites science and engineering number 65. OCLC: 935892426. Amsterdam Boston Cambridge: Elsevier/WP, Woodhead Publishing, 2016. 454 pp. ISBN: 9781782422860 9781782422983.
- [Var+99] J. Varna, R. Joffe, N V Akshantala, and R Talreja. “Damage in composite laminates with off-axis plies”. In: *Composites Science and Technology* 59.14 (Nov. 1999), pp. 2139–2147. ISSN: 02663538. DOI: [10.1016/S0266-3538\(99\)00070-6](https://doi.org/10.1016/S0266-3538(99)00070-6).
- [VH10] V. Vinogradov and Z. Hashin. “Variational analysis of cracked angle-ply laminates”. In: *Composites Science and Technology* 70.4 (Apr. 2010), pp. 638–646. ISSN: 02663538. DOI: [10.1016/j.compscitech.2009.12.018](https://doi.org/10.1016/j.compscitech.2009.12.018).
- [Wan+18] Y. Wang, L. P. Mikkelsen, G. Pyka, and P. Withers. “Time-Lapse Helical X-ray Computed Tomography (CT) Study of Tensile Fatigue Damage Formation in Composites for Wind Turbine Blades”. In: *Materials* 11.11 (Nov. 21, 2018), p. 2340. ISSN: 1996-1944. DOI: [10.3390/ma11112340](https://doi.org/10.3390/ma11112340).
- [Wis12] M. R. Wisnom. “The role of delamination in failure of fibre-reinforced composites”. In: *Philosophical Transactions of the Royal Society A: Mathematical, Physical and Engineering Sciences* 370.1965 (Apr. 28, 2012), pp. 1850–1870. ISSN: 1364-503X, 1471-2962. DOI: [10.1098/rsta.2011.0441](https://doi.org/10.1098/rsta.2011.0441).

- [WL07] P. Wriggers and T. A. Laursen, eds. *Computational Contact Mechanics*. Red. by Giulio Maier, Jean Salençon, Wilhelm Schneider, Bernhard Schrefler, and Paolo Serafini. Vol. 498. CISM International Centre for Mechanical Sciences. Vienna: Springer Vienna, 2007. ISBN: 9783211772973 9783211772980. DOI: [10.1007/978-3-211-77298-0](https://doi.org/10.1007/978-3-211-77298-0).
- [ZB09] D. Zenkert and M. Battley. *Laminate and sandwich structures: foundations of fibre composites*. 2nd ed. Polyteknisk Forlag, 2009. ISBN: 9788770780537.
- [ZBG14] J. Zangenberg, P. Brøndsted, and J. W. Gillespie. “Fatigue damage propagation in unidirectional glass fibre reinforced composites made of a non-crimp fabric”. In: *Journal of Composite Materials* 48.22 (Sept. 1, 2014), pp. 2711–2727. ISSN: 0021-9983. DOI: [10.1177/0021998313502062](https://doi.org/10.1177/0021998313502062).
- [Zeh12] A. T. Zehnder. *Fracture mechanics*. Lecture notes in applied and computational mechanics 62. OCLC: ocn755698387. London ; New York: Springer Science+Business Media, 2012. 223 pp. ISBN: 9789400725942 9789400725959.
- [ZH99] J. Zhang and K. P. Herrmann. “Stiffness degradation induced by multilayer intralaminar cracking in composite laminates”. In: *Composites Part A: Applied Science and Manufacturing* 30.5 (May 1999), pp. 683–706. ISSN: 1359835X. DOI: [10.1016/S1359-835X\(98\)00106-7](https://doi.org/10.1016/S1359-835X(98)00106-7).

**Author:** Leon Herrmann

**Title:** Fracture modeling of layered composites in a specialized off-axis finite element framework

**DTU Wind Energy-M-0485**

**October 2021**

**Project period:**

**May - October 2021**

**ECTS: 30**

**Education: Master of Science**

**Supervisors:**

Lars Pilgaard Mikkelsen

**DTU Wind Energy**

Christian Frithiof Niordson

Brian Nyvang Legarth

**DTU Mechanical Engineering**

Fabian Duddeck

**TU München**

**Remarks:**

This report is submitted as partial fulfillment of the requirements for graduation in the above education at the Technical University of Denmark.

DTU Wind Energy is a department of the Technical University of Denmark with a unique integration of research, education, innovation and public/private sector consulting in the field of wind energy. Our activities develop new opportunities and technology for the global and Danish exploitation of wind energy. Research focuses on key technical-scientific fields, which are central for the development, innovation and use of wind energy and provides the basis for advanced education at the education.

**Technical University of Denmark**

Department of Wind Energy  
Frederiksborgvej 399  
4000 Roskilde  
Denmark

[www.vindenergi.dtu.dk](http://www.vindenergi.dtu.dk)